Universita' degli studi di Padova

Scuola di Dottorato di Ricerca in
Ingegneria dell'Informazione

Indirizzo Bioingegneria

Ciclo XXIV

Methods for Segmentation and Characterization of Multiple Sclerosis Cortical Lesions from MRI Data

Direttore della Scuola: **Ch.mo Prof. Matteo Bertocco**

Supervisore: **Ch.mo Prof. Enrico Grisan**

Dottorando: **Elisa Veronese**

Contents

List of Figures

Sommario

Questa tesi tratta l'analisi automatica di immagini di risonanza magnetica cerebrale in soggetti affetti da sclerosi multipla. In particolare, l'analisi è volta sia a una stima quantitativa del carico di lesioni corticali presenti a causa del decorso della malattia, sia a una caratterizzazione del tipo di lesioni presenti basata sul loro grado di infiammazione.

La sclerosi multipla è una malattia infiammatoria a decorso cronico che colpisce il sistema nervoso centrale, provocandone una progressiva distruzione della mielina in più aree. Per frequenza, nel giovane adulto è la seconda malattia neurologica e la prima di tipo infiammatorio cronico. Inoltre, la sclerosi multipla può essere considerata anche come malattia sociale, con un'elevata ricaduta economica, sia diretta che indiretta: la diminuzione o la perdita dell'autonomia porta alla progressiva impossibilità di svolgere una qualsiasi attività lavorativa fino all'incapacità di condurre una vita indipendente. A questo si aggiungano il costo delle cure e dell'assistenza necessarie.

Benché le cause siano ancora in parte sconosciute, molto è stato fatto nel chiarire le diverse fasi del processo infiammatorio che caratterizza tale patologia, permettendo così di arrivare a una diagnosi e a un trattamento precoce che consentono di ridurre gli effetti della malattia.

Le lesioni causate dalla sclerosi multipla risultano visibili grazie a particolari tecniche di acquisizione di immagini basate sulla risonanza magnetica. In particolare negli ultimi decenni si sono studiate e messe a punto diverse sequenze di risonanza ottimizzate per la visualizzazione delle lesioni in mate-

ria bianca. Il quadro delle tecniche a disposizione qualora si vogliano studiare lesioni in materia grigia risulta invece meno completo, soprattutto a causa del fatto che la scoperta di un coinvolgimento della materia grigia nella malattia è molto più recente.
La verifica dell'evoluzione e della comparsa di nuove lesioni è importante dal momento che consente di monitorare il progredire di una malattia caratterizzata da fasi acute intervallate a periodi di quiescenza più o meno lunghi. Per questo motivo i soggetti affetti da sclerosi multipla vengono periodicamente sottoposti a esami di risonanza magnetica. Ogni successiva valutazione da parte del medico neurologo dipenderà da quanto evidenziato dalle immagini acquisite. In questo senso è fondamentale che il medico sia ben allenato nella valutazione di immagini di risonanza, e che ponga particolare attenzione non solo nell'individuare la comparsa di nuove lesioni, ma anche nel riconoscere la presenza di lesioni già presenti in esami precedenti, che possono essere progredite nella forma, nelle dimensioni e nel grado di attività. La lettura di un esame di risonanza magnetica richiede tempo e attenzione, ed è inevitabilmente soggetta all'errore umano che caratterizza qualsiasi valutazione manuale. Per questo, benché sia impensabile prescindere dalla valutazione del medico, una tecnica di analisi automatica di immagini di risonanza magnetica cerebrale che sia in grado di evidenziare la presenza di lesioni da sclerosi multipla può rappresentare un valido aiuto alla refertazione, sia in termini di tempo che di accuratezza.

In questa tesi si descriveranno le tecniche di risonanza magnetica a disposizione per una miglior visualizzazione delle lesioni corticali. Su queste si procederà alla segmentazione del tessuto di interesse, ossia del volume di materia grigia. In seguito verrà descritta la tecnica proposta per il riconoscimento delle regioni patologiche corticali. Infine sarà descritto un primo tentativo di caratterizzazione delle diverse lesioni corticali, basato sulla valutazione del grado di attività di ciascuna lesione.

Summary

This thesis deals with the automatic analysis of magnetic resonance images of the brain, acquired from people affected by multiple sclerosis. In particular, the primary aim of the analysis is to obtain a quantitative measure of the cortical lesion burden due to the specific disease. Besides, we propose a technique for the characterization of the different lesion types, based on their inflammatory activity.

Multiple sclerosis is a chronic, inflammatory disease of the central nervous system, that causes a progressive demyelination of several areas of the brain and of the spinal cord. As far as diseases' frequency is concerned, multiple sclerosis represents the second neurologic disease in the young adult, and it is even the first inflammatory chronic disease. Besides, it can also be considered as a social burden, with heavy direct and indirect costs: multiple sclerosis prevents people from working as much as they could without the disease, and can lead to the impossibility to live autonomously. Last but not least, the cost of treatment and care can be very high.

Although the causes are still partly unclear, a lot has been achieved in the understanding of the different phases of the inflammatory process characterizing multiple sclerosis. Today it is possible to early diagnose the disease, thus allowing to limit symptoms by early therapies.

The lesions caused by multiple sclerosis can be visualized in vivo thanks to magnetic resonance (MR) imaging. In particular in the latest decades several MR sequences have been designed in order to highlight white matter lesions.

When studying gray matter lesions, instead, the available MR sequences are less numerous. This is partly due to the fact that the gray matter involvement in multiple sclerosis is a relatively recent finding.

It is important to verify both the evolution and the appearance of new lesions: in this way it is possible to monitor the disease progression, which is particularly tricky in the case of multiple sclerosis. This disease is characterized by acute relapses alternated with remitting periods of variable length. For this reason patients are periodically examined acquiring MR images. The subsequent diagnosis made by the physician is based on the MR results.
So, it is fundamental for the neurologist to be well trained in order to be able to properly evaluate different magnetic resonance sequences. Besides, he/she has to pay close attention not only to detect new lesions, but also to recognize those lesions that were already present in the previous examinations, and that might have changed their shape, their dimension or they activity. This process requires time and attention, but unfortunately, being human-based, it is strongly error prone. Unquestionably, the diagnose cannot prescind from the neurologist's evaluation. Nonetheless, the advent of techniques for the automatic analysis of magnetic resonance images and for the detection of multiple sclerosis lesions would represent a valid support for the physicians, who could provide accurate evaluations in faster timing.

In this thesis several MR techniques currently used for cortical lesions visualization will be described. Then a segmentation algorithm will be proposed, in order to find the region corresponding to gray matter. On this region a second algorithm will be presented, that detect multiple sclerosis cortical lesions. Finally, a first attempt to characterize cortical lesions based on their inflammatory activity will be described.

Chapter 1

Introduction

Multiple sclerosis is an autoimmune disease of the central nervous system. It represents the second neurologic disease in the young adult and it causes neurological disability resulting from the interruption of myelinated tracts in the central nervous system.
Currently, there are about 400,000 people living with multiple sclerosis in the United States, more than 100,000 people in the U.K. and more than 2 million people throughout the world (Fig. 1.1). A recent study in the U.K. tried to put a number to the economic cost of multiple sclerosis. They found that multiple sclerosis costs are mostly sustained by family members who provide care and money for treatments. The estimated costs are little less than 2 billion US dollars. This doesn't count the lost opportunity costs of not being able to work. For the U.S. the costs are different, but for a rough estimate it is sufficient to multiply the above costs by 5 (because there are about 5 times more people living with multiple sclerosis in the U.S. than in the U.K.).

Worldwide, the diagnosis made by the neurologists is mainly based on the so called MacDonald criteria ([62]) (Fig. 1.2), which exploit the information derivable from magnetic resonance imaging exams. Actually, magnetic resonance imaging is used not only in order to assess the diagnosis, but also to monitor the patients' follow up all their life long. With the increasing availability of different magnetic resonance sequences, which allow to differently enhance distinct parts of the brain, it is clear that the number of magnetic resonance acquisitions is destined to increase. In this sense, an automatic

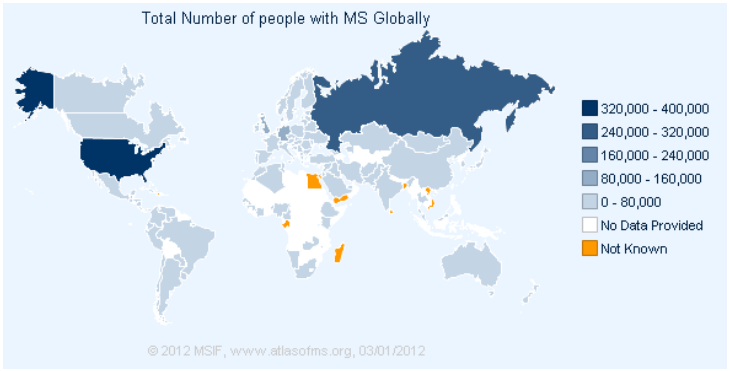

Figure (1.1). *Map of the total number of people with multiple sclerosis worldwide (Image taken from http://www.atlasofms.org/index.aspx).*

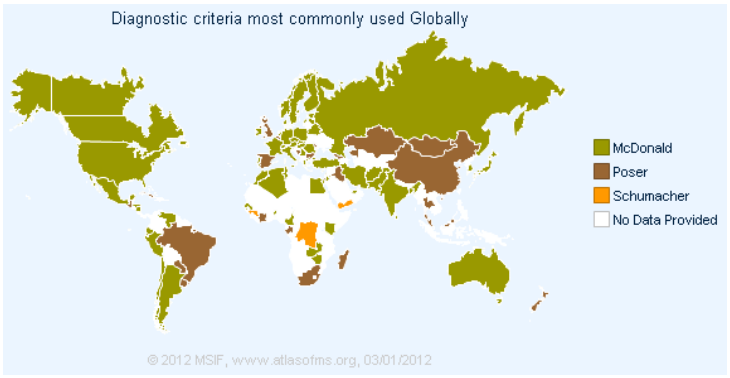

Figure (1.2). *Map of the diagnostic criteria most commonly used globally (Image taken from http://www.atlasofms.org/index.aspx).*

analysis of such images might relieve, at least partially, the burden of brain lesions and alterations screening carried on by the neurologists.

1.1 Aim and Objectives

The aim of the work presented in this thesis is to develop a tool for an automatic segmentation of cortical lesions caused by multiple sclerosis, starting from specific magnetic resonance sequences. The actual goal is not limited to lesions segmentation, but includes an attempt to characterize cortical lesions according to their inflammatory activity. This can be done exploiting specific magnetic resonance sequences that are sensitive to the altered concentration of both myelin and tissue iron.

Cortical lesion detection is currently performed manually. It is an operation that requires a lot of time and expertise. In fact, the neurologist must be well trained in examining magnetic resonance images, in order to be able to recognize tissue alterations. At the same time he/she has to be cautious in order not to classify as lesion those regions of the images that are corrupted by noise. Though all this process is usually made by an experienced neurologist, who pays close attention in order to obtain the most accurate results possible, the segmentation stage is strongly error prone and operator dependent.

In the light of these considerations, an automatic technique for cortical lesions segmentation would become a useful aid in magnetic resonance images report. It would save physicians' time, allowing them to simply scoring a small set of automatically highlighted regions; in this way they could avoid perusing the entire magnetic resonance acquired volume.
We propose a method that makes use of two different magnetic resonance sequences: the first is a fluid attenuated inversion recovery (FLAIR) sequence, while the second is a Double Inversion Recovery (DIR) sequence. These two specific acquisition modalities allow to enhance those tissues we are interested in.

First of all, we perform an automatic segmentation of the gray matter. To do so, FLAIR and DIR volumes have to be coregistered. Then we use an active contour based method to segment both white and gray matter from the FLAIR sequence, discarding the cerebrospinal fluid and all the other surrounding tissues. By exploiting the spatial relationship between white and gray matter, we can apply the segmentation on FLAIR to the DIR sequence, on which we can now segment the gray matter. All this procedure revealed to be necessary because, although cortical lesions appear as hyper intense regions in DIR, the use of a simple threshold does not suffice. Besides, segmentation performed with commonly available brain imaging software often gives weak results when the brain to be segmented is altered by the presence of lesions.

Within the obtained gray matter segmentation, we automatically detect those regions in DIR that appear as localized hyperintense areas. According to the consensus criteria defined by Geurts et al. ([34]), these are highly suspectable of being actual cortical lesions.

The last step addresses the characterization of cortical lesions. This can be achieved exploiting specific magnetic resonance sequences that are sensitive to tissue parameters that mirror the inflammatory status of a lesion. These parameters include local concentration of myelin and iron.

1.2 Outline of the Thesis

Chap. 2-3 are introductory chapters. In particular, the former describes multiple sclerosis, illustrating the peculiarities of this disease, its most common symptoms and diagnosis techniques, and the most recent theories about its causes. The final section is dedicated to iron accumulation in the brain, with a particular stress on brain tissue iron accumulation in multiple sclerosis. In Chap. 3 the basic principles of magnetic resonance imaging are described, in order to better appreciate the peculiarities of the specific sequences we are working with. Chap. 4 deals with brain segmentation: it starts highlighting the major problems related to this field of medical image processing and it lists the most popular brain imaging software, focusing both on their pros and cons. Then the Level Set method and the Active Contour models are described, in order to finally illustrate the gray matter segmentation method proposed in this thesis. Cortical lesions segmentation is the object of Chap. 5: in particular, the consensus recommendations for cortical lesions identification are initially recalled. Then the major problems due both to bias field inhomogeneities and to artifact prone areas are explained. Finally, the proposed cortical lesion segmentation technique is described. In Chap. 6 results are reported. Before describing the performance of the proposed method, technical information regarding the MR scanner used and the acquired MRI volumes acquired will be summarized.
Chap. 7 deals with the problem of in vivo lesions characterization by means of tissue iron quantification. Given that this project is still on an early stage, it has been discussed apart.
Finally, a brief discussion on the whole thesis, together with a description of possible future developments, will be contained in Chap. 8.

Chapter 2

Multiple Sclerosis

2.1 Multiple sclerosis

Multiple sclerosis (MS) is an autoimmune demyelinating disease. It represents a common cause of neurological disability in young adults resulting from the interruption of myelinated tracts in the central nervous system.
Currently, there are about 400,000 people living with multiple sclerosis in the United States, 100,000 people in the UK and more than 2 million people throughout the world. The first attack often occurs when the patient is between the ages of 20 and 40, although this and subsequent attacks may not be recognized as MS until much later. Like many other diseases, MS existed long before it had a name. Writings from as far back as the Middle Ages described patients with symptoms that doctors today believe pointed to MS [17]. It was the French neurologist Jean-Martin Charcot (1825-1893) the first person credited with identifying MS as a disease. After a patient of his had died, he dissected her brain and discovered the brain lesions. He called the disease *sclerose en plaques*. Myelin was discovered shortly afterwards, although its exact significance was unknown. The name "multiple sclerosis" means that a patient has more than one sclerosis, which is a plaque, or lesion that can appear both in the white matter and in the gray matter of the brain, or in the spinal cord. Lesions can lead to a breakdown of the myelin sheath, the protective layer surrounding the axons. This breakdown is known as demyelinization. When the myelin sheath thins and breaks down, the axon is

not able to function correctly anymore, and electrical signals cannot travel between neurons. Although the myelin can rebuild itself, a process that is called remyelination [77], the rate of demyelinization caused by MS is too rapid for it to keep up. In some cases, the axon is cut completely.
In summary, MS's major features can be distinguished as follows:

- destruction of myelin, which is the main characteristic of MS. The final results of this process, called demyelination, are multiple patches of hard, scarred tissue called plaques;
- destruction of axons, which is also a major factor in the permanent disability that occurs with MS.

The symptoms, severity, and course of MS vary widely depending partly on the sites of the plaques and the extent of the demyelination. This is the reason why MS is an extremely unpredictable disease: lesions can occur anywhere in the central nervous system and the stages and rates of demyelinization vary depending on the lesion.

2.2 Symptoms

The symptoms, severity, and course of MS vary widely depending partly on the sites of the plaques and the extent of the demyelination. The specific symptoms that appear depend upon both which part of the central nervous system is affected and the function of the damaged nerve. Most patients first experience multiple sclerosis as a single attack of symptoms called a *clinical isolated syndrome*, which typically occurs between the ages of 20 and 40 years. Once a second attack occurs, the patient is considered to have relapsing-remitting multiple sclerosis. Much less commonly, the disease is progressive from the start and symptoms are more or less continuous.

Early symptoms

Early symptoms may include:

- optic neuritis and other problems in the eye;
- fatigue;
- changes in sensations in the arms and legs;
- muscle weakness in the legs and poor coordination;
- Lhermitte's sign;
- spasticity;
- disturbances in the bladder.

Additional symptoms occurring over time

In addition to the persistence of early symptoms, some patients experience the following symptoms as the disease progresses:

- imbalance and dizziness;
- tremors;
- facial pain;
- spasm-related symptoms (burning, itching, aching, quivering sensations);
- speech difficulties;
- difficulty swallowing;
- symptoms in the gastrointestinal, urinary, and genital tracts;
- emotional mood swings;
- problems in concentration and memory;
- hearing loss.

Possible symptom triggers

Some external agents are known to worsen MS symptoms. Among them there are viral infections and stress. Besides, heat, whether generated by ambient temperature, infection, or physical activity, worsens MS symptoms in about 60% of patients.

2.3 Classification of different types of MS

There are two major types of MS: Chronic-Progressive MS, which is commonly recognized to have three different variants, and Relapsing-Remitting MS.

Relapsing-Remitting Multiple Sclerosis

It generally occurs in younger people and is the most common form of MS. About 20% of patients with relapsing-remitting MS experience little or no progression after a first attack for long periods of time, although by 25 years most patients have converted to a progressive phase. Diagnosis of relapsing remitting MS rests either on two relapses separated by more than 30 days, or one relapse and an MRI scan three months later, showing new lesions.

Chronic-Progressive Multiple Sclerosis

In this case symptoms continue to worsen slowly without remission. About 20% of MS patients (usually those whose first symptoms occur after the age of 45) have the chronic-progressive form without first developing relapsing-remitting MS. Chronic-progressive MS generally follows a downhill course, but its severity varies widely. Three variants are commonly used to define this patient group:

Progressive-Relapsing - Patients with this rare form of MS get progressively and steadily worse and also suffer relapses. Sometimes they recover briefly, but they never experience remission of the disease.

Primary-Progressive - A small percentage of MS patients experience a slow progression of the disease without attacks or remissions. They may temporarily improve, or the disease may stay the same for short periods of time. Primary progressive MS is diagnosed if there have been no previous relapses and if there is a progression of disability over at least one year, if there is an MRI scan that shows lesions consistent with MS, and if there is evidence of MS detected by examining the spinal fluid collected during a lumbar puncture.

Secondary-Progressive - Some patients begin with a diagnosis of progressive-relapsing MS but develop secondary-progressive MS. This means that the disease progresses more quickly, and they may or may not experience attacks, periods of recovery or periods of remission.

Table (2.1). *Neurologic disability classification: Expanded Disability Status Scale (EDSS). (* Data taken from [18])*

Score	**Disability description**	**RRMS: average time until onset of symptoms(*)**	**CPMS: average time until onset of symptoms(*)**
1	No disability and minimal neurologic symptoms.	11.4 years from Score 1 to Score 4	0 years from Score 1 to Score 4
2	Minimal disability in one or two functional areas. Slight weakness or stiffness, mild walking impairment or visual disturbances.		
3	Moderate disability in one functional area, such as vision or the urinary tract, and possibly more than one minimal disability in several others. Either a part of one of the limbs or a whole side can be partially paralyzed. May stagger at times.		
4	Disability is relatively severe but there is full ability to walk without aid. Patients are self-sufficient and can be active 12 hours a day and carry on normal activities. Can walk without aid or rest for 300 to 500 meters.		
5	Disability is severe enough to impair or even preclude a full day's activities. Able to walk unaided and without rest for 100 to 200 meters.	23.1 years from Score 1 to Score 6	7.1 years from Score 1 to Score 6
6	Can walk unaided for about 100 meters only with assistance or devices, such as two canes, crutches, or braces.		
7	Mostly restricted to wheelchair, although can manage the wheelchair and leave it unassisted. Can walk with aids no further than about five meters.	33.1 years from Score 1 to Score 7	13.4 years from Score 1 to Score 7
8	Mostly restricted to wheelchair or even bed, but still has effective use of arms remains and able to perform many self-care functions.	(Data not avalable)	(Data not available)
9	Bedridden. Patient can communicate or eat.		
10	Fatality occurs from complications.		

2.4 Diagnosis

Due to its complexity and variety of symptoms, MS is not easy to diagnose. Nowadays MS diagnosis is most commonly performed using magnetic resonance imaging (MRI), analysis of cerebrospinal fluid and evoked potentials. All these tests are taken in conjunction with a neurological examination to verify the different symptoms experienced by the patient. Early diagnosis is important, because MS can cause permanent neurological damage and getting on medication as soon as possible can help to mitigate the symptoms.
In order to assess and predict future disability a scale called the Expanded Disability Status Scale (EDSS) [50] is commonly used (Tab. 2.1). The system uses a score of 1 to 10 to rate the degree of walking disability. The scale has been used also to attempt to predict average times for progression from one stage to the next depending on whether patients have relapsing-remitting or chronic progressive MS.

2.5 Causes

The cause, or causes, of multiple sclerosis are still unknown. Genetic factors certainly play a role in MS. No single gene, however, is likely to be responsible for causing MS. Rather, the current theory is that the disease occurs in people with a genetic susceptibility who are exposed to some environmental assault (a virus or a toxin) that disrupts the blood-brain barrier. Immune factors converge in the nerve cells and trigger inflammation and an autoimmune attack (a self-attack) on myelin and axons. Still, a number of disease patterns have been observed in patients, so that MS is often considered not as single disorder, but it may instead represent several diseases with different causes.

Genetic Factors

Genetic factors probably play some role in making a person susceptible to the disease process leading to MS. In particular, abnormalities in the human leukocyte antigen (HLA) region located on chromosome 6 appear to be more

prevalent among people with MS.
In 1972, three different groups [65], [46], [6] reported the first studies of HLA in MS. It has been theorized, however, that a combination of genes (not a single gene) is implicated in the development of MS, and the risk for someone inheriting all of these genetic factors is less than 5% (for an extensive review, see [68] and [92]).

Infectious Organisms

Infectious organisms, most likely viruses that can affect the central nervous system, are suspected of triggering the autoimmune response in people genetically susceptible to MS. Although many infectious microorganisms have been investigated, no one organism has emerged as a proven trigger. It is possible different patients may be affected by different organisms, and that infections cause some, but not all, cases of MS. At present, three microorganisms are mostly under suspicion:

- HHV-6. Herpesvirus 6 [41];
- Epstein-Barr virus (EBV) [103];
- Chlamydia Pneumoniae [28].

Other viruses that have been investigated include measles virus, adenovirus, and the retroviruses (HIV, HTLV-I, and HTLV-II), but none have emerged as having any importance.

2.6 The autoimmune disease process

Multiple sclerosis is an autoimmune disease. Autoimmunity may develop when the body's immune system is damaged by genetic or environmental factors or both, causing it to attack its own tissues. In MS the myelin sheaths of the central nervous system are attacked by T-cells and monocytes. Thus, one of the tests for MS is a spinal tap, which allows checking whether the cerebrospinal fluid contains an abnormally high number of antibodies and certain

protein byproducts which indicate a breakdown of myelin, composed of protein and lipids.
In particular T-cells mistake the body's own myelin as a foreign antigen. Myelin cells become self-antigens. As a consequence, T-cells set off the usual cascading immune events, including the release of B-lymphocytes. The B-lymphocytes give off antibodies, which in this case are referred to as autoantibodies. Autoantibodies can attack both myelin proteins and the oligodendrocytes. At the injured site, masses of leukocytes gather. The leukocytes release cytokines, small proteins that in normal condition are indispensable in the healing process. However when they are overproduced, like in MS, they play a major role in the destructive process.
The body often makes corrective actions to offset the effects of the nerve cell destruction. For example, an increase in the density of the sodium channels, which carry electric charges, has been observed. By increasing the number of sodium channels, the nerve cells can continue to communicate, in spite of the loss of myelin [102]. Besides, the nerves retain some capacity to remyelinate, restoring the damaged myelin ([77],[72]). Such processes are probably responsible for the remissions that most patients experience.

2.7 Gray matter pathology

Although MS has been regarded as a disorder predominantly affecting the WM, interest in GM involvement has been increasing since the discover of GM damage due to MS ([10],[61]). In the beginning phase of MS, specific periventricular focal WM lesions appear; demylination of the GM is relatively sparse in the beginning phases of the disease but then rapidly increases when the disease progresses.

Extensive demyelination in the cortex (Figure 2.1) is associated with a more progressive phase of the disease. As it can be seen in Figure 2.2, there is an evident disproportion of increasing in the damage of the two tissues. Juxtacortical, cortical, hypothalamic, and hippocampal lesions have been shown to correlate with the degree of clinical disability ([35]).

GM damage can be directly viewed thanks to post mortem studies: in [51],

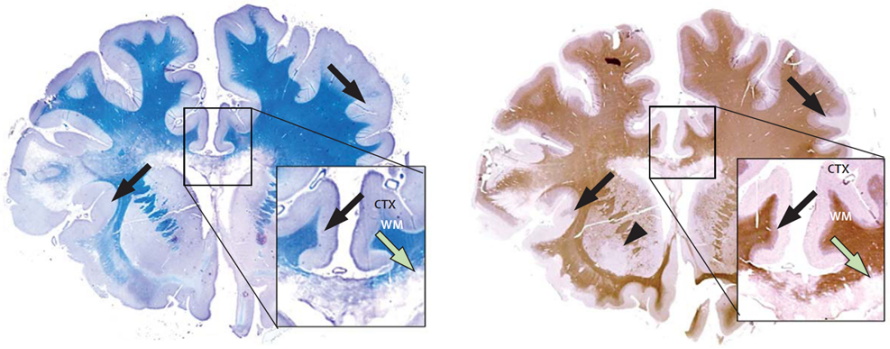

Figure (2.1). *Brain section histochemically stained for myelin by use of the Luxol fast-blue technique (left panel) and histochemically stained for proteolipid protein (right panel). The green arrow shows readily detectable periventricular WM demyelination; black arrows show cortical loss of myelin in the cerebral cortex (CTX). Images adapted from [35]. (Courtesy of Dr. J.J.G. Geurts).*

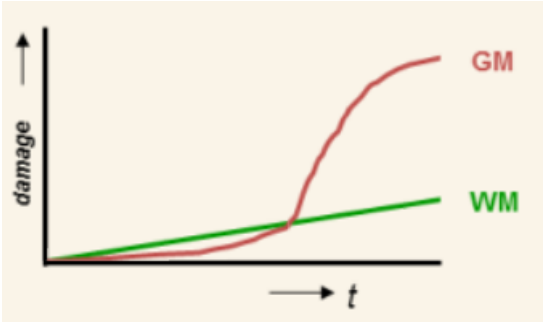

Figure (2.2). *Plot of the damage in the WM and in the GM over time. (Courtesy of Dr. J.J.G. Geurts).*

the amount of cortical demyelination was reported to be different in relation to the disease course. In particular, demyelination in the cerebral cortex was mainly a feature in patients with SPMS and PPMS. Demyelination mainly affected the subpial layers of the cerebral cortex and was associated with mononuclear inflammatory infiltrates in the meninges.

As summarized in [33], different classification systems for cortical MS lesions have been proposed: among them the system of Bö et al. ([8]) is based on the anatomic observations by Dawson ([22]). This system distinguishes mixed GM-WM lesions (type I cortical lesions) from purely intracortical lesions (types II-IV). Type II lesions are small intracortical lesions, type III lesions are larger lesions extending from the pia downwards without reaching the subcortical WM, and type IV lesions affect the entire width of the cortex from pial surface to the WM. Type III lesions are most frequently seen and can extend over several gyri, in certain cases leading to a general cortical subpial demyelination (Figure 2.3).

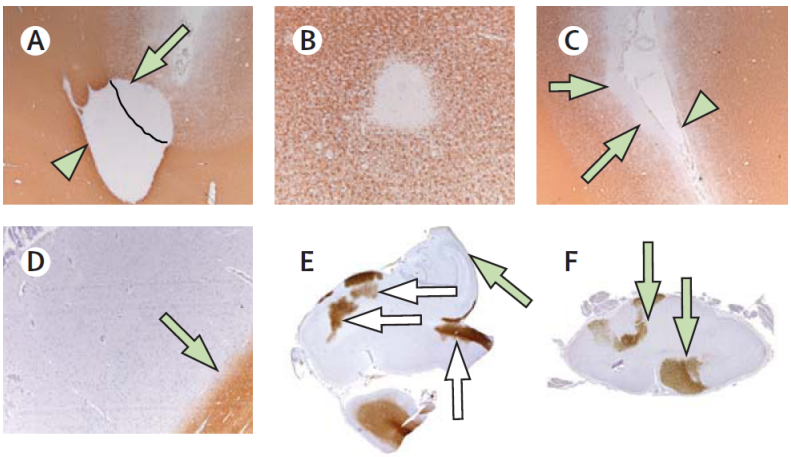

Figure (2.3). *(A) Type I or mixed WM-GM lesion: the black line indicates the border between the cortex (arrow) and the subcortical WM (arrowhead). (B) Type II intracortical lesion. (C) Type III subpial cortical lesion (arrows); arrowhead indicates normal cortex. (D) Type IV lesion, spanning the entire cortical ribbon. (E) Hippocampal lesion. (F) Spinal cord lesion. Images adapted from [35]. (Courtesy of Dr. J.J.G. Geurts).*

2.7.1 Cortical Lesions Identification: Consensus Recommendations

As it will be described in 3.5.2, the aim of DIR MRI sequence is to visualize GM, while suppressing the signals from WM and CSF. Unfortunately, this double suppression scheme creates an image with low signal-to-noise ratio, which, combined with the influence of a nonuniform magnetic field in the cortex and flow artifacts, used to leave clinicians in a state of uncertainty about whether all signal hyperintensities on DIR should be considered actual cortical lesions. A recent study ([63])using advanced multicontrast 3-dimensional imaging confirmed the usefulness of DIR imaging, by showing that it permits the highest detection of cortical lesions when compared with other sequences.

In order to visualize cortical lesions, different DIR sequences are currently

Figure (2.4). *Areas of high signal in the archicortex and paleocortex, such as the isula (left panel, arrows). Cortical vessels as source of hyperintense signal (right and top panel). (Courtesy of Dr. J.J.G. Geurts).*

used in multiple sclerosis research centers; this represents a problem both when trying to compare published data and, from a clinician's point of view, when making diagnosis on images acquired with a protocol that differs from the one he/she is used to. Recently, an important attempt has been performed in order to formulate consensus recommendations for scoring cortical lesions in patients with MS, using DIR images acquired in 6 European centers according to local protocols ([34]). To this aim, a multinational meeting was or-

ganized to reach consensus. The work presents the results of this consensus meeting, and the first application of the recommendations to a DIR dataset. A set of recommendations for cortical lesion scoring has been defined. In particular, it was decided to score cortical lesions, which had to be entirely or partly located in the cortical GM, ignoring subpial demyelination ([7]) and lesions located in WM directly adjacent to the cortex (i.e., not entering the cortical GM). It was deemed mandatory that:

- cortical lesions are hyperintense on DIR images, compared to surrounding normal-appearing GM (NAGM);
- cortical hyperintensities should have an area not smaller than 3 pixels (based on minimally 1 mm^2 in-plane resolution).

Other less obligatory, though suggested, recommendations were defined: in particular, readers are requested to become familiar with those areas of the brain that are particularly prone to artifacts on DIR. For example, areas such as the insula, or areas in the correspondence of cortical vessels (typically the superior sagittal sinus) may be mistaken for cortical lesions (Figure 2.4).
Although these recommendations may enable a more integrated interpretation of DIR hyperintensities, from [34] it resulted that they still leave readers divided as to the nature of almost half of the hyperintensities identified by at least one of the groups in which the raters had clustered. The DIR sequences acquired in Padova, Amsterdam, and Basel elicited the highest average agreement per lesion.
So, a still open issue when manually scoring images is represented by factors such as lesion type, size, and location, as well as field strength, image quality measures, and sequence type. This evidence arises the need of a more adequate technique to standardize cortical lesions detection.

2.8 Iron accumulation in the brain

The presence of iron in the brain was reported as early as 1886 by the German pathologist, S.S. Zaleski. His results were confirmed and extended by Hugo

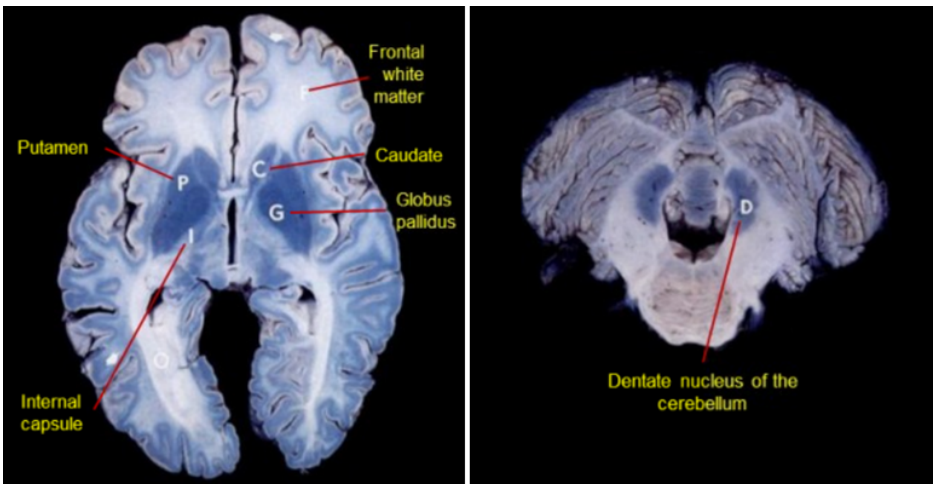

Figure (2.5). *Perls stain of normal brain (44-year-old man): axial slice (left panel) and dentate nucleus of the cerebellum (left panel). The greater intensity of blueness on the Perls stain corresponds to highest concentration of ferric iron. (Images adapted from [25])*

Spatz in 1922. He used the Perls' staining technique to produce bright blue precipitates in brain regions with high iron concentrations and demonstrated strong concentrations of ferric iron in the deep brain nuclei of the extrapyramidal motor system including the globus pallidus, the caudate nucleus, the red nucleus, the dentate nucleus and the substantia nigra, as shown in Figure 2.5 (For an extensive review, see [48] and [25]). The accumulation of iron is dependent on age and is different for different structures. In the healthy brain, the highest content of iron is found in the globus pallidus ([38]). In brain tissues, iron is mainly stored in the proteins ferritin and hemosiderin, which serve as a buffer against harmful iron deficiency or iron overload ([9]). Ferritin is a large protein, ca. 12.0 nm in diameter, formed from a spherical protein coat (apoferritin) that surrounds a core of hydrous ferric oxide [Fe(III)O-OH]. The protein coat, composed of 24 subunits, is in contact with the iron core at several points on the inner surface, forming an iron-protein interface. Iron passes into and out of the core most likely through the channels in the protein [93]. Hemosiderin is another iron-storage complex. Its molecular nature remains poorly defined. It appears to be a complex of ferritin, denatured ferritin and other material. The iron within deposits of hemosiderin is very poorly available to supply iron when needed. Ferritin is the predomi-

nant iron form in most healthy tissues. Hemosiderin may be present in high concentrations as a result of pathology (e.g., iron overload disorders). Iron is also known to play an important role in a number of degenerative diseases (Alzheimer disease, Parkinson disease, Multiple sclerosis and others [19], [64], [23]). In fact it is the cause of the development of toxic products of oxidative stress: even if bound trivalent iron in metalloproteins such as ferritin and hemosiderin represents the "safe" form of iron, free bivalent iron is toxic to the cell [100]. Thus monitoring iron levels can be useful in the search for the etiopathogenic agent responsible for the mentioned neurodegenerative diseases.
Iron accumulation in neurodegenerative diseases results from a cyclic inflammatory process. Inflammation increases local iron content by attracting iron-rich macrophages, disrupting the blood-brain barrier and reducing axonal clearance of iron ([91]). The presence of iron-rich cells and the inability to clear iron on one hand generate free radicals and reactive oxygen species, while on the other hand eventually cause further inflammation and iron deposition, initiating a cyclic process evidenced by the accumulation of iron in neurons and oligodendrocytes, the basal ganglia, and macrophages and microglia seen in postmortem MS brains [55], [26]. Biochemical events surrounding iron-mediated catalytic events give rise to oxidative stress and free radical generation. Neurodegeneration of the deep gray matter may correspond to the cognitive impairment commonly observed in patients with MS.

2.8.1 Iron overload in multiple sclerosis

Many high-resolution MR techniques have shown stored iron regions inside the brain and spinal cord. Sfagos et al. [84] correlated iron overload and MS and revealed variations in the level of protein expression involved in iron homeostasis: the serum concentration of soluble transferrin receptor in a group of MS patients was significantly higher in patients with active MS, in both progressive and relapsing-remitting clinical forms, than in controls. Serum ferritin levels were also significantly elevated in patients affected by the active and progressive form of MS.

It has been observed that the cells involved in iron overload having the

greatest effect on immunity are the macrophages, and that there is a close relationship between iron and the T-lymphocytes, the major cells of adaptive immunity, as they have a major function in recycling the iron from hemoglobin [75]. Moreover, IFN-gamma is produced by T-lymphocytes and seems to be the main mediator of neurodegeneration [11]. However, IFN-gamma is simultaneously responsible for T-lymphocyte apoptosis. Therefore, under normal conditions, a positive feedback loop resulting in a high local concentration of IFN-gamma cannot develop. Several studies have shown the role of iron in T-lymphocyte regulation, and iron induces their refractoriness to IFN-gamma/STAT1 signaling. Thus, iron can determine a longer survival of T-lymphocytes exposed to IFN-gamma, increasing the potentiality of IFN-gamma-mediated neuronal damage [79]. So, as observed in [86], more advances in imaging techniques for iron detection may contribute substantially to understand the role of iron in MS pathology and to develop iron-based biomarkers for disease progression

Chapter 3

Magnetic Resonance Imaging

3.1 A Brief History

Magnetic Resonance Imaging (MRI) is a medical imaging technique used in radiology to visualize the internal structure and functionality of the body. It is based on Nuclear Magnetic Resonance (NMR), a physical phenomenon used to investigate chemical and physical properties in atoms and molecules. It is a relatively new technology. The first MR image was published in 1973 ([54]), when Paul Lauterbur had the idea to spatially encode the nuclear magnetic resonance signal in order to create images. The first studies performed on humans were published in 1977 ([21], [44]). MRI provides greater contrast between the different soft tissues of the body than Computed Tomography (CT). This property makes it very useful in neurological, musculoskeletal, cardiovascular and oncological imaging.

3.2 Basic principles

MRI produces high resolution, high contrast cross-sectional anatomic images through the body but it uses non-ionizing radiation (high intensity magnetic fields and Radio Frequency (RF) electromagnetic fields), and is therefore a non-invasive technique. In MRI, the signals arise from the nuclear magnetic resonance properties of tissues. These properties are stimulated by the application of fixed magnetic field in combination with radio-frequency varying

fields. In particular, MRI creates 3D scans measuring the local response of the nuclei when set into a constant magnetic field and excited with an electromagnetic field of appropriate frequency. The nuclei of ^1H, ^{13}C, ^{19}F, and ^{31}P are important in NMR because they are prevalent in biological systems and provide a NMR signal large enough to be detected above the background noise: this occurs because NMR can be performed only on atoms with a non-zero nuclear spin, i.e., with either an odd atomic number or with an odd mass number. Since a magnetic field is present whenever there are circulating charges, the nucleus must possess a microscopic magnetic field, which has a magnetic moment vector. Moving from the microscopic case to a sample volume of material, there is no preferred orientation for nuclei.
In whole-body MRI, however, we are concerned only with the nuclei of ^1H: given the water and fat content in our bodies, ^1H atoms are present in very high density, thus providing a strong NMR signal.
If the sample volume, i.e. either the whole body or the anatomical district we are interested in, is placed in a magnetic field B_0, the microscopic spins tend to align with the applied external field and the spin system becomes magnetized. This can be modeled using a bulk magnetization vector $\overrightarrow{M}$. B_0 applies a moment to the spins, thus modifying their magnetic moment. Spins wobble about the axis of B_0, so as to describe a cone. This movement is called *precession*. The angular velocity is given by

$$\Omega_0 = \gamma B_0 \tag{3.1}$$

where Ω_0 is the *Larmor frequency* or *precessional frequency*, and γ is the *gyromagnetic ratio* (which is characteristic of the element). Within the B_0 magnetic field, there are more spins aligned with the field (parallel - low energy state) than spins aligned against the field (anti-parallel - high energy state). Due to this slight excess of parallel spins, net magnetization $\overrightarrow{M}$ has a longitudinal component (along the z axis, which is the direction of the external magnetic field) aligned with B_0, i.e. $M_z = M_0$. As spins do not rotate in phase, the sum of all the microscopic transverse magnetizations of each spin is a null transverse macroscopic magnetization, i.e. $M_{xy} = 0$.

3.2.1 RF Excitation and Relaxation

If the spin system in B_0 is upset by his state of thermal equilibrium by a resonant radio frequency pulse B_1 linearly polarized along the x axis, considering the reference system (x', y', z') rotating around the z axis at the Larmor frequency, the total magnetization vector $\overrightarrow{M}$ will precess around x' with angular velocity [60]

$$\omega_1 = -\gamma B_1 \tag{3.2}$$

This type of motion of $\overrightarrow{M}$ is called *forced precession*, because it occurs in response to a deposition of RF energy that comes from outside the sample. The forced precession will lead to a transverse component M_{xy} of $\overrightarrow{M}$. The actual evolution of $\overrightarrow{M}(t)$ is a spiral from the z-axis toward the xy-plane in a clockwise orientation when viewed from the $+z$-axis. The inclination angle of $\overrightarrow{M}$ with its equilibrium direction is called *flip angle*. According the laws of thermodynamics, removed the pulse B_1, $\overrightarrow{M}$ will be back to the earlier equilibrium state. Return to equilibrium of net magnetization is called *relaxation*. During relaxation, electromagnetic energy is retransmitted: this RF emission is called the NMR signal.
Relaxation combines two different mechanisms:

- longitudinal relaxation corresponds to longitudinal magnetization recovery;
- transverse relaxation corresponds to transverse magnetization decay.

Longitudinal relaxation is due to energy exchange between the spins and surrounding lattice (spin-lattice relaxation), re-establishing thermal equilibrium. As spins go from a high energy state back to a low energy state, RF energy is released back into the surrounding lattice. The recovery of longitudinal magnetization follows an exponential curve. The recovery rate is characterized by the tissue-specific time constant T_1. T_1 values are longer at higher field strengths. After time T_1, longitudinal magnetization has returned to 63% of its final value. The equation governing this behavior as a function of the time t after its displacement is:

$$M_z = M_0(1 - e^{-\frac{t}{T_1}}) \tag{3.3}$$

Transverse relaxation results from spins getting out of phase. As spins move together, their magnetic fields interact (spin-spin interaction), slightly modifying their precession rate. These interactions are temporary and random. Thus, spin-spin relaxation causes a cumulative loss in phase resulting in transverse magnetization decay. Transverse magnetization decay is described by an exponential curve, characterized by the time constant T_2. T_2 is tissue-specific and is always shorter than T_1. Transverse relaxation is faster than longitudinal relaxation. T_2 values are unrelated to field strength. After time T_2, transverse magnetization has lost 63% of its original value. The equation governing this behavior as a function of the time t after its displacement is:

$$M_{xy} = M_{xy_0} e^{-\frac{t}{T_2}} \tag{3.4}$$

Two factors contribute to the decay of transverse magnetization.

1. molecular interactions, said to lead to a pure T_2 molecular effect;

2. variations in B_0, said to lead to an inhomogeneous T_2 effect.

The combination of these two factors is what actually results in the decay of transverse magnetization. The combined time constant is T_2^*. The relationship between the T_2 from molecular processes and that from inhomogeneities in the magnetic field is

$$\frac{1}{T_2^*} = \frac{1}{T_2} + \frac{1}{T_{2_{inhomog}}} = \frac{1}{T_2} + \frac{\gamma \Delta B_0}{2} \tag{3.5}$$

So if transverse magnetization of the spins is produced, e.g. by a 90^o pulse, a transient MR signal will result that will decay toward zero with a characteristic time constant T_2^*; this decaying signal is the *free induction decay*.

3.3 Imaging Principles

3.3.1 Magnetic Field Gradient

A magnetic field gradient is a variation in the magnetic field with respect to position. Magnetic field gradients are used in MR imaging in order both to

select the slice plane and to obtain a spatial encoding of each voxel. Gradients are characterized by amplitude, direction, duration and moment of application. Gradients allow the encoding of spatial data as spatial frequency information. The most useful type of gradient in MRI is a one- dimensional linear magnetic field gradient. The symbols for a magnetic field gradient in the x, y, and z directions are respectively G_x, G_y, and G_z.

3.3.2 Spatial encoding

In order to obtain a spatial encoding of each voxel, firstly the desired slice is selected with a slice selection gradient (GSS), applied perpendicular to the desired slice plane. The GSS is added to B_0, so that the protons present a resonance frequency variation proportionate to GSS. An RF wave is simultaneously applied, with the same frequency as that of the protons in the desired slice plane. This causes a shift in the magnetization of the protons on this plane only. Then, within the selected volume, the position of each point must be encoded along the rows (i.e. vertically) by applying a phase encoding gradient (GPE) and along the columns (i.e. horizontally) by applying a frequency encoding gradient (GFE). The GPE, applied for a limited period of time, modifies the spin resonance frequencies, inducing dephasing, which persists after the gradient is interrupted. This results in the protons precessing at the same frequency but with different phases. This phase difference lasts until the signal is recorded.
Finally the GFE is applied when the signal is received, along the horizontal direction, thus modifying the Larmor frequencies in the horizontal direction throughout the time of application: it creates proton columns, which have all an identical Larmor frequency.
All the signals from the same slice are recorded in k-space, then processed to form an image of the slice plane.

3.4 Common MRI Sequences

The NMR signal emitted by the relaxing protons is acquired using a radio frequency coil. In MRI, RF coils serve to both induce spin precession and to

have currents induced in them by the spin system. Coils are only sensitive to variations of transverse magnetization vector. The decay of M_{xy} induces a sinusoidal FID, which depends on T_1, T_2 and ρ, which is the proton density of the tissue. Contrast in MR images is produced by manipulating the RF excitation pulse sequence to produce MR signals that are influenced by different weighted contributions of ρ, T_1 and T_2.

The architecture of a sequence consists of a combination of radiofrequency pulses and gradients. Different sequences are designed in order to highlight the signal of a particular tissue, while limiting both acquisition time and artifacts, without altering the SNR. Essential components for any imaging sequence are:

- an RF excitation pulse;
- gradients for spatial encoding (2D or 3D), whose arrangement will determine how the k-space is filled;
- a signal reading.

Various options are analyzed for setting a sequence: they usually comprehend other radiofrequency pulses, gradients or variable reconstruction methods, which can be combined to modify the contrast, or to accelerate the sequence, or to reduce artifacts. Besides, a series of other parameters (Repetition Time (TR), Echo Time (TE), flip angle, turbo factor, field of view matrix (FOV)...) can be used to find the best compromise between contrast, spatial resolution and speed.
There are two main sequence families, i.e. Spin-Echo (SE) and Gradient-Echo (GE) sequences. Each of them is characterized by the type of echo recorded. Besides, numerous variations have been developed within each of these families.

3.4.1 Spin Echo Sequences

Pure transverse relaxation, characterized by the time constant T_2, is a random phenomenon. The fact that the FID decays faster, with time constant T_2^*, is due to fixed perturbations in the magnetic field. These fixed perturbations

cause the precession of some spins to speed up and others to slow down (relative to the nominal rate of rotation predicted by the Larmor frequency). In a brief period, nearby spins are largely dephased. The existence of spin echoes is due to the fact that the faster (slower) spins, which now lead (lag) the spin system, can be made lag (lead) the spin system using a short-duration 180^o pulse. From this new phase position, the fast spins "catch up" and the slow spins "fall back", forming a spin echo. Thus, a spin echo is the signal that is generated by the transverse spins recovering their coherence after loss of coherence followed by a deliberate 180^o RF pulse. The time interval from the initial 90^o pulse to the formation of the spin echo is known as the echo time and is given the symbol TE. This time is under our control, because we specify the application time of the 180^o pulse, which is at TE/2. The spin echo sequence is made up of a series of events

- 90^o pulse
- 180^o rephasing pulse at TE/2
- signal reading at TE.

This series is repeated at each time interval TR. With each repetition, a k-space line is filled, thanks to a different phase encoding. The signal from a spin echo sequence is

$$S \propto \rho(1 - e^{-\frac{TR}{T_1}})e^{-\frac{TE}{T_2}} \tag{3.6}$$

3.4.2 Gradient Echo Sequences

In a gradient echo sequence, there is no refocusing 180^o pulse and the data are sampled during a gradient echo, which is achieved by dephasing the spins with a negatively pulsed gradient before they are rephased by an opposite gradient with opposite polarity to generate the echo. Besides the absence of the 180^o rephasing pulse, GR sequences are characterized also by a flip angle usually lower than 90^o (partial flip angle). In this way the amount of magnetization tipped into the transverse plane is decreases. The consequence of a low-flip angle excitation is a faster recovery of longitudinal magnetization that allows a shorter TR/TE and a decreases scan time. The advantages

of low-flip angle excitations and gradient echo techniques are faster acquisitions, adjustable contrasts between tissues and a stronger MR signal in case of short TR. As already observed in 3.2.1, the actual decay of M_{xy} is due to different factors: molecular interactions (i.e. spin-spin tissue-specific relaxation), which account for pure T_2 effect, and B_0 field inhomogeneities and tissues' magnetic susceptibility. As GE techniques use a single RF pulse and no 180^o rephasing pulse, the relaxation due to fixed causes is not reversed and the loss of signal results from T_2^* effects (pure T_2 + static field inhomogeneities). The signal obtained is thus T_2^*-weighted rather than T_2-weighted. These sequences are thus more sensitive to magnetic susceptibility artifacts than spin echo sequences. The signal arising from a GE is

$$S \propto \rho(1 - e^{-\frac{TR}{T_1}})e^{-\frac{TE}{T_2^*}} \tag{3.7}$$

3.4.3 Inversion Recovery Sequences

Inversion-recovery is a magnetization preparation technique followed by an imaging sequence of either the spin echo or the gradient echo type. It can be used to null the signal of a single tissue. To better understand the principle of inversion recovery, an inversion recovery sequence which uses a spin-echo sequence to detect the magnetization will be briefly described as example. The RF pulses are 180-90-180. An inversion recovery sequence which uses a gradient-echo signal detection is similar, with the exception that a gradient-echo sequence is substituted for the spin-echo part of the sequence.
The sequence starts with a 180^o RF inversion wave which flips longitudinal magnetization down to the $-z$ axis. Longitudinal magnetization will then relaxate and increase to return to its initial value, passing through null value. Before it reaches equilibrium, after a time TI (Inversion Time), a 90^o pulse is applied which rotates the longitudinal magnetization into the XY plane. Here the magnetization rotates about the z axis and dephase, giving a FID, and is usually rephased with a 180^o pulse as in the spin echo sequence. The entire sequence is repeated every TR seconds. The signal as a function of TI when the sequence is not repeated is

$$S \propto \rho(1 - 2e^{-\frac{TI}{T_1}}) \tag{3.8}$$

and it crosses zero for $TI = T_1 ln2$. The signal from a repeated inversion recovery sequence which uses a spin echo to record the signal is

$$S \propto \rho(1 - 2e^{-\frac{TI}{T_1}} + e^{-\frac{TR}{T_1}})e^{-\frac{TE}{T_2}} \tag{3.9}$$

The inversion recovery sequence has the advantage that, choosing the appropriate TI, it can provide very strong contrast between tissues having different T1 relaxation times or to suppress tissues like fluid or fat. On the other hand, the disadvantage is that the additional inversion RF pulse makes this sequence less time efficient than the other pulse sequences. So, the aim of an IR sequence is to suppress the contribution of a specific tissue, choosing the proper value of TI. The most common examples are the STIR (Short TI Inversion Recovery) sequence [12], where TI is chosen to suppress fat, and FLAIR (FLuid Attenuated Inversion Recovery) sequence [80], where TI is chosen to suppress cerebrospinal fluid.

3.5 MRI sequences for brain lesions detection

3.5.1 Fluid Attenuated Inversion Recovery

FLAIR (FLuid Attenuated Inversion Recovery) is an inversion recovery technique that nulls fluid contributions in the image. In this thesis, it is used in the brain imaging to suppress cerebrospinal fluid (CSF). Additionally, in such a way periventricular lesions caused by MS plaques become hyperintense with respect to the background.
Gray matter and white matter are characterized by a similar T_1 value, which on the contrary is much shorter than CSF T_1 value (Table 3.1). This fact can be exploited choosing a TI equal to $TI = T_{1,CSF} ln2$, so to acquire the signal when the contribution of CSF is equal or at least close to zero.
The maximum number of slices that can be acquired in one TR is determined either by the time period TI or by (TR-TI), whichever is shorter. A longer TR will result in a more complete recovery of magnetization, in better signal-to-noise ratio and increased contrast-to-noise ratio between the lesion on one hand and gray and white matter on the other hand.

3.5.2 Double Inversion Recovery

More recently, a double inversion recovery (DIR) pulse sequence has been introduced [78]: it provides two different inversion pulses, which attenuate the CSF *and* the whole white matter, thus achieving a superior delineation between gray and white matter. This sequence consists of two inversion pulses preceding a conventional spin-echo sequence. In the interval TI_1 between the two inverting pulses, brain tissue magnetization recovers almost fully, while CSF recovers to only a small fraction of M_0. The second inversion interval TI_2 is chosen to null white matter magnetization. Gray matter, having a longer T_1 (Table 3.1), remains negative thus generating a MR signal. In order to null the signals from the two tissues, it is necessary to choose TI_1 and TI_2 to satisfy

$$1 - 2E_2 + 2E_1E_2 - E_c(2E_\tau^{-1} - 1) = 0 \tag{3.10}$$

at both T_1 values, i.e. the T_1 of CSF and the T_1 of white matter. In 3.10 the variables are respectively

$$E_1 = e^{-\frac{TI_1}{T_1}}$$

$$E_2 = e^{-\frac{TI_2}{T_1}}$$

$$E_c = e^{-\frac{TR}{T_1}}$$

$$E_\tau = e^{-\frac{\tau}{T_1}}$$

To satisfy these conditions, it turns out that the required TR results quite long. Anyway, thanks to rapid spin-echo acquisition the overall acquisition time is reduced to levels appropriate for the clinical use.

3.5.3 Gradient Spin Echo

In general, faster scanning can be achieved by either spending less time per profile or by acquiring fewer profiles. The former approach leads to a lower SNR, while the latter causes a lower spatial resolution and a possible lower SNR. An alternative is to sample more than one profile per excitation, which can be currently done with different MR methods, among which two primary examples are echo-planar imaging (EPI) and turbo spin echo (TSE) imaging.

Table (3.1). *Typical tissue parameters measured at 1.5T*

Tissue	T1 [ms]	T2 [ms]
Water	3000	300
CSF	2650	280
Gray matter	810	100
White matter	680	90
Fat	240	85
Gadolinium	Reduces T_1	Reduces T_2

It is possible to combine the TSE and EPI methods: in particular GRASE (GRadient And Spin Echo) imaging uses a train of refocusing 180^o RF pulses, but for each spin echo of the readout, there are additional gradient recalled echoes. Proposed in [29], in this sequence several gradient echo trains are recorded during each TR, with a signal weighting of the spin echo type. Each echo has a different phase encoding to fill the k-space faster. The advantage of using intermediary gradient echos rather than spin echos (as in ultrafast spin echo sequences) is to reduce the number of 180^o rephasing pulses, thereby reducing the quantity of radiofrequency energy deposited.

3.6 MRI methods for tissue iron detection and quantification in the brain

As already said in 2.8, endogenous tissue iron, other than that in blood, occurs primarily as ferritin iron and hemosiderin iron [9]. In MRI they can be considered as natural contrast agents ([25]). Their MRI detectability is due both to their relative abundances as well as to their high magnetic susceptibilities. The latter, in particular, makes them generate substantial magnetic field inhomogeneities when placed in a strong magnetic field B_0. These field inhomogeneities cause proton spin dephasing and increase the transverse relaxation rate. Iron-sensitive MRI techniques provide useful non-invasive approaches for the monitoring of iron concentration and deposition. Actually, quantification is confounded by the fact that the spatial pattern of tissue iron

deposition is often complex and varies with tissue type and pathology [36]. In addition, ferritin and hemosiderin iron can alter the MR signal in significantly different ways.

Among the great variety of MRI sequences, gradient echo sequences (GES) are simple, fast, and universally available. Iron concentration quantification is mostly based on the R_2^* relaxation rate (being $R_2^* = 1/T_2^*$) calculated from monoexponential fits to the GES signal decay [104]. Both single echo and multiple echo GES can be used for R_2^* estimation, with the multiple echo approach usually being more efficient and accurate. For iron quantification, R_2^* is normally taken to be linearly related to the iron concentration [52].

Chapter 4

Brain Segmentation

4.1 State of Art

In biomedical imaging, brain segmentation has been an important issue for the last decades. So far, many of the algorithms implemented for the segmentation of the brain have been developed in order to work on T1-weighted MRI volumes, even if some have been designed to work on different types of acquisition ([5], [43]).
Currently, the most used software to perform both brain segmentation and the segmentation of gray matter, white matter and CSF in MRI are:

- SPM (Statistical Parametric Mapping), written by the Wellcome Department of Imaging Neuroscience at University College London, UK) [2];
- FSL (FMRIB Software Library), written by the Analysis Group, FMRIB, Oxford, UK [88];
- FreeSurfer, written by a collaboration between the Massachusetts Institute of Technology and the Harvard University, USA [20].

Both for brain segmentation and for brain tissue extraction, SPM uses an approach based on probabilistic atlases combined with fuzzy clustering.
As far as brain segmentation is concerned, FSL combines an approach based on intensity distributions analysis and deformable models [89]. For GM, WM and CFS, instead, FSL combines an approach based on maximum likelihood classification with hidden Markov Random Fields [106].

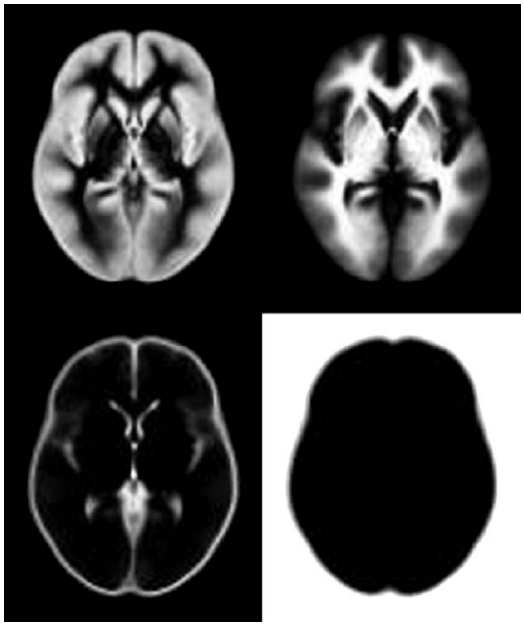

Figure (4.1). *The tissue probability maps for gray matter, white matter, CSF, and "other".*

Lastly, in order to extract brain volume, FreeSurfer combines an approach based on watershed algorithms, deformable surfaces and brain atlases [82]. It shall be noticed that Freesurfer is very time consuming compared to other software (the processing of one scan can consume 12-24 hours in comparison with the 15-30 minutes requested by FSL and SPM). For the different tissues segmentation, FreeSurfer combines an approach based on template matching, and intensity, geometry and connectivity analysis ([20], [30]).

4.1.1 SPM

Tissue classification in SPM requires the images to be registered with tissue probability maps ([3]). After registration, these maps represent the prior probability of different tissue classes being found at each location in an image. Bayes rule can then be used to combine these priors with tissue type probabilities derived from voxel intensities to provide the posterior probability (Fig. 4.1). For an extensive description of the method, see [2]

This procedure is inherently circular, because the registration requires an

initial tissue classification, and the tissue classification requires an initial registration. This circularity is resolved by combining both components into a single generative model, which also includes parameters that account for image intensity nonuniformity. Estimating the model parameters involves alternating among classification, bias correction, and registration steps. This approach provides better results than simple serial applications of each component.

In the overall procedure, additional *a priori* information is used, based on other subjects' brain images. Priors are usually generated by registering a large number of subjects together, assigning voxels to different tissue types and averaging tissue classes over subjects. The data used by SPM are a modified version of the ICBM (International Consortium for Brain Mapping) Tissue Probabilistic Atlas, available on line. They consist of tissue probability maps of grey and white matter and of CSF (see Fig. 4.1). A fourth class is also used, which is simply one minus the sum of the first three. These maps give the prior probability of any voxel in a registered image being of any of the tissue classes, irrespective of its intensity. The current implementation uses tissue probability maps for grey matter, white matter, and CSF, although maps for additional tissue types (e.g., blood vessels) could also be included.

A nonlinear deformation field is estimated that best overlays the tissue probability maps on the individual subjects' image. The original data are derived from 452 T_1-weighted scans, which were aligned with an atlas space, corrected for scan inhomogeneities, and classified into GM, WM and CSF. These data were then affine registered to the Montreal Neurological Institute (MNI) space and downsampled to 2 mm resolution. A common way to follow in order to overcome possible volume alignment problems consists in manually repositioning the images so that the anterior commissure is close to coordinate 0,0,0 and the orientation is within a few degrees of the tissue probability map data. SPM provides a *Display* option that allows the manual realignment. However, this implies the intervention of a human inspector, a fact that is always undesirable, especially when dealing with huge amount of data.

4.1.2 FSL

Tissue segmentation in FSL requires the images to be preprocessed with the Brain Extraction Tool (BET), in order to remove the non-brain tissues. The algorithm starts with an initial estimation step to obtain initial tissue parameters and classification. It is then followed by a three-step Expectation Maximization (EM) process which updates the class labels, tissue parameters and bias field iteratively. During the iterations, an MRF-MAP (Markov random field- maximum a posteriori) approach is used to estimate class labels, MAP is applied to estimate the bias field, and the tissue parameters are estimated by maximum likelihood (ML). The resulting output from the algorithm is tissue segmentation, bias field estimation and a restored version of the image. As it has explicitly declared by the authors ([106]), the problem of MRI segmentation is focused on segmenting normal brains without apparent diseases into three tissues: gray matter, white matter and cerebrospinal fluid.

4.1.3 FreeSurfer

FreeSurfer's subcortical processing pipeline uses a probabilistic approach to perform automated labeling of 37 brain structures, where each voxel in the MR image volume is classified using a probabilistic atlas generated by a training set of 41 manually labeled brains. The procedure includes a neighborhood function to encode spatial information, a forward model of the MR scanner parameters to improve sequence independence, and a non-linear function to account for morphological differences between the atlas and the target brain. It shall be noticed that FreeSurfer is very time consuming compared to other software (the processing of one scan can consume 12-24 hours in comparison with the 15-30 minutes required by FSL and SPM). Segmentation of brain images requires a statistical atlas for providing prior information about the spatial position of different structures. A major limitation of atlas-based segmentation algorithms is their deficiency in analyzing brains that have a large deviation from the population used in the construction of the atlas. More details can be found in [39].

In order to understand the performance of the software at the state of the art, two recent publications shall be analyzed. In particular, [96] described the values that are shown in Table 4.1 in the evaluation of the sensitivity and specificity of SPM and FSL on the Internet Brain Segmentation Repository (IBSR). Shattuck et al. [85] obtained the values that are shown in Table 4.2 during the evaluation of the Jaccard index [45] and of the Dice index [24], the Sensitivity and the Specificity of the software on which are based FSL and FreeSurfer. This comparison is performed on the on-line segmentation validation engine realized by the Laboratory of Neuro-Imaging (LONI) of the University of California, Los Angeles.

Table (4.1). *Brain segmentation metrics computed for FSL and SPM on the IBSR dataset*

Algorithm	Sensitivity	Specificity
FSL	0.746	0.986
SPM	0.780	0.988

Table (4.2). *Brain segmentation metrics computed for FSL and FreeSurfer on the LONI Segmentation Validation Engine*

Algorithm	Jaccard	Dice	Sensitivity	Specificity
FSL	0.9400 ± 0.0089	0.9691 ± 0.0048	0.9627 ± 0.0117	0.9957 ± 0.0014
FreeSurfer HW A3	0.8537 ± 0.0184	0.9210 ± 0.0107	0.9992 ± 0.0003	0.9695 ± 0.0053

What is worth noting for the purpose of this chapter is that the reported indexes values can still be improved for SPM, FSL and Freesurfer. More importantly, the results proposed have not be obtained on brains of MS patients, which are typically source of misclassification.

4.1.4 Main Problems

One common problem is represented by the fact that when working either with specific pulse MR sequences or on images acquired from patients suffer-

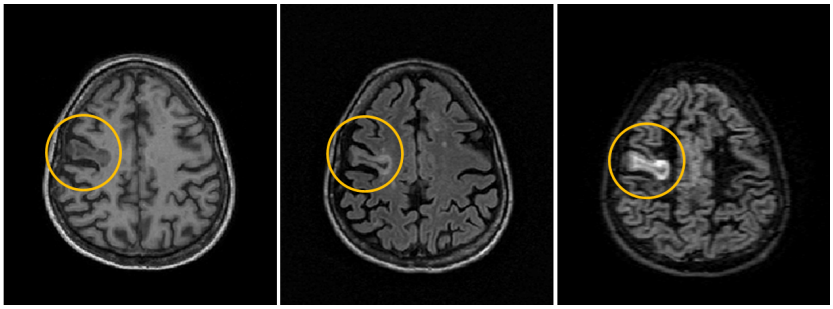

Figure (4.2). *T_1-weighted MR image (left panel) and corresponding FLAIR MR image (central panel) and DIR MR image (right panel). A big MS lesion is highlighted by the circle in the three images.*

ing from specific diseases, segmentation methods that use both intensity and *a priori* anatomic information do not perform at their best. In fact, as pointed out by [66], the use of general-purpose software to segment MR images of MS patients often results in misclassification of MS lesions as gray matter due to overlapping intensity values. The consequence is that an operator is required to check the automatic segmentation and to manually correct it, an operation that is time consuming and that introduces operator variability into the measurements.

An example of uncorrect tissue segmentation is reported: in the proposed case we have a subject affected by MS, with a large type I lesion extending through both white matter and gray matter (Fig. 4.2). As it can be seen in the T_1-w MR image (which is the MR sequence mostly used to perform tissues segmentation), the appearance of both white and gray matter is altered by the lesion. Consequently, the automatic segmentation provided by these software may result uncorrect.
In particular, in Fig. 4.3 the segmentation of the same volume reported in Fig. 4.2, as provided by the FAST segmentation tool of FSL is shown. The detail of the lesion is magnified (Figure 4.4) to better appreciate the problem represented by multiple sclerosis. The entire gyrus results misclassified because of an error which occurred in the brain extraction phase, performed by the BET tool of FSL (Figure 4.5). In order to verify if the problem is solely related to the BET tool, we tried to extract the brain changing the default parameters, so that a bigger mask of the brain is obtained. In such a way we inevitably

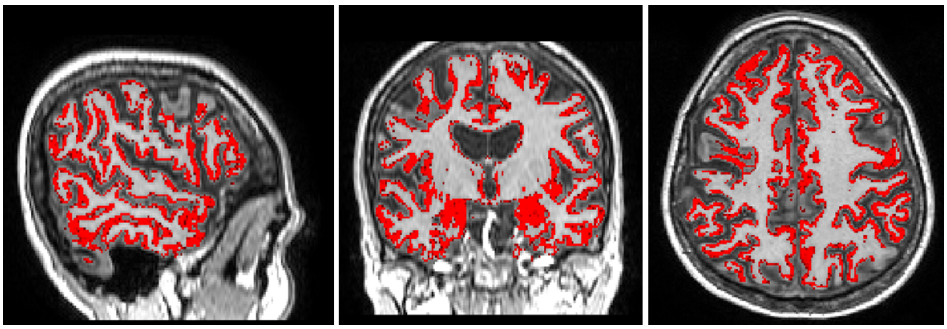

Figure (4.3). *T_1-weighted sequence: sagittal (left panel), coronal (central panel) and axial (right panel) view with superimposed the gray matter segmentation obtained with FAST (FSL).*

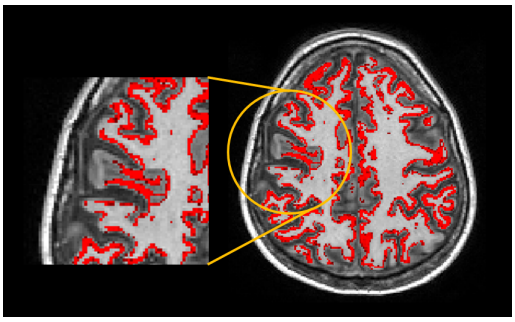

Figure (4.4). *T_1-weighted sequence: axial (right panel) view with with superimposed the gray matter segmentation obtained with FAST (FSL). On the left panel, a zoom of the region in which the segmentation is uncorrect.*

include some voxels of the scalp. The new segmentation obtained is shown in Figure 4.6: though now the gyrus is correctly segmented, this is obtained at the cost of the misclassification of the adjacent white matter.

In order to make a comparison, we segmented the same T_1-w volume using SPM. At first we left all the parameters at their default values. The obtained segmentation is shown in Fig. 4.7: the strikingly unsuccessful results are due to the poor alignment between the images to be segmented and the tissue probability map used by SPM. Different tricks can be devised to bypass the problem of the coregistration of the T_1-w volume on the MNI space: we found for instance possible to use FSL to coregister the MNI atlas on the T_1-w volume: this step requires a transformation matrix that can be subsequently used to change the SPM priors on the T_1-w space. Afterwards the segmentation can be performed on SPM using as priors those just moved on the T_1-w.

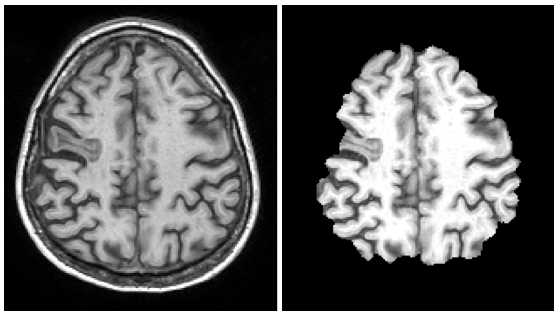

Figure (4.5). *Brain extractions: original T_1-weighted axial slice (right panel) and brain extraction obtained with BET (FSL) (left panel).*

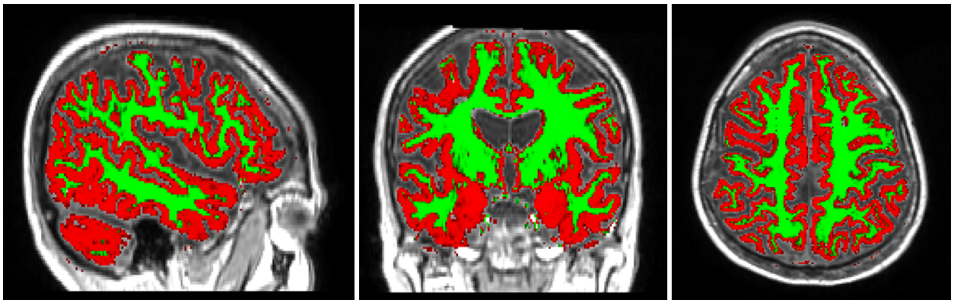

Figure (4.6). *T_1-weighted sequence: sagittal (left panel), coronal (central panel) and axial (right panel) view with superimposed in red the gray matter segmentation and in green the white matter segmentation obtained with FAST (FSL).*

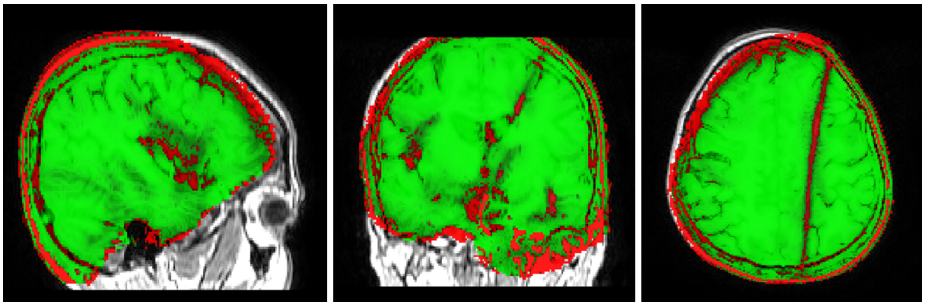

Figure (4.7). *T_1-weighted sequence: sagittal (left panel), coronal (central panel) and axial (right panel) view with superimposed the gray and white matter segmentation obtained with SPM with a poor alignment between the images to be segmented and the tissue probability maps.*

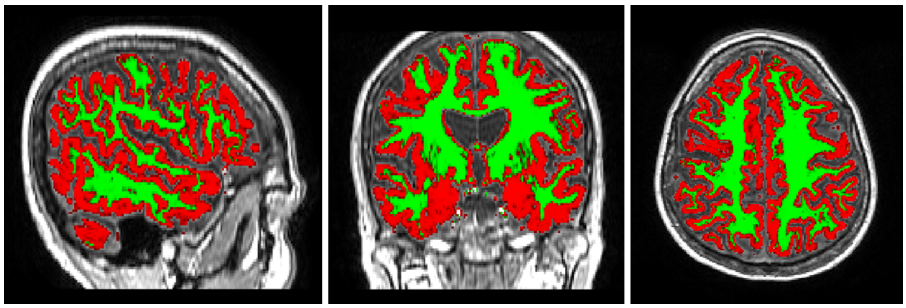

Figure (4.8). *T_1-weighted sequence: sagittal (left panel), coronal (central panel) and axial (right panel) view with superimposed, in red the gray matter segmentation and in green the white matter segmentation obtained with SPM after a correction of the prior used by the algorithm.*

The results obtained are shown in Fig. 4.8, where the red and green pixels stand respectively for GM and WM. The segmentation appears much more satisfactory, even though the region in the proximity of the type I lesion still results uncertain.
Finally, we tried to segment the same subject using FreeSurfer. With this software, the use of three T_1-w sequences is recommended: they are averaged in order to minimize possible mistakes due to artifacts. Also in this case the result is unsatisfactory (Fig. 4.9): the cortical lesion highlighted in Fig. 4.2 is missed and causes the segmentation process to fail in delimiting the gray matter borders.

Besides, [66] and [32] claim that these methods are not only prone to classification errors due to partial volume effects between MS lesions and normal

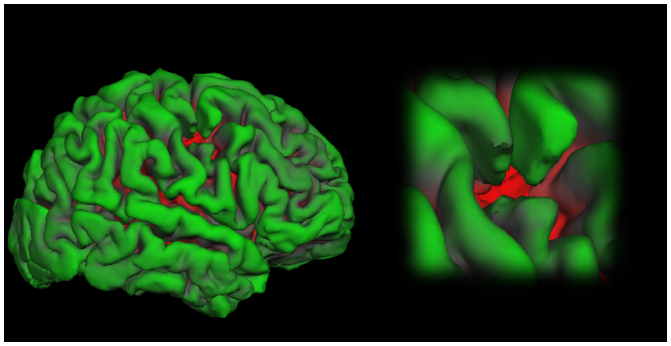

Figure (4.9). *Three dimensional rendering of the brain reconstruction obtained with FreeSurfer (left). Magnification in the correspondence of the cortical lesion (right).*

tissue, but also that when image data have not been acquired using optimal sequences for use with one of the widely available segmentation tools, a customized segmentation method may be required to obtain accurate results.
In our work we are dealing with all the problems described. On one hand we are using FLAIR and DIR MRI sequences instead of the usual T_1-weighted sequence. On the other we are working on images acquired from MS patients, which are often anomalous in their appearance due to the tissue structural changes caused by the disease. This is the reason why we have decided to follow a different (brand new) approach, which exploits the advantages, mainly in term of contrast-to-noise ratio, of the two specific MR sequences, while avoiding the use of any anatomical a priori information, which may be misleading in the presence of a disease. In particular, the brain extraction and the gray matter segmentation are obtained using the level set method, a numerical technique used in image analysis to segment objects and shapes. In the next section, the level set theory and implementation will be described.

4.2 Methods

4.2.1 Level Set Method

Implicit Functions

Suppose we divide the real Cartesian plane $\mathbb{R}^2$ into separate subdomains with nonzero areas. For example, consider the curve $\phi(\vec{x}) = x^2 + y^2 - 1$ in $\mathbb{R}^2$ and an interface defined by $\phi(\vec{x}) = 0$. We refer to $\Omega^- = \{\vec{x} || \vec{x}| < 1\}$ as the *inside portion* of the domain, while the *exterior region* is $\Omega^+ = \{\vec{x} || \vec{x}| > 1\}$. The interface defined by the $\phi(\vec{x}) = 0$ isocontour is explicitly represented by the unit circle defined by $\partial\Omega = \{\vec{x} || \vec{x}| = 1\}$. Hereafter we will limit our interface curves to *closed curves*, so that the interior and exterior regions will be clearly defined. Note that in an *explicit* interface representation the points that belong to the interface are explicitly defined, which in our example correspond to $\partial\Omega = \{\vec{x} || \vec{x}| = 1\}$. In an *implicit* interface representation, instead, interfaces are defined as the isocontour of some function (usually the zero-isocontour). The explicit interface definition needs to specify all the points on a curve, a fact that, moving from the proposed simplifying example, can be difficult for general curves. Curves might need to be parametrized with a vector function $\vec{x}(s)$, where s is a parameter in $[s_0, s_{end}]$ and, being the curve closed, $\vec{x}(s_0) = \vec{x}(s_{end})$. It is worth noting that two-dimensional curves may become so complicated that it is convenient to approximate their explicit representation; to do so, the parameter s is discretized into a finite set of points $s_0 < ... < s_{i-1} < s_i < s_{i+1} < ... < s_{end}$, where the intervals $[s_i, s_{i+1}]$ can in general be of different size.

Dealing with the discretized problem in the implicit representation case, we discretized a bounded subdomain $D \subset \mathbb{R}^2$, and within D we choose a finite set of points $(x_i, y_i), i = 1, ..., N$ to discretely approximate the implicit function ϕ. Note that while in the explicit representation the discretization needs to resolve only a one-dimensional set $[s_0, s_{end}]$, in the implicit representation the discretization needs to resolve a two-dimensional region D. This concept can be generalized in $\mathbb{R}^n$ and represents a potential drawback of the implicit surface representation. The problem can be overcome considering that only the isocontour $\phi(\vec{x}) = 0$ is important. Therefore to accurately represent the inter-

face only the points $\vec{x}$ close to the isocontour are needed, and the rest of D can be left unresolved. Working with the implicit representation assures a series of advantages and powerful geometric tools. For example, it is straightforward to determine which side of the interface a point is on, by looking at the local sign of ϕ. Besides, if ϕ_1 and ϕ_2 are two implicit functions, their union and intersection are simple to be determined by using Boolean operations. Let us define some important operators that will be used throughout the chapter. The *gradient* of an implicit function ϕ is defined as

$$\nabla\phi = (\frac{\partial\phi}{\partial x}, \frac{\partial\phi}{\partial y}, \frac{\partial\phi}{\partial z}) \tag{4.1}$$

It is perpendicular to the isocontours of ϕ and it points in the direction of increasing ϕ. For points on the interface, i.e. points $\vec{x}_0$ on the zero isocontour ϕ, the *unit outward normal* is

$$\vec{N} = \frac{\nabla\phi}{|\nabla\phi|}. \tag{4.2}$$

Functions ϕ should be chosen to be smooth. The mean curvature of the interface is defined as the divergence of the normal, that is

$$\kappa = \nabla \cdot \vec{N} = \nabla \cdot (\frac{\nabla\phi}{|\nabla\phi|}) \tag{4.3}$$

so that it can be written in terms of the first and second derivatives of ϕ.
All the properties and definitions described so far hold also for the so-called *signed distance functions*, a subset of the implicit functions ϕ with $|\phi(\vec{x})| = d(\vec{x})$ for all $\vec{x}$, where $d(\vec{x})$ is a distance function defined as

$$d(\vec{x}) = min(|\vec{x} - \vec{x}_I|) \quad \forall\vec{x}_I \in \partial\Omega. \tag{4.4}$$

What is important is that in addition to all the properties of implicit functions, there are new properties that only signed distance functions possess. In particular, since d is Euclidean distance, $|\nabla d| = 1$, which turns into $|\nabla\phi| = 1$. Besides, they are monotonic across the interface, thus they can be differentiated.

Level Set Motion

As described in [70], level set methods add dynamics to implicit surfaces, that is they embed in a time-dependent equation the movements of an implicit surface. We will now summarize the concepts and laws to describe in an analytical way the moves of implicit surfaces.

Motion in an externally generated velocity field. Suppose that the velocity of each point on the implicit surface is given as $\vec{V}(\vec{x})$, and that $\vec{V} = \langle u, v, w \rangle$ is the velocity field describing the velocity with which we want to move all the points on the surface. There are two different approaches to deal with this problem: we can choose either to use a Lagrangian formulation, or to use an Eulerian formulation. In the former case, we have to solve the ordinary differential equation

$$\frac{d\vec{x}}{dt} = \vec{V}(\vec{x}) \tag{4.5}$$

for every point $\vec{x}$ on the front. This approach, unfortunately, can raise problems with numerical instabilities and in general with deformations of boundary elements (segments or triangles, respectively in 2D and in 3D). To avoid such problems, an Eulerian formulation is preferable. In particular, we use an implicit function ϕ not only to represent the interface, but also to evolve it. The evolution of ϕ can thus be defined by the convection equation

$$\phi_t + \vec{V} \cdot \nabla\phi = 0 \tag{4.6}$$

where the t subscript denotes a temporal derivative in the time variable t, and the partial differential equation defines the motion of the interface, i.e. where $\phi(\vec{x}) = 0$. Equation 4.6, introduced for numerical interface evolution in [69], is usually referred to as the *level set equation*.
Thanks to a Cartesian grid, we can apply numerical methods to find the proper representation of ϕ at the time t^n, that is, we are able to update ϕ in time by finding the new values of ϕ at every grid point after some time increment $\triangle t$. A *grid* is a set of data points where ϕ is defined. It is usually convenient to choose uniform, isotropic Cartesian grids, i.e. grids defined as $\{(x_i, y_i) | 1 \leqslant i \leqslant m, 1 \leqslant j \leqslant n\}$, with all the subintervals $[x_i, x_{i+1}]$ and $[y_i, y_{i+1}]$

equal in size. In this way, a first-order method for time discretization of 4.6 is the *forward Euler method*

$$\frac{\phi(t^{n+1}) - \phi(t^n)}{\triangle t} + \vec{V}(t^n) \cdot \nabla\phi(t^n) = 0. \tag{4.7}$$

The velocity field gradient can come from a number of external sources and in general it depends on both space and time, i.e., it is $\vec{V}(\vec{x}, t)$. Interface motion can be driven not only by externally generated velocity fields, but also by internally generated velocity fields. In the next sections two common examples will be proposed.

Motion involving mean curvature. A self generated velocity field $\vec{V}$ can depend directly on the level set function ϕ. In particular, we consider motion by mean curvature where the interface moves in the normal direction with a velocity proportional to its curvature, i.e. $\vec{V} = -b\kappa\vec{N}$, where b is a non negative constant and κ is the curvature. Considering that the velocity field for motion by mean curvature contains a non-zero component in the normal direction only, we can rewrite the general equation eliminating the tangential component, which is identically zero.
In the two dimensional case, the vector field $\vec{V}$ can be decomposed as $\vec{V} = V_n\vec{N} + V_t\vec{T}$, where $\vec{N}$ and $\vec{T}$ are respectively the normal and the tangent vector of every point of ϕ. Since $\vec{N}$ and $\nabla\phi$ point in the same direction, it follows that $\vec{T} \cdot \nabla\phi = 0$ for any $\vec{T}$. So, substituting $\vec{V}$ in Eq. (4.6) with the obtained decomposition, what we are left with is

$$\phi_t + V_n\vec{N} \cdot \nabla\phi = 0. \tag{4.8}$$

Besides, since

$$\vec{N} \cdot \nabla\phi = \frac{\nabla\phi}{|\nabla\phi|} \cdot \nabla\phi = \frac{|\nabla\phi|^2}{|\nabla\phi|} = |\nabla\phi|, \tag{4.9}$$

equation 4.8 can be written as

$$\phi_t + V_n|\nabla\phi| = 0. \tag{4.10}$$

Also Eq. (4.10) is known as the *level set equation*, but it is used for internally self-generated velocity fields, whereas 4.6 does not make any assumption on $\vec{V}$.

Balloon motion. An internally generated velocity field can be designed in order to induce a constant motion of the interface in the normal direction. A velocity field like this is defined by $\vec{V} = a\vec{N}$, where a is a constant. The corresponding level set equation is

$$\phi_t + a|\nabla\phi| = 0. \tag{4.11}$$

The interface is moving in the normal direction with speed a.

We can add all the three contribution to obtain a more general equation of motion, that is

$$\phi_t + \vec{V_{ext}} \cdot \nabla\phi + a|\nabla\phi| = b\kappa|\nabla\phi|. \tag{4.12}$$

This equation combines an external velocity field, a motion normal to the interface and a motion by mean curvature.

4.2.2 Active Contour Models and Level Sets

Since their invention by Kass et al., [47], active contour models have been widely used for image segmentation. The existing active contour models can be categorized into two classes: *edge-based models*, which typically use image gradient to stop the evolving contours on the object boundaries ([56], [57]) and *region-based models* ([14], [71]), which in general have better performance for the image with weak object boundaries, in addition to being less sensitive to the location of initial contours.

Among the most used techniques of active contours without edges, Chan and Vese [14] proposed the piecewise constant (PC) model, in which an image is assumed to be composed of statistically homogeneous regions. Later on, the same authors found a way to handle more general scenario, e.g. images in which the regions of interest are not statistically homogeneous. To do so, they proposed the so called piecewise smooth (PS) model [99], built on the minimization of Mumford-Shah functional. However, as observed by [58], for

images with intensity inhomogeneity, PC model can result in a contour that is still far away from the object boundary.

As we have already said, intensity inhomogeneity typically appears in MR images, due either to non-uniform magnetic field produced by radio-frequency coils and from object susceptibility. For this reason, the approach proposed in [58] has been chosen as a starting point from which to deal with the gray matter segmentation. The basic idea of the cited work is to introduce a kernel function to define a local binary fitting energy in a variational formulation, so that local intensity information can be embedded into a region-based active contour model. Then the local binary fitting energy functional is further incorporated into a variational level set formulation without reinitialization already proposed by [57].

For our specific problem, for a given open region Ω with smooth boundary we assume the existence of a level set function $\phi(x, y)$, which is Lipschitz continuous, satisfying

$$\phi(x,y) > 0 \quad for (x,y) \in \Omega \tag{4.13}$$

$$\phi(x,y) = 0 \quad for (x,y) \in \partial\Omega \tag{4.14}$$

$$\phi(x,y) < 0 \quad for (x,y) \in \overline{\Omega}^c \tag{4.15}$$

Then we can obtain the length of $\partial\Omega$ and the area inside Ω by using the double integrals

$$\mathcal{L}(\phi) = \int\int \delta(\phi(x,y))|\nabla(\phi(x,y))|dxdy \tag{4.16}$$

$$\mathcal{A}(\phi) = \int\int H(\phi(x,y))dxdy \tag{4.17}$$

where $H(x)$ is the Heaviside function and $\delta(x)$ is the Dirac delta function, in the sense of distributions. To cope with numerical implementation, slightly regularized versions of $\delta(x)$ and $H(x)$ have to be used, i.e. the Heaviside function needs to be approximated by a smooth function H_ε defined by

$$H_\varepsilon(x) = \frac{1}{2}[1 + \frac{2}{\pi}\arctan(\frac{x}{\varepsilon})]. \tag{4.18}$$

Consequently, the derivative of H_ε is the smooth function

$$\delta_\varepsilon(x) = H'_\varepsilon(x) = \frac{1}{\pi}\frac{\varepsilon}{\varepsilon^2 + x^2}. \tag{4.19}$$

In order to properly segment the MR images we are provided with, we used an approach based on the work of Li et al. [58], who introduced in the well established active contour models the idea of a local binary fitting energy with a kernel function. The aim of this work is to overcome the limitation of piecewise constant models [14], thus allowing to segment images with intensity inhomogeneity. The choice was considered to be suitable because of the characteristics of the images we have to segment: in particular, we are looking for tissues which can be delimited by smooth contours. Besides, our images are often corrupted by different kind of noise, which can be due either to the properties of the tissues and of the MRI sequences we are working with, or to magnetic field inhomogeneity, which typically causes low frequency noise.

Local Binary Fitting Energy

Consider a given image $I : \Omega \to \mathbb{R}$, where $\Omega \subset \mathbb{R}^n$ is the image domain. Let C be a contour in the image domain Ω. For each point $\mathbf{x} \in \Omega$ the following energy is defined:

$$\begin{aligned} \mathcal{E}_{\mathbf{x}}^{LBF}(C, f_1(\mathbf{x}), f_2(\mathbf{x})) &= \lambda_1 \int_{in(C)} K(\mathbf{x}-\mathbf{y})|I(\mathbf{y}) - f_1(\mathbf{x})|^2 d\mathbf{y} + \\ &+ \lambda_2 \int_{out(C)} K(\mathbf{x}-\mathbf{y})|I(\mathbf{y}) - f_2(\mathbf{x})|^2 d\mathbf{y} \end{aligned} \tag{4.20}$$

where λ_1 and λ_2 are positive constants, and K is a kernel function with a localization property that $K(\mathbf{u})$ is a positive decreasing function, i.e., it approaches zero as $|\mathbf{u}|$ increases, and $f_1(\mathbf{x})$ and $f_2(\mathbf{x})$ are two numbers that fit image intensities near the point $\mathbf{x}$. The energy defined in 4.20 is called the *local binary fitting (LBF) energy* around the center point $\mathbf{x}$. The values of $f_1(\mathbf{x})$ and $f_2(\mathbf{x})$ are spatially varying, thus overcoming the problems of piecewise constant models. In particular, they only fit the image intensities near each $\mathbf{x}$, because the kernel function has be designed in order to take larger values at the points $\mathbf{y}$ near the point $\mathbf{x}$, while decreasing to 0 as $\mathbf{y}$ goes away from $\mathbf{x}$.

A typical kernel function can be modeled as a Gaussian kernel

$$K_\sigma(\mathbf{x}) = \frac{1}{\sqrt{2\pi}\sigma^n} \exp \frac{-|\mathbf{x}|^2}{2\sigma^2}. \tag{4.21}$$

Variational level set formulation of the model

Transposing the 4.20 in a variational level set formulation, the energy to be minimized becomes

$$\begin{aligned} \mathcal{E}_{\mathbf{x}}^{LBF}(\phi, f_1(\mathbf{x}), f_2(\mathbf{x})) &= \lambda_1 \int K_\sigma(\mathbf{x}-\mathbf{y})|I(\mathbf{y}) - f_1(\mathbf{x})|^2 H(\phi(\mathbf{y}))d\mathbf{y} + \\ &+ \lambda_2 \int K_\sigma(\mathbf{x}-\mathbf{y})|I(\mathbf{y}) - f_2(\mathbf{x})|^2 (1 - H(\phi(\mathbf{y})))d\mathbf{y}. \end{aligned} \tag{4.22}$$

The 4.22 has to be minimized for all the $\mathbf{x}$ in the image domain Ω, thus the fitting energy can be written as

$$\begin{aligned} \mathcal{E}_{\varepsilon}^{LBF}(\phi, f_1, f_2) &= \int_\Omega \mathcal{E}_{\mathbf{x}}^{LBF}(\phi, f_1(\mathbf{x}), f_2(\mathbf{x}))d\mathbf{x} \\ &= \lambda_1 \int\int K_\sigma(\mathbf{x}-\mathbf{y})|I(\mathbf{y}) - f_1(\mathbf{x})|^2 H_\varepsilon(\phi(\mathbf{y}))d\mathbf{y}d\mathbf{x} + \\ &+ \lambda_2 \int\int K_\sigma(\mathbf{x}-\mathbf{y})|I(\mathbf{y}) - f_2(\mathbf{x})|^2 (1 - H_\varepsilon(\phi(\mathbf{y})))d\mathbf{y}d\mathbf{x} \end{aligned} \tag{4.23}$$

where the Heaviside function has been approximated using the 4.18.
In order to make the level set function evolution more stable, additional terms can be introduced. In particular, the deviation of ϕ from a signed distance function can be characterized by the following integral

$$\mathcal{P}(\phi) = \int_\Omega \frac{1}{2}(|\nabla\phi(\mathbf{x})| - 1)^2 d\mathbf{x} \tag{4.24}$$

while a control in the length of ϕ can be obtained by calculating

$$\mathcal{L}_\varepsilon(\phi) = \int_\Omega \delta_\varepsilon(\phi(\mathbf{x}))|\nabla\phi(\mathbf{x})|d\mathbf{x}. \tag{4.25}$$

So, the entire energy functional to be minimized to find the object boundary results in

$$\mathcal{F}_\varepsilon(\phi, f_1, f_2) = \mathcal{E}_\varepsilon^{LBF}(\phi, f_1, f_2) + \mu\mathcal{P}(\phi) + \nu\mathcal{L}_\varepsilon(\phi) \tag{4.26}$$

where μ and ν are nonnegative constants.
To minimize the 4.26, we use the standard gradient descent method. In particular, keeping ϕ fixed, the 4.26 is minimized with respect to $f_1(\mathbf{x})$ and $f_2(\mathbf{x})$,

which results in

$$f_1(\mathbf{x}) = \frac{K_\sigma(\mathbf{x}) * [H_\varepsilon(\phi(\mathbf{x}))I(\mathbf{x})]}{K_\sigma(\mathbf{x}) * H_\varepsilon(\phi(\mathbf{x}))} \tag{4.27}$$

and

$$f_2(\mathbf{x}) = \frac{K_\sigma(\mathbf{x}) * [(1 - H_\varepsilon(\phi(\mathbf{x})))I(\mathbf{x})]}{K_\sigma(\mathbf{x}) * (1 - H_\varepsilon(\phi(\mathbf{x})))}. \tag{4.28}$$

Then, keeping $f_1(\mathbf{x})$ and $f_2(\mathbf{x})$ fixed, the 4.26 is minimized with respect to ϕ, so that the Euclidean evolution equation is derived for ϕ

$$\frac{\partial \phi}{\partial t} = -\delta_\varepsilon(\phi)(\lambda_1 e_1 - \lambda_2 e_2) + \nu \delta_\varepsilon(\phi) div(\frac{\nabla \phi}{|\nabla \phi|}) + \mu(\nabla^2 \phi - div(\frac{\nabla \phi}{|\nabla \phi|})) \tag{4.29}$$

where e_1 and e_2 are

$$e_1(\mathbf{x}) = \int_\Omega K_\sigma(\mathbf{y} - \mathbf{x})|I(\mathbf{x}) - f_1(\mathbf{y})|^2 d\mathbf{y} \tag{4.30}$$

and

$$e_2(\mathbf{x}) = \int_\Omega K_\sigma(\mathbf{y} - \mathbf{x})|I(\mathbf{x}) - f_2(\mathbf{y})|^2 d\mathbf{y}. \tag{4.31}$$

As pointed out by the authors, this method does not require any regularization of the fitting functions f_1 and f_2 or reinitialization of the level set function ϕ: in particular, the initialization itself of ϕ is quite flexible, so that it can be simply initialized as a binary function

$$\phi_0(\mathbf{x}) = \begin{cases} c_0 & \text{for } \mathbf{x} \in R_0 \\ -c_0 & \text{for } \mathbf{x} \in \{\Omega \setminus R_0\} \end{cases}$$

where the region R_0 is an arbitrary subset of the image domain Ω.
Some tricks for a computationally efficient implementation of the method are suggested in [58].

4.3 Level Set Based Brain Segmentation

The proposed LBF method was adapted in this work in order to segment gray matter from MR images acquired from our cohort of MS patients. What has turned out to be the first hurdle is that there is no MRI sequence that provides both a tissue contrast sufficient for a level set evolution and that at the same time has enough resolution to allow a well defined delineation of the tissues' boundaries. In fact if the T_1-w sequence is characterized by a

high spatial resolution, it has the drawback that different tissues are not adequately contrasted. Besides, the morphological changes resulting from the presence of lesions make tissues' appearance even less adequate for a proper tissue classification. On the other hand, DIR sequence provides a definitely better contrast between gray matter and the other tissues, but it is corrupted by a disadvantageous signal to noise ratio, due primarily by the double inversion recovery. In fact, every inversion recovery applied causes a worsening of the SNR of the sequence. The consequences of partial volume effect coupled with the poorer voxel resolution, compared with the T_1-w sequence, do not make DIR sequence the proper choice to obtain an accurate delineation of the borders between GM and CSF, although it can be helpful in the detection of the GM-WM border.
On the other hand, even though FLAIR's SNR is less favourable than T_1-w's, it is acquired applying just one inversion recovery pulse, thus providing a better defined CSF-GM border than DIR's. The disadvantage is a poor contrast between GM and WM, combined with a weak highlighting of MS lesions in GM.
What is new is that we exploit the advantageous peculiarities of the two different MRI sequences, i.e. FLAIR and DIR, combining them to obtain the results. More precisely, we firstly use FLAIR sequence to segment the CSF, thus managing to extract the brain, i.e. gray and white matter. Then the gray matter is segmented on DIR images, starting from the results obtained on FLAIR images. In particular, after a coregistration step, we apply in cascade two different level sets, one for each MRI sequence. The whole process is both described thoroughly in the next sections, and summarized in the flowchart in Fig. 4.10.

4.3.1 Volume coregistration and brain extraction

At first a preprocessing step is required to coregister the two sequences we are working with. FLAIR and DIR images are coregistered using the *Coregister, Estimate and Reslice* tool in SPM8 [2]. The setting of the Estimation Options and of the Reslice Options is described in Appendix A. An example of the result of the coregistration is shown in Fig. 4.11.

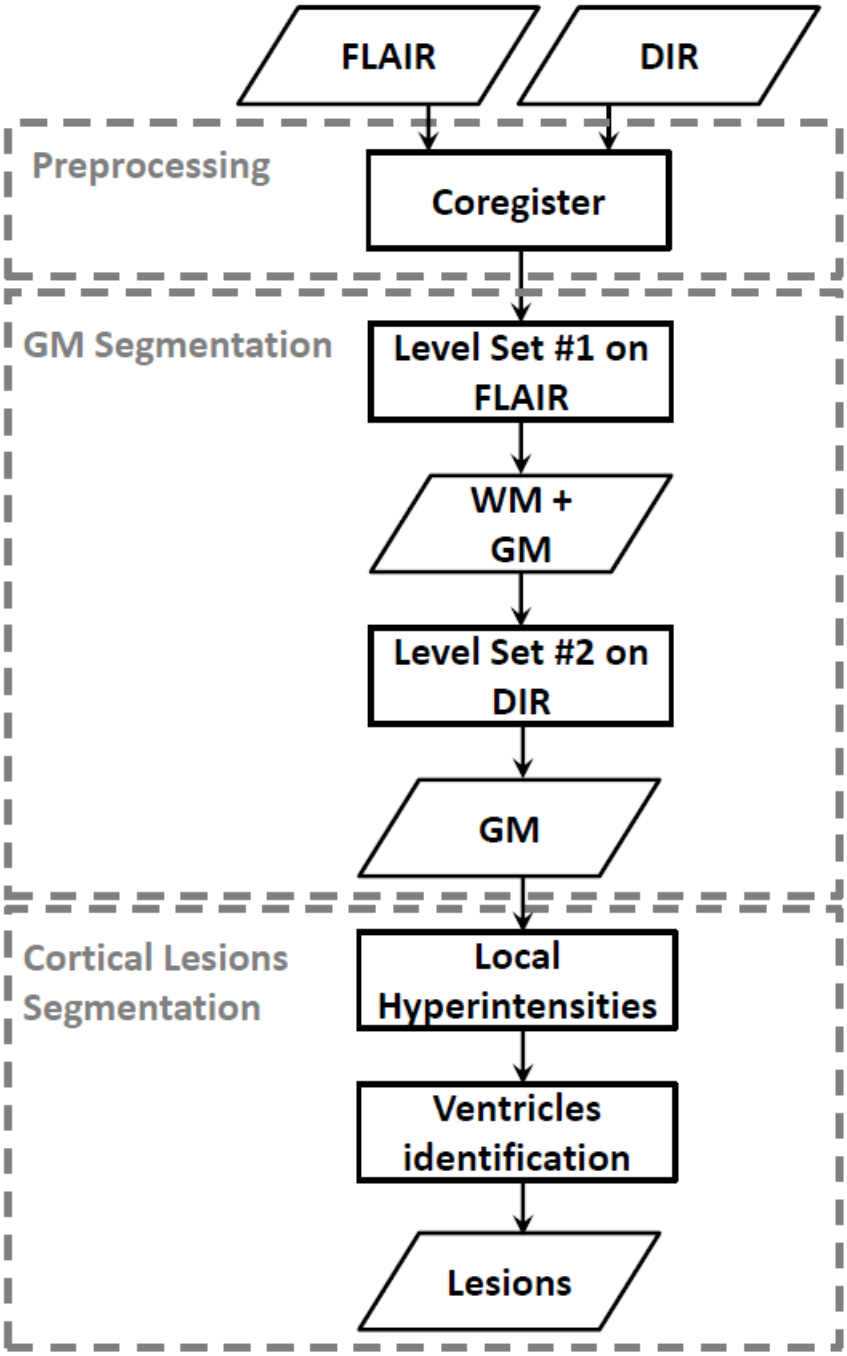

Figure (4.10). *Overall lesion detection process flow, starting with the input DIR and FLAIR images. In this chapter the Preprocessing and GM Segmentation steps are described. The Cortical Lesions Segmentation step will be discussed in Chap. 5.*

(a) DIR **(b)** FLAIR

Figure (4.11). *Sample slice of a DIR volume (left panel), with its corresponding slice taken from the FLAIR volume (right panel).*

4.3.2 Descalping

Then on FLAIR images a rough brain extraction is obtained. To perform this step, we exploit the fact that in FLAIR sequence, considering axial slices, the brain appears as a bright structure well disconnected from the surrounding skull. This is due to the suppression of the CSF, which is the main characteristic of FLAIR sequence. So, using an edge detector based on the Laplacian of Gaussian operator, followed by simple morphological operators, we eliminate the outer connected component, represented by the bone.

4.3.3 Gray and White Matter Segmentation on FLAIR

In the obtained FLAIR image deprived of the skull, we apply the first level set. Being that the contribution of the CSF is nullified by the particular MRI sequence, we expect the level set to segment gray and white matter from the surrounding darker tissues. In particular, the parameters were set as follows: $\lambda_1 = \lambda_2 = 1$, $\nu = 0.004 \times 255^2$, $\mu = 1$, $\varepsilon = 5$, $\sigma = 2$. The gray levels of each image were scaled in the range $[0\ 255]$. The level set was initialized as a binary function

$$\phi_{0\_Fla}(\mathbf{x}) = \begin{cases} 2 & \text{for } \{\mathbf{x} \in I(\mathbf{x}) | I(\mathbf{x}) > 2\overline{\mu}\} \\ -2 & \text{for } \{\mathbf{x} \in I(\mathbf{x}) | I(\mathbf{x}) < 2\overline{\mu}\} \end{cases}$$

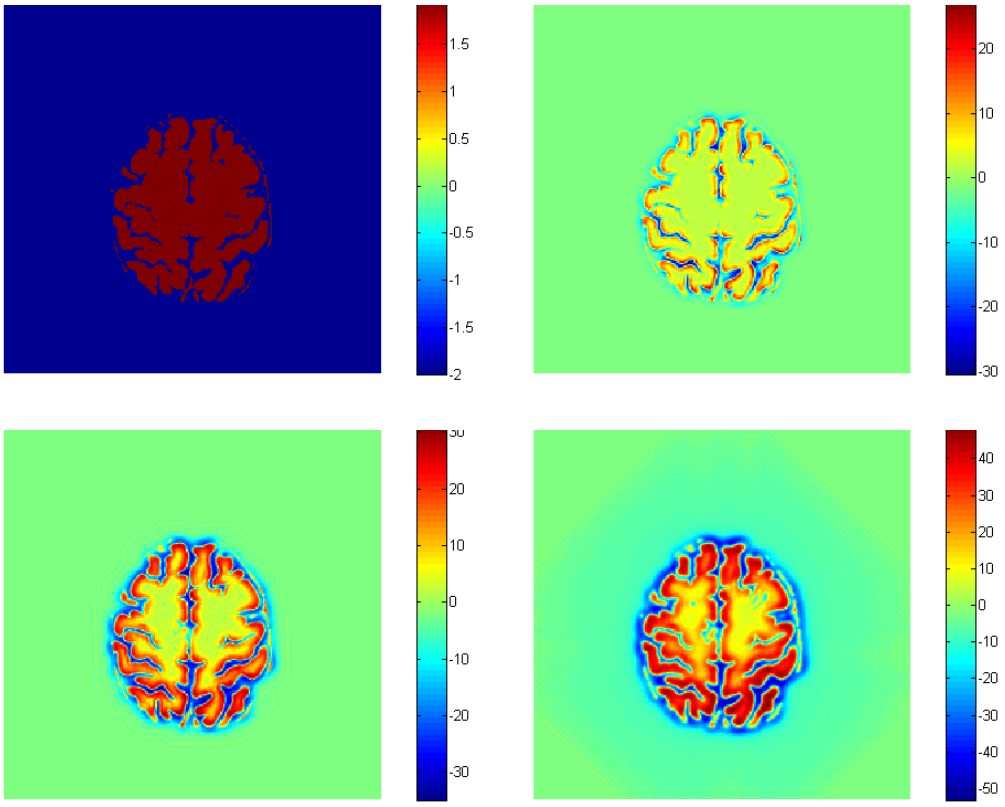

Figure (4.12). *Initialization and evolution of the first level set: initialization as a constant function; evolution after one iteration; evolution after four iterations; final configuration.*

where I is the FLAIR image to be segmented and $\overline{\mu}$ is the mean gray level evaluated in I. Initialization and evolution of ϕ_{Fla} are represented in Fig. 4.12. The zero crossing of ϕ_{Fla} correspond to the border between the white matter and the CSF, which can be better appreciate in Fig. 4.13, where ϕ_0 is superimposed to the original FLAIR image.
The curve is made evolve (Fig. 4.13) and Eq. 4.32 is minimized so that the Euclidean evolution equation is derived for ϕ_{Fla}.

$$\mathcal{F}_{\varepsilon}(\phi_{Fla}, f_1, f_2) = \mathcal{E}_{\varepsilon}^{LBF}(\phi_{Fla}, f_1, f_2) + \mu\mathcal{P}(\phi_{Fla}) + \nu\mathcal{L}_{\varepsilon}(\phi_{Fla}). \tag{4.32}$$

The resulting segmentation provides the contour of the gray and white matter, and is subsequently applied to the corresponding DIR image (Fig. 4.14).

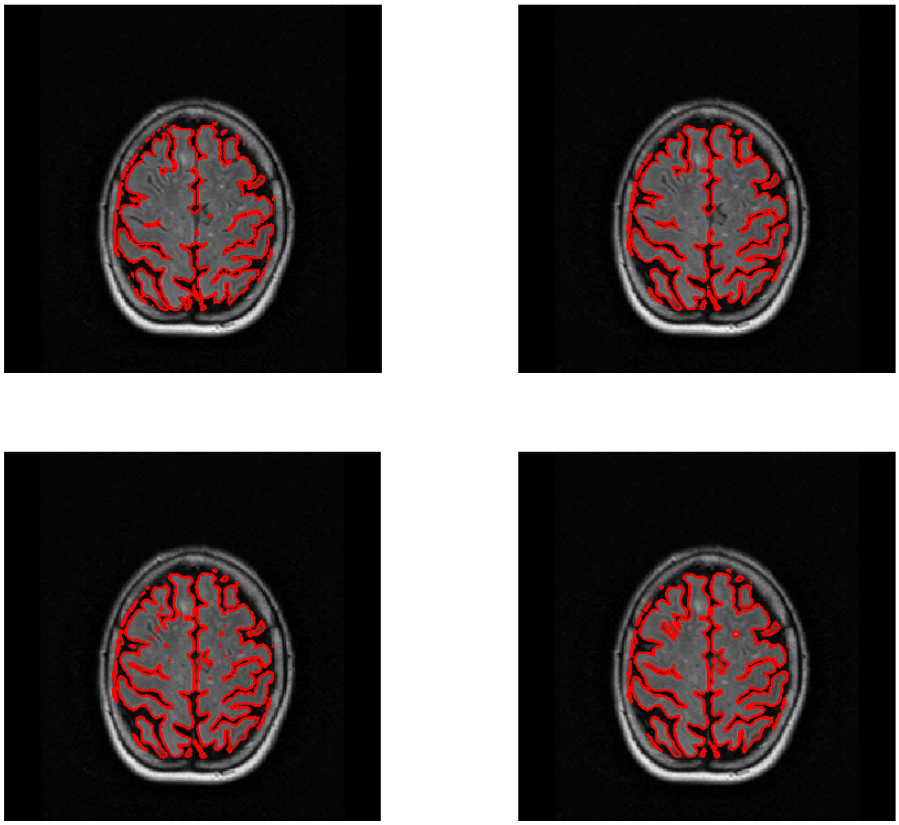

Figure (4.13). *Zero level set, initialization and evolution of the first level set superimposed to the corresponding FLAIR image: initialization; evolution after one iteration; evolution after four iterations; final configuration.*

4.3.4 Gray Matter Segmentation in DIR

In the resulting DIR image, which now carries the contributions only of gray and white matter, we apply the second level set. Being that this specific sequence is characterized by the capability of contrasting these two tissues, we expect the level set to segment gray matter from white matter.
In particular, the parameters were set as follows: $\lambda_1 = \lambda_2 = 1$, $\nu = 0.0001 \times 255^2$, $\mu = 1$, $\varepsilon = 5$, $\sigma = 2$. Note that in this case we used a smaller value of ν, in order to let the emergence of new contours, consistently with the convolved anatomy of gray matter.
The gray levels of each image were scaled in the range $[0\ 255]$. The level set

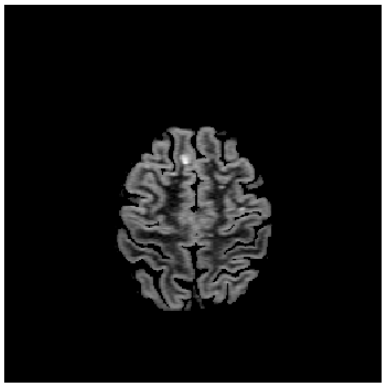

Figure (4.14). *Result of the application of the mask obtained with the first level set on the corresponding DIR image*

was initialized as a binary function

$$\phi_{0\_Dir}(\mathbf{x}) = \begin{cases} 2 & \text{for } \{\mathbf{x} \in I(\mathbf{x}) | I(\mathbf{x}) > \vartheta\} \\ -2 & \text{for } \{\mathbf{x} \in I(\mathbf{x}) | I(\mathbf{x}) < \vartheta\} \end{cases}$$

where I is a nonnegative image obtained by calculating the Euclidean distance transform from each point of the final zero level set obtained from Eq. 4.32. The distance transform assigns to the corresponding pixel in I a number that is the distance between that pixel and the nearest point of the zero level set. The value of the threshold ϑ was set to 5.
Initialization and evolution of ϕ_{Dir} are represented in Fig. 4.15. The curve is made evolve (Fig. 4.16) and Eq. 4.33 is minimized so that the Euclidean evolution equation is derived for ϕ_{Dir}.

$$\mathcal{F}_\varepsilon(\phi_{Dir}, f_1, f_2) = \mathcal{E}_\varepsilon^{LBF}(\phi_{Dir}, f_1, f_2) + \mu\mathcal{P}(\phi_{Dir}) + \nu\mathcal{L}_\varepsilon(\phi_{Dir}). \tag{4.33}$$

The resulting segmentation provides the contour of the gray matter. Fig. 4.17 shows another example of the obtained GM segmentation superimposed to the corresponding DIR slice. This is the same slice already proposed in Section 4.1.4 (Fig. 4.2), on which we elucidated some common problems arising when segmenting brain tissues with popular brain imaging software. From our result it can be seen that the cortical lesion is still classified as GM, which is essential in order to subsequently highlight GM abnormalities.

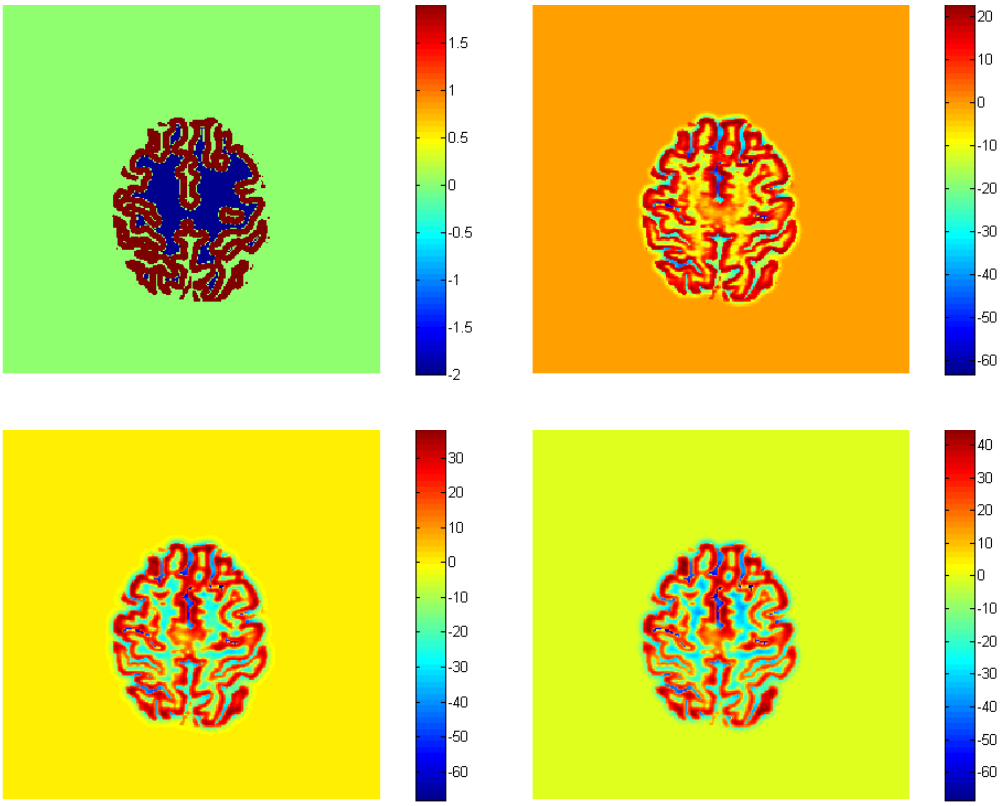

Figure (4.15). *Initialization and evolution of the second level set: initialization as a constant function; evolution after five iterations; evolution after ten iterations; final configuration.*

4.3.5 Ventricles identification

The ventricular system is a set of structures containing cerebrospinal fluid in the brain. The system comprises four ventricles: right and left lateral ventricles, third ventricle, and fourth ventricle. The ventricles are filled with CSF, which bathes and cushions the brain and spinal cord within their bony confines.

MS plaques are commonly found within this region surrounding the four ventricles. Periventricular lesions produce atrophy of the corpus callosum, as evidenced by MRI.

As we have already said, the proposed level set GM segmentation prescinds from any anatomical information. So in our work periventricular lesions rep-

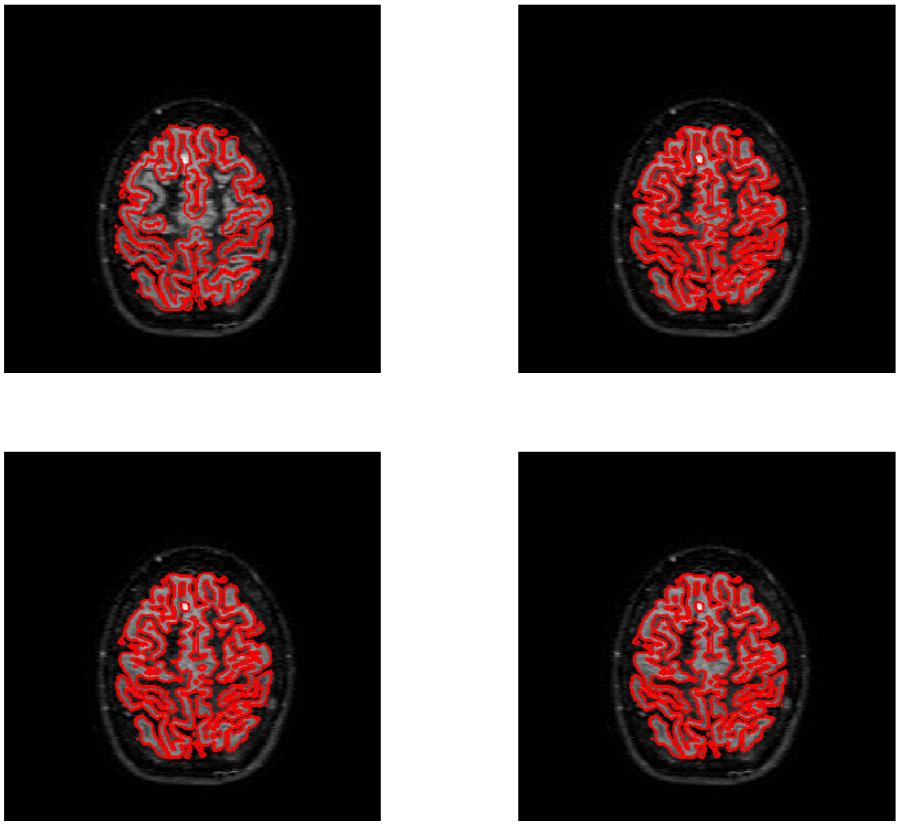

Figure (4.16). *Zero level set, initialization and evolution of the second level set superimposed to the corresponding DIR image: initialization; evolution after five iterations; evolution after ten iterations; final configuration.*

resent a problem because, since in DIR they usually appear as hyperintense regions, they can be erroneously segmented as GM.
In order to overcome this inconvenience, we again exploit the characteristics of FLAIR images: since in this sequence the CSF is nullified and appears as a dark region in contrast to WM and GM, which are brighter, we find ventricles by looking for the presence of a dark region roughly in the middle of the axial slice. In FLAIR images, the ventricles appear as big, closed regions with a smooth profile.
We then obtain a mask of the ventricles in FLAIR. Such a mask can be subsequently used in order to discard those potential hyperintense regions visible in DIR images adjacent to ventricles.

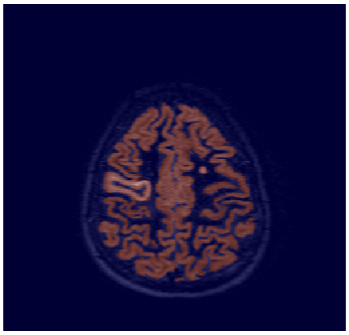

Figure (4.17). *Result of our level set based GM segmentation.*

4.4 Further Improvements

To further improve the brain segmentation results achievable with our level set based segmentation algorithm, we are trying to couple information related to texture analysis. In particular, a supervised classification of brain tissues using local multi-scale texture analysis in FLAIR and in DIR MR sequences has recently been tested ([74]). The aim of this work is to implement a supervised classification method that exploits the texture information of the brain tissue provided by the two sequences FLAIR and DIR (Fig. 4.18). Fig. 4.19 shows the manual segmentation performed by one of the two expert neurologists, together with the segmentation obtained by our algorithm.

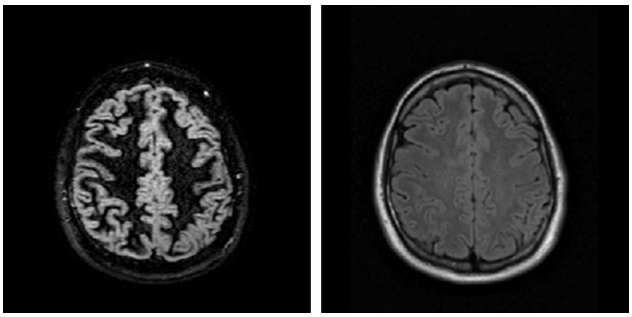

Figure (4.18). *Two corresponding slices extracted from a DIR (left panel) and a FLAIR (right panel) volume.*

Vovk et al. ([101]) succeeded in automatically generate accurate class priors that can be used to initialize and regularize image segmentation without

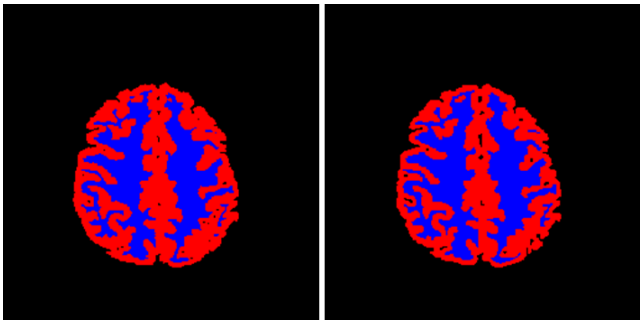

Figure (4.19). *One of the two manual ground truth segmentation provided by the experts (left panel) and the result provided by our algorithm when the image was in the testing set (right panel).*

using bias field correction, location-based templates, or registration. Information about a voxel's tissue class membership is based on its signature - a collection 3 local volume textures estimated over a range of 10 neighborhood sizes on T_1-weighted sequences. In order to reduce the heterogeneity of signatures within a tissue type, 9 different subclasses have been classified with a supervised approach, and eventually merged with a voting scheme into the 3 classes GM, WM, and CSF. Although that approach's results out-perform those provided by location based method, both qualitatively and quantitatively, they are quite poor: Dice similarity coefficient for GM, WM, and CSF are respectively 0.90, 0.85 and 0.55. In our work we avoid using T_1-w sequence which, even if characterized by high spatial resolution, proved inadequate for tissue segmentation when brain lesions are present. In addition, the method does not need population-derived location-based priors, registration to template space, or explicit bias field modeling.

The rationale of our approach is to use the peculiar texture characteristic of a pixel neighborhood in order to obtain information about the pixel tissue class. Image texture analysis has been subject of intense study and has been employed in a variety of applications; however, there is no general agreement upon definition of texture ([97]). For our specific application, we assume that a region in an image has a constant texture if a set of local statistics or other local properties of the picture function are almost constant or approximately periodic ([87]).

4.4.1 Textures employed

Depending on the number of pixels defining the local feature, the statistical methods can be respectively classified as 1^{st} order, 2^{nd} order and higher-order statistics. 1^{st} order statistics measure the likelihood of observing a specific gray value at a random location in the image (hence directly computable from the image histogram). 2^{nd} order statistics measure the likelihood of observing a specific pair of gray values in a randomly placed dipole of pixels (computable from the gray level co-occurrence matrices (GLCM) ([40])). Method proposed in ([101]) employed three 1^{st} order statistics: skewness-, median-, and median absolute deviation-based textures, which, on T_1-w images, are approximately independent of bias field and of scanner gain. In order to increase the discriminability of the classes, and at the same time couple at best with the double source of information at disposal (i.e., the DIR and the FLAIR sequences), we opted to employ as features four 1^{st} order statistics and five 2^{nd} order statistics. The 1st-order statistics considered in this work are mean, standard deviation, skewness, and kurtosis, while the 2^{nd} order ones are contrast, correlation, homogeneity, entropy and energy.

In Eq. 4.34-4.37 we report the mathematical formulations of the 1^{st} order statistics employed in this work: one ordinary moment and three central moments (two of which are standardized). We chose this set of values because it can accurately characterize a probability distribution in all its properties: while the 1^{st} moment, expected value or mean, describes the central location of the data, central moments relate only to the spread and shape of the distribution. The standard deviation, i.e., the square of the 2^{nd} central moment, measures the dispersion of the data from the average. The skewness and the kurtosis measure respectively the asymmetry and the peakedness (or the heaviness of the tails) of the distribution. These two last statistics are based on the standardization (with respect to the standard deviation) of the 3^{rd} and the 4^{th} central moment, and hence are scale invariant and dimensionless.

$$\mu = E[I] = \frac{1}{N^2} \sum_{x,y} I(x,y) \tag{4.34}$$

$$\sigma = \sqrt{E[(I-\mu)^2]} = \sqrt{\frac{1}{N^2}\sum_{x,y}(I(x,y)-\mu)^2} \tag{4.35}$$

$$\gamma_1 = E[(\frac{I-\mu}{\sigma})^3] = \frac{\frac{1}{N^2}\sum_{x,y}(I(x,y)-\mu)^3}{\sigma^3} \tag{4.36}$$

$$\gamma_2 = E[(\frac{I-\mu}{\sigma})^4] - 3 = \frac{\frac{1}{N^2}\sum_{x,y}(I(x,y)-\mu)^4}{\sigma^4} - 3 \tag{4.37}$$

In order to compute the 2^{nd} order statistics, GLCM has to be defined. If G is the number of gray levels of the image $I(x,y)$, the GLCM $C_{\mathbf{d}}$ for a displacement vector $\mathbf{d} = (dx, dy)$ is a square matrix $G \times G$ so that the entry $C_{\mathbf{d}}(i,j)$ is the number of occurrences in I of the pair of gray levels i and j that are a distance $\mathbf{d}$ apart, i.e.:

$$C_{\mathbf{d}}(i,j) = \sum_{x,y} \begin{cases} 1 & \text{if } I(x,y) = i, I(x+dx, y+dy) = j \\ 0 & \text{otherwise} \end{cases}$$

2^{nd} order statistics (Eq. 4.38 - 4.42) can be thought as weighted sums of the GLCM cell contents, where the weights express the relative importance of the cell values. In that sense, it is worth noting that the diagonal elements of C represent all pixel pairs with no grey level difference; the farther away from the diagonal, the greater the difference between pixel grey levels. The contrast (i.e., the sum of squares variance) exponentially weights C as $|i-j|$ increases, while in the homogeneity definition the weights decrease exponentially away from the diagonal. Entropy and energy are measures related to orderliness (regularity or commonness) of the data: the weights are constructed related to how many times a given pair occurs. Since $C(i,j)$ are already a measure of commonness of occurrence, it makes that they are used as weights for themselves.

$$\text{Contrast} = \sum_{i,j} C(i,j)(i-j)^2 \tag{4.38}$$

$$\text{Homogeneity} = \sum_{i,j} C(i,j)\frac{1}{1+|i-j|} \tag{4.39}$$

$$\text{Entropy} = -\sum_{i,j} C(i,j) ln C(i,j) \tag{4.40}$$

$$\text{Energy} = \sum_{i,j} C(i,j)^2 \tag{4.41}$$

$$\text{Correlation} = \sum_{i,j} C(i,j) \frac{(i-\mu_{cx})(j-\mu_{cy})}{\sigma_{cx}\sigma_{cy}} \tag{4.42}$$

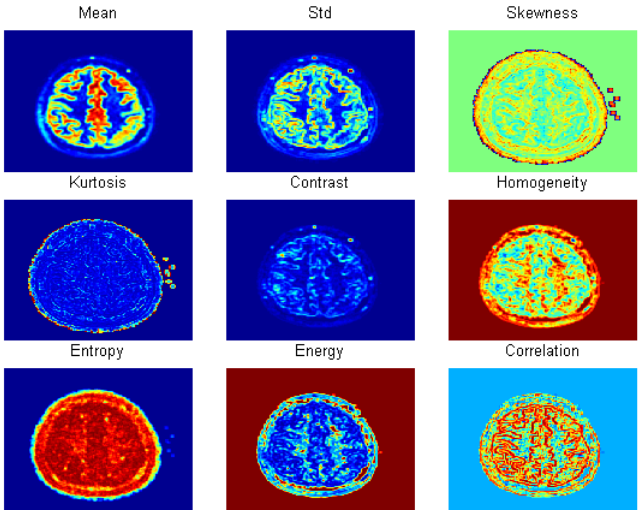

Figure (4.20). *The nine textures extracted from a DIR slice at scale 5 (i.e.* 5×5 *pixel block analysis). The corresponding original DIR slice is visible in Fig. 4.18, left panel.*

4.4.2 Feature Extraction and Classifier Setup

The local texture information were extracted at 3 different scales from blocks of $N \times N$ pixel, with $N = 3, 5, 7$ (Fig. 4.20 and Fig. 4.21 show the case with N = 5).

For each 2^{nd} order texture, four GLCMs are constructed, with $d = (dx, dy) \in \{(0,1), (1,1), (1,0), (1,-1)\}$. Then, to make the textures invariant to rotation, the obtained matrices are averaged over the 4 angles. Since the feature extraction is performed on both DIR and FLAIR images, the final feature vector associated to each pixel is composed by 56 values, including 2 original sequence pixel values.

For the setup of the classifier, we employed as a classifier model the libSVM library ([15]) interfaced with MATLAB. Training on the 56-feature element

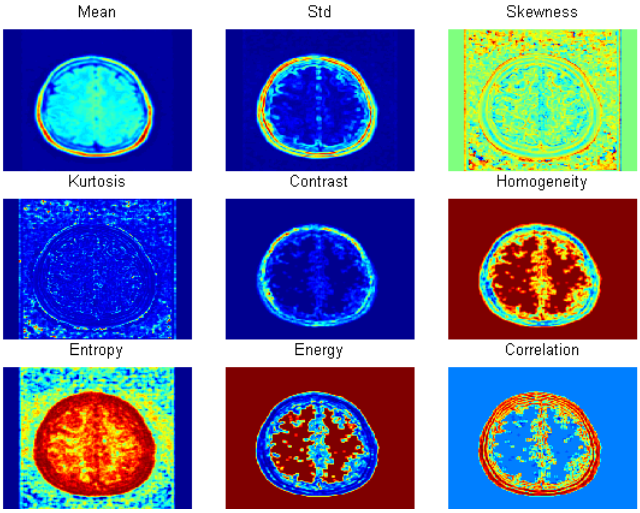

Figure (4.21). *The nine textures extracted from a FLAIR slice at scale 5 (i.e.* 5×5 *pixel block analysis). The corresponding original FLAIR slice is visible in Fig. 4.18, right panel.*

set was carried out with a Radial Basis Function kernel. In order to find the optimal parameters of the SVM model (gamma and penalty parameter c) we performed a grid search on an exponential grid, with both gamma and c ranging from 2^{-6} to 2^{6}. The parameter pair providing the best classification in a 10-fold cross-validation was chosen.

4.4.3 Results

In the first three rows of Table 4.3 we reported the above-mentioned performance indexes computed for the second human observer versus the first one. In the last three rows we reported the performance indexes of our algorithm, whose results are compared with the first human observation. In this last case, the value reported for each index is the mean value computed on the 4 results of the 4-fold cross-validation. The standard deviation is not reported, since in each fold, and for each index, it was always less than 0.0020. Comparison with the results of other study is always a delicate matter when different dataset is used. The rationale of the approach described in [101] is similar to ours, since a supervised classification on textures-based features is proposed. That system consists in extracting three 1^{st} order textures from a spherical neighborhood at 10 scales (1, 2, 3, 4, 6, 8, 10, 13, 16, and 19 mm) from a T1-w

volume, in order to classify 9 tissue subclasses. The scheme we propose, instead, consists in extracting 4 1^{st} order textures and 5 2^{nd} order textures from a squared neighborhood at 3 scales (3, 5, 7 pixels) from each of the DIR and FLAIR sequences, in order to classify 3 tissue classes. Quantitative results in [101] can be appreciated only in graphs and figures, where average Dice similarity coefficients for GM, WM, and CSF are respectively around 0.90, 0.85 and 0.55.

Table (4.3). *Brain segmentation metrics computed for FSL and FreeSurfer on the LONI Segmentation Validation Engine*

	Class	Accuracy	Sensitivity	Specificity	Dice	Matthews
Ref2 vs Ref1	BG	0.995	0.994	0.997	0.996	0.984
	WM	0.990	0.934	0.996	0.953	0.948
	GM	0.986	0.973	0.988	0.943	0.936
Our method vs Ref1	BG	0.991	0.993	0.984	0.994	0.975
	WM	0.988	0.930	0.998	0.957	0.951
	GM	0.985	0.969	0.986	0.926	0.919

Chapter 5

Gray Matter Lesion Identification

As it has been introduced in Section 2.7.1, cortical lesions detection is usually manually performed. This is not a banal problem, which requires lot of time and experience. Still, an open issue when manually scoring images is represented by factors such as lesion type, size, and location, as well as field strength, image quality measures, and sequence type. This evidence arises the need of a more adequate technique to standardize cortical lesions detection.

5.1 Methods

Even if MS cortical lesions appear as hyperintense regions in DIR images, a simple thresholding on the GM intensities fails in correctly identifying and delineating lesions boundaries because of low signal to noise ratio, intensity inhomogeneity and appearance variability of the lesions.

5.1.1 Bias Field

A common problem met when working with MR images is represented by two distant voxels having the same biological composition but indifferent gray level intensity. This difference in intensity is called bias, and it can be caused by field inhomogeneities, by imperfections of the RF coil ([67]) or by the fact

that the same biological structure is characterized by an intensity that varies around a mean value ([76]). The presence of bias results in a smooth, biologically meaningless variation of the tissue intensities across MR images, which can amount to as much as 30% of the signal amplitudes. Though this bias field produces little effect on visual interpretation, it can significantly affect the outputs of image processing tools. Many methods have been proposed so far to correct this kind of noise; they can be broadly divided into two categories: *prospective methods* ([95]) and *retrospective methods* ([59], [76]). Prospective methods operate in the acquisition phase, modifying the hardware or adopting specific sequences. In such a way they can correct the inhomogeneity due to the RF coil, but they cannot do anything to avoid the intensity inhomogeneities that are patient-dependant. Retrospective methods, instead, act in the post-processing phase, and thus can remove patient-dependant effects.
In our specific problem, assuming a gray matter (statistical) homogeneity, we can safely conclude that the observed intensity variability can have only two sources: bias field inhomogeneity or presence of lesions. Lesions are localized and thus correspond to high spatial frequencies, whereas the bias field is slowly varying across each slice. Hence, instead of trying to estimate the bias field and then correcting the tissue intensities, we can mitigate the problem by estimating the local gray matter mean and standard deviation, and identifying the region deviating from the gray matter intensity distribution. This local estimation is obtained in a $N \times M$ region around each pixel, and considering GM voxels only: within these neighborhoods, the effects of the bias field can be considered negligible. The optimal dimension of these regions is a trade-off: on one hand we desire as small regions as possible, in order not to be influenced by the smoothly varying field inhomogeneity, whereas on the other hand each region has to be wide enough to ensure both an appropriate number of gray matter voxels and also that the possible presence of lesion does not influence significantly the statistical analysis.
At the implementation stage, it turned out that good results can be obtained by setting $N = 128$ and $M = 128$, i.e. by dividing each axial 256×256 image into four squared subimages, in which the bias field inhomogeneity effects result negligible (Fig. 5.1a).

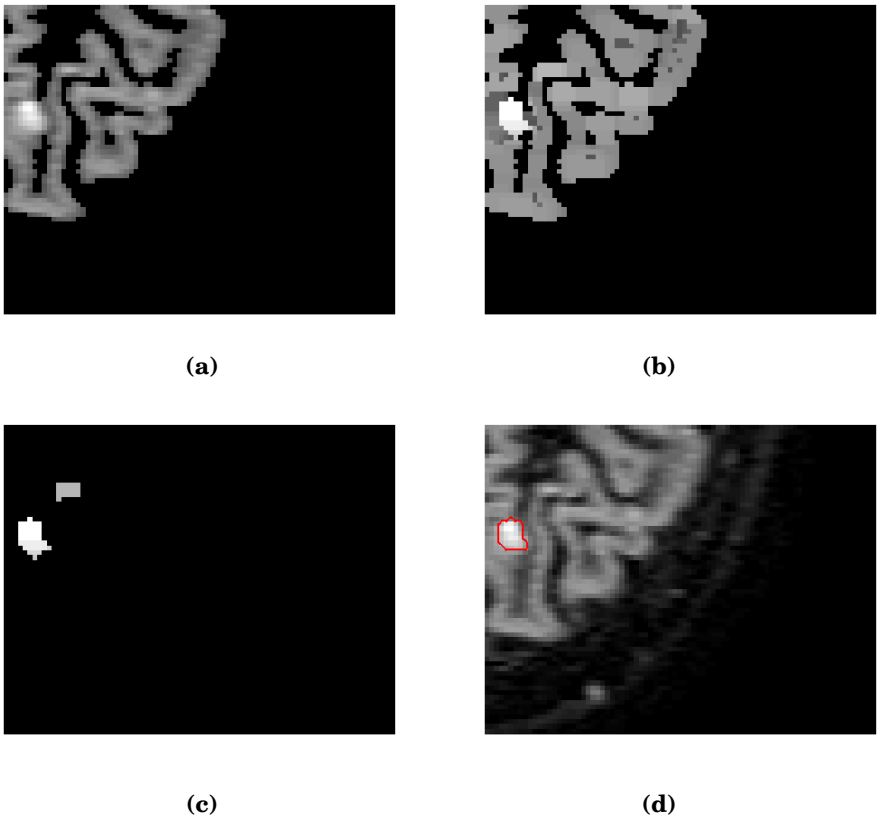

(a) **(b)**

(c) **(d)**

Figure (5.1). *Contrast enhancement and lesions segmentation.*

5.1.2 Data Preprocessing: Contrast Enhancement

As mentioned in 5.1, even if MS cortical lesions appear as hyperintense regions in DIR images, a simple thresholding on the GM intensities fails in correctly identifying and delineating lesions boundaries, becaused of the listed problems. Working in a 128×128 subimage highly attenuate the issue of field inhomogeneity.

In order to enhance the contrast of the DIR sequence and to smooth the noise, we apply the algorithm proposed in [90]. In their work, Souplet et al. try to automatically detect WM lesions in FLAIR sequence by using a threshold: in fact, they claim that most of the lesions have at least a voxel with an intensity higher than the threshold they calculate. However they also had the problem of inhomogeneous lesion voxel intensities that make the delineation of the

lesion difficult. For this reason, they propose a simple algorithm to enhance the contrast in the T_2-FLAIR sequence before applying the threshold.
Our problem is quite similar, so we have tried to adapt the enhancing algorithm to our data. In particular, we have to smooth the noise in DIR images, looking for hyperintense regions in the GM. So, given the k^{th} axial slice in the DIR volume, after the application of the segmentation algorithm described in the previous chapter, we are left with the GM alone (cfr Sec.4.3.4). Then, in order to minimize the effect of the field inhomogeneities, we divide the image in four equal-size subimages. In each of the four subimages S_k^i, with $i = 1, 2, 3, 4$, the local minimum and local maximum of the image are computed by means of morphological operators: in particular, the gray-level erosion E_k^i and dilation D_k^i are calculated; for each pixel at the position (x, y), the resulting filtered image $F_k^i(x, y)$ is obtained by assigning the value in the eroded or dilated version according to the distance $S_k^i(x, y)$ form $D_k^i(x, y)$ and $E_k^i(x, y)$:

$$F_k^i = \underset{\{D_k, E_k\}}{\operatorname{argmin}} \left(|S_k^i - D_k^i|, |S_k^i - E_k^i| \right). \tag{5.1}$$

We used as structuring element for the dilation and the erosion a disk of radius $R = 3$ voxels. An example of the result is shown in Fig. 5.1b.

5.1.3 Candidate Lesions Segmentation

Given the enhanced subimage F_k^i, the mean and standard deviation of the gray matter are estimated. The resulting values are used to threshold the F_k^i in order to get a set of regions representing candidate lesions. In particular, from $F_{GM}^i = \{F_k^i | (x, y) \in GM\}$, we compute $\mu_{GM}^i = E[F_{GM}^i]$ and $\sigma_{GM}^{2i} = var[F_{GM}^i]$, and $\theta_k^i = \mu_{GM}^i + \sigma_{GM}^i$. Then candidate lesions are obtained with

$$L_{Cand} = \begin{cases} 1 & \text{if } F_k^i > \theta_k^i \\ 0 & \text{otherwise} \end{cases}$$

The result consists in an image of disconnected hyperintense regions, which are considered as the starting point from which cortical lesions are extracted. In fact, the thresholding operation provides different regions $L_{cand,j}$, with $j = 1, ..., J$, each one representing a candidate lesion (Fig. 5.1c). From the

consensus recommendation described in Sec.2.7.1, we know that lesions must be hyperintense with respect to their neighborhood and, in order to avoid noise, covering a region bigger than three voxel (considering an in-plane resolution of 1 mm^2). The latter condition can be easily fulfilled by using simple morphological operators.

On the other hand, as far as the required hyperintensity is concerned, for each identified lesion $L_{cand,j}$ a set of parameters are extracted: first of all the external surrounding of $L_{cand,j}$ is obtained with a dilation of $L_{cand,j}$ with a disk-shape structuring element of radius 1, paying attention not to include in the external neighborhood voxels that might belong to other candidate lesions. Then the mean $\mu_{j,int}$, the maximum value $M_{j,int}$ and standard deviation $\sigma_{j,int}$ of the gray level intensities of the voxels belonging to $L_{cand,j}$, together with the mean $\mu_{j,ext}$ and standard deviation $\sigma_{j,ext}$ on the intensities of the cortical voxels belonging to its contour are evaluated. As for the maximum $M_{j,int}$, it is calculated as $M_{j,int} = \frac{1}{4}\sum_{i=1}^{4}(x_i)$, where $x_i,\ i = 1,2,3,4$ are the four brightest voxels belonging to the candidate lesion; in this way we make the parameter more robust to noise.

Finally, in order to comply to the requirements of the consensus recommendations, a proper mathematical representation has been obtained coupling two different conditions:

$$\mu_{j,int} - \sigma_{j,int} \geq \mu_{j,ext} \tag{5.2}$$

and

$$M_{j,int} > \mu_{GM} + l\sigma_{GM} \tag{5.3}$$

where μ_{GM} and σ_{GM} are respectively the mean and the standard deviation of the whole gray matter in F_k^i. In particular, Eq. (5.2) ensures that the interior of the region is well contrasted with respect to its external part. In addition, Eq. (5.3) verifies that each lesion is significantly brighter with respect to the mean gray level intensities of the whole gray matter in F_k^i. The positive parameter l in Eq. (5.3) is used to find a solution to the problem of hyperintense noisy regions in areas such as the insula and in the correspondence of the main cerebral vessels (i.e. superior sagittal sinus). How the value of l is estimated will be explained in section 5.1.4.

The final result of the lesion segmentation is shown in Fig. 5.1d.

5.1.4 Artifacts Prone Areas

As it has been observed by Geurts et al. ([34]), DIR sequence is artefact prone, especially in the insula and in those area adjacent to main vessels (Fig. 2.4): the blood that flows in the vessels generates a hyperintense signal that makes the corresponding regions brighter than the surrounding tissues, causing an uncorrect cortical lesion identification.
In our automatic technique to detect lesions, this fact causes an increased number of false positive, i.e. noisy regions of NAGM that are erroneously classified as cortical lesions.

To overcome the problem, each candidate lesion has been weighted differ-

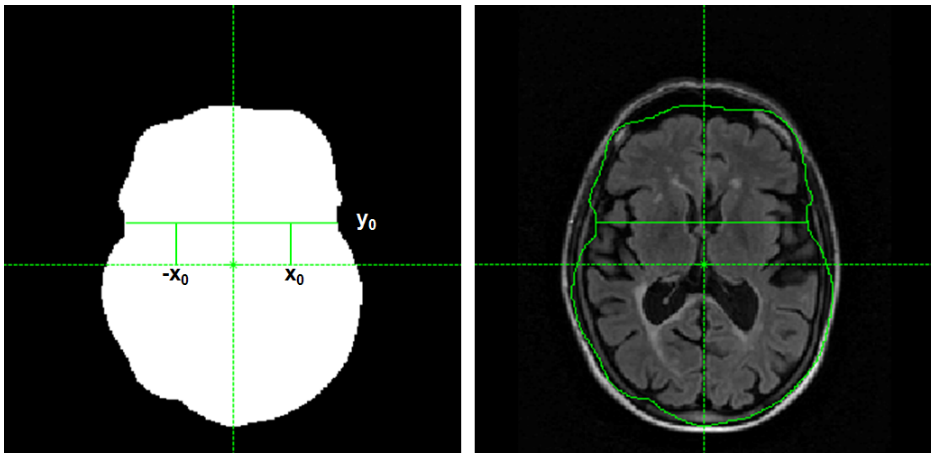

Figure (5.2). *Estimate of the positioning of the weighting kernel functions: the value of y_0 corresponds to the 30% of the distance between the origin and the upper limit of the white mask. The value of x_0 is set in the corresponds of the middle of the horizontal green solid line.*

ently, in order to be more restrictive when judging candidate lesions belonging to areas that are notoriously affected by artifacts. To this aim, different weighting functions have been designed as follows.
Given that when we are analyzing the slices of the MRI volume in correspondence of the insula we want to be more restrictive in a region that is symmetric with respect to the longitudinal cerebral fissure, the weighting function

$wf_1(x,y)$ is designed as

$$\begin{aligned} wf_1(x,y) &= \frac{1}{2\pi\sigma_{1x}\sigma_{1y}}\exp(-(\frac{x^2}{\sigma_{1x}^2})-(\frac{y^2}{\sigma_{1y}^2})) \\ &+ \frac{1}{2\pi\sigma_{2x}\sigma_{2y}}\exp(-(\frac{(x-x_0)^2}{\sigma_{2x}^2})-(\frac{(y-y_0)^2}{\sigma_{2y}^2})) \\ &+ \frac{1}{2\pi\sigma_{2x}\sigma_{2y}}\exp(-(\frac{(x+x_0)^2}{\sigma_{2x}^2})-(\frac{(y-y_0)^2}{\sigma_{2y}^2})). \end{aligned} \tag{5.4}$$

Here σ_{1x} and σ_{1y} represent the variances of a bivariate gaussian function built in the correspondence of the longitudinal cerebral fissure, while σ_{2x} and σ_{2y} are the variances of two bivariate gaussian functions located in the correspondence of the right and left insula. The values of x_0 and y_0 have been set in order to properly locate the two symmetric gaussian functions. In particular, the coordinate system has been translated so that its origin coincide with the estimated centroid of the region provided by the first level set. The $y-$axis therefore is in the middle of the longitudinal cerebral fissure, thus roughly dividing the two hemispheres on each axial slice. To position the two gaussian surfaces in the correspondence of the two insulae, we have set y_0 and x_0 so that the two kernels result symmetric with respect to the $y-$axis (Fig. 5.2). The resulting surface is represented in Fig. 5.3, while in Fig. 5.6a we have superimposed the value of 5.4 to its corresponding DIR axial slice.

Similarly, when we are analyzing the slices of the MRI volume in correspondence of the main brain vessel (i.e. superior sagittal sinus), we want to be more restrictive in a region that covers the longitudinal cerebral fissure. In this case the used weighting function $wf_2(x,y)$ is

$$wf_2(x,y) = \frac{1}{2\pi\sigma_x\sigma_y}\exp(-(\frac{x^2}{\sigma_x^2})-(\frac{y^2}{\sigma_y^2})) \tag{5.5}$$

where σ_x and σ_y represent the variances of a bivariate gaussian function built in the correspondence of the longitudinal cerebral fissure. The resulting surface is represented in Fig. 5.4, while in Fig. 5.6b we have superimposed the value of Eq. 5.4 to its corresponding DIR axial slice.
The value of l in Eq. 5.3 is obtained by calculating the mean of the gaussian weighting function in the pixels of the DIR image covered by the candidate

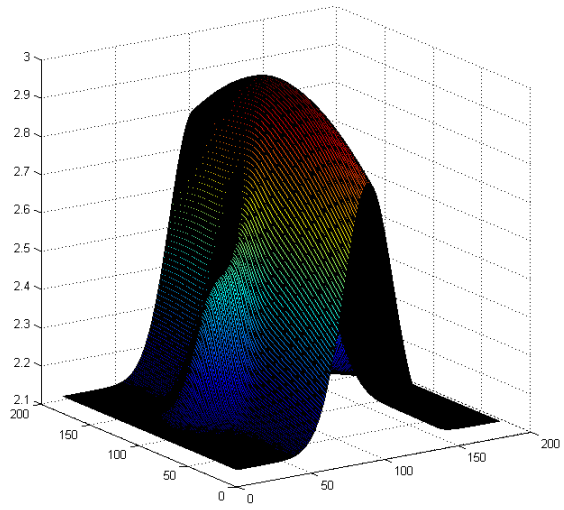

Figure (5.3). *Three dimensional rendering of the weighting function in Eq. 5.4 used to score lesions in Fig. 5.6a.*

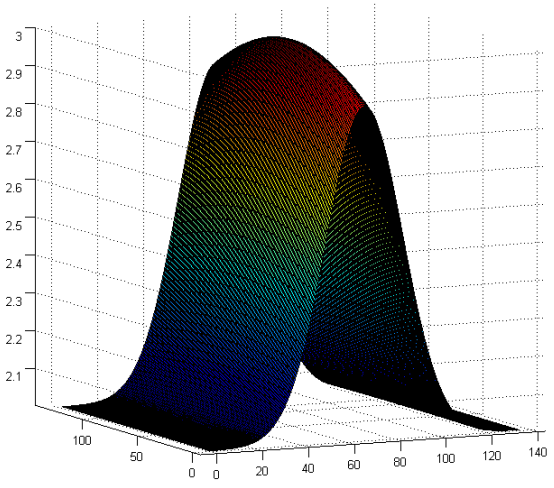

Figure (5.4). *Three dimensional rendering of the weighting function in Eq. 5.5 used to score lesions in Fig. 5.6b.*

lesion.

This solution enable us to reduce the number of false positive, i.e. of hyperintense regions erroneously recognized as lesions. An example of the advantage introduced is shown in Fig. 5.7 , where only one cortical lesion (highlighted by the light blue arrow) has been detected by three human raters: the leftmost and the central panel correspond to the case in which no weighting function is used, which corresponds to setting the value of l constant throughout the whole image in Eq. 5.3. In particular, in the leftmost panel l has been set equal to 1, while in the central panel it has been set equal to 3. In the former case the lesion is correctly segmented, but many false positives are erroneously introduced, at the expense of the algorithm's specificity. On the other hand, in the latter case we have been less conservative, thus diminishing the number of false positive, but we are not able to detect the cortical lesion anymore. The rightmost panel shows the result obtained with the use of the weighting function in Eq. 5.5: the actual lesion is correctly identified, and the number of false positive is acceptable.

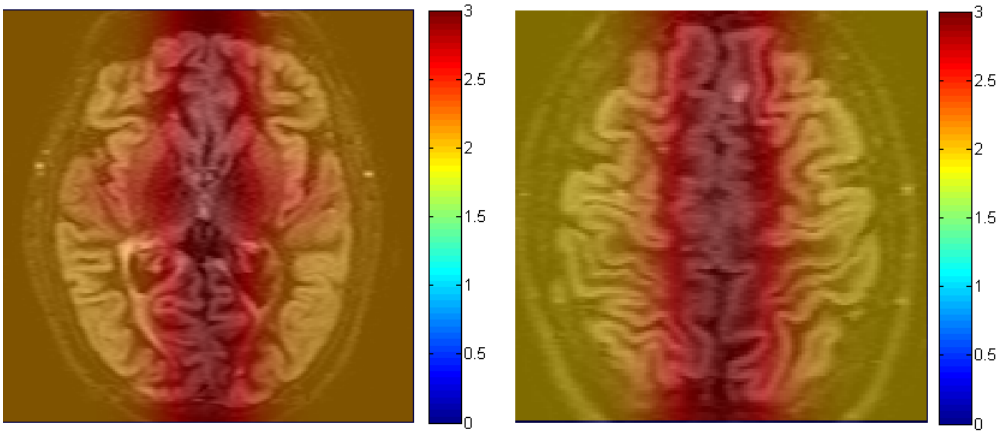

Figure (5.5). *Example of two axial slices of DIR sequence, with superimposed the transparency of the weighting function used to score lesions.*

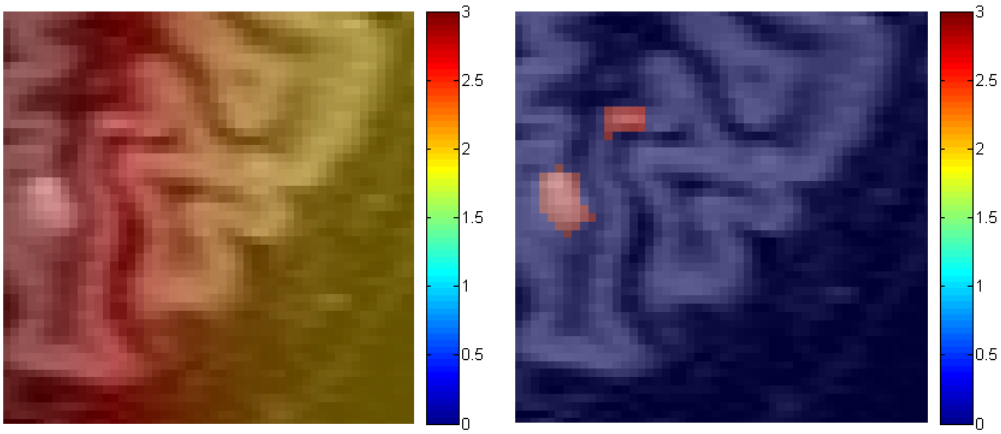

Figure (5.6). *Example of an axial slice of DIR sequence, with superimposed the transparency of the weighting function used to score lesions: magnification (left panel) and mask on the two candidate lesions (right panel).*

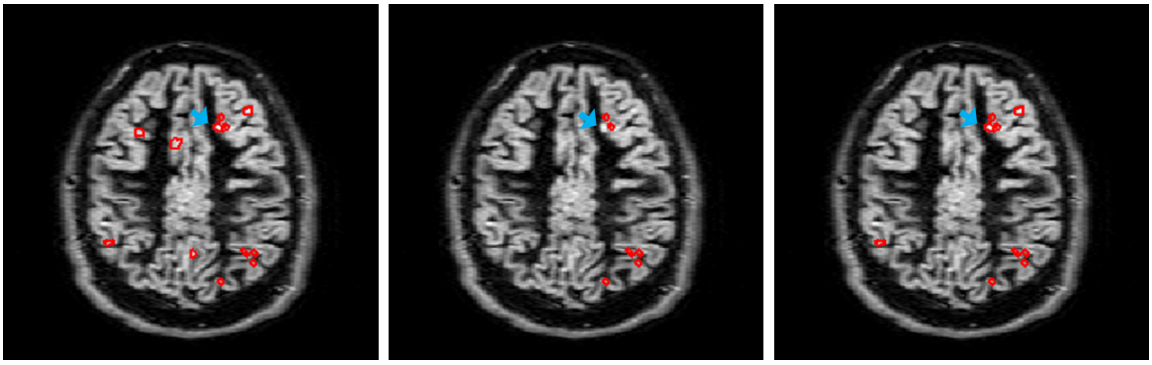

Figure (5.7). *Example of the usefulness of the kernel function.*

Chapter 6

Results

As observed by Lladó et al., ([49]), numerous approaches to lesion detection and quantification have been proposed in literature, based on different approaches. However, despite this variety, none of them provide a fully automatic procedure that includes all the required steps to help in the diagnosis and treatment follow-up.
Ideally, in order to test the performance of an automatic lesion detector, it should be applied to a common database and compared with a ground truth. This is, however, almost impracticable because of the lack of common public databases of real images acquired from MS patients along with their ground truth.

6.1 Manual Segmentation

In our study, MS lesions were manually identified by two experienced neurologists who were not aware of the results of our automatic method. They were asked to manually highlight MS cortical lesions in DIR images with possible visual inspection of the corresponding FLAIR and T_1-weighted images. The voxels corresponding to a cortical lesion as defined in [34] were manually identified. When the two human raters provided different evaluation of a cortical region, they were asked to reach a consensus. The final results were used as ground truth for the evaluation of the performance of our algorithm. Besides, for a subset of patients we were provided with the blinded manual

segmentation performed by three raters. In order to test the importance of inter-operator variability, we did not make them come to a consensus, when their results did not agree. This allowed us to gain an insight into the difficulty of the data. In fact, as pointed out in [49], the degree of difficulty of the data to be analyzed should be taken into account. This parameter can be quantified considering the variability of the results provided by different experts. For example, Zijdenbos et al. ([107]) used the coefficient of variation computed among the experts from seven different institutes to demonstrate that the image data they used was complicated and resulted in large variability even among the experts.

6.2 Performance metrics

On DIR images, the lesions were recognized for their high-signal intensity. Lesions had different locations: infratentorial, periventricular WM, deep WM, juxtacortical WM (not entering the cortical GM), mixed WM-GM, and intracortical. Following Geurts et al. ([34]), it was decided to score cortical lesions, which had to be entirely or partly located in the cortical GM. Subpial demyelination and lesions located in WM directly adjacent to the cortex were not scored. The intracortical lesions were distinguishable as lesions confined to the cortical ribbon without involving the underlying subcortical WM. However, considering the actual resolution of our images, the possibility that some intracortical lesions extend into the juxtacortical WM cannot be excluded.
In order to test the capability of our algorithm in correctly finding true cortical lesions, we used different metrics. In particular, we computed the sensitivity index (Eq. 6.1) and Dice's similarity index (Eq. 6.2). Besides, we wanted to investigate whether there could be a relationship between the number of false positive, which typically are local hyperintense regions though they are not classifiable as lesions, and the total number of true lesions. To do so we computed the fraction of false positive (FFP) (Eq. 6.3). The aim of the latter index computation was twofold: on one hand we wanted to check if it was possible that an increased number of false positive may be correlated with a high number of cortical lesions. On the other hand we have a long-term purpose, which consists in keeping trace of the false positive, in order to verify whether

they turn into actual lesions in follow up examinations.

The sensitivity index, Dice's similarity index, and fraction of false positive are respectively defined as

$$\text{Sensitivity} = \frac{TP}{TP + FN} \tag{6.1}$$

$$\text{Dice} = \frac{2TP}{2TP + FP + FN} \tag{6.2}$$

$$\text{FFP} = \frac{FP}{TP + FN} \tag{6.3}$$

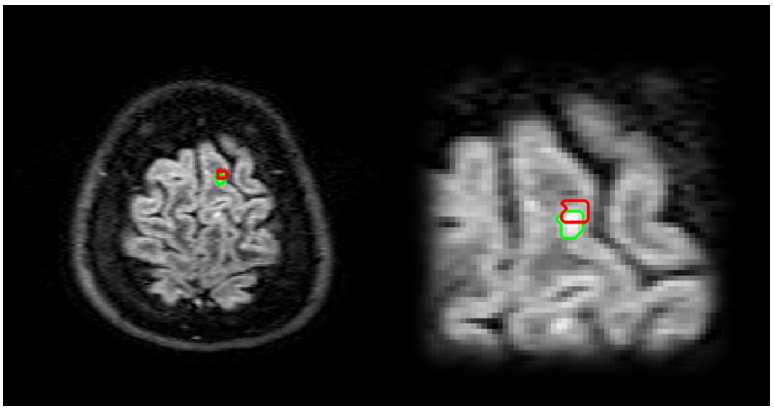

Figure (6.1). *Example of partial overlapping between an automatically identified lesion (red line) and the corresponding manually outlined lesion (green line) on an axial DIR slice (on the left), with a magnification (on the right).*

where TP is the number of true positive, FP is the number of false positive, and FN is the number of false negative. The number of TP accounts for all the pixels belonging both to a region segmented by the algorithm and to a region provided by the clinicians' consensus. The number of FP accounts for all the pixels erroneously included in the automatically segmented lesions by the proposed method. Finally, the number of FN accounts for all the pixels that, according to the consensus, represent cortical lesions but that have been erroneously excluded by the proposed method. For a good segmentation, both sensitivity and Dice's index should be close to 1. As far as fraction of false positive is concerned, it does not have an upper bound since the number of

false positive may be much greater than the denominator of Eq.6.3, which represents the total number of positive.
We considered that a lesion was correctly identified, thus increasing the number of true positive, when the intersection between the true lesion (i.e. the result of the manual segmentation) and the automatic one covers at least the 12.5% of the area of the true lesion (Fig. 6.1), and if the number of voxels identified automatically and not intersecting the true lesion is lower than twice the true lesion perimeter length. If these two conditions are not met, we considered a FN corresponding to the missed lesion, and a FP due to the erroneously selected automatic region. Given the huge number of true negatives per subject, which are given by all the voxel that do not represent a lesion and that are not classified as lesion, the computation of both specificity and accuracy revealed to be poorly significant. Anyway, the use of Dice's index provides a metrics that takes into account not only the rate of actual CLs detected, but also the normal appearing GM erroneously classified as lesion.
Moreover, in order to test the repeatability of our method, we were provided with a scan-rescan acquisition performed on a group of subjects: after a first scan, the patients were required to exit the scanner and reenter at a later time for a second scan.
Finally, to test the entity of inter-operator variability, we computed the same indexes between each possible combination of the three raters r1, r2, and r3 (i.e., r1 *vs* r2, r1 *vs* r3, and r2 *vs* r3), previously described (Sec. 6.1).

6.3 Materials

6.3.1 Patients Population

Fifty-one patients (37 women and 14 men, overall mean age 34.0 $\pm$ 10.7 years, range 18-65 years) affected by Relapsing Remitting Multiple Sclerosis (RRMS) who consecutively presented to the Multiple Sclerosis Centre of Veneto Region from June to October 2009 were included in the study. The mean disease duration was 11 $\pm$ 7.5 years, range 2-31 years. All patients were clinically assessed by means of the Kurtzke Expanded Disability Status Scale (EDSS) ([50]) (mean EDSS score 3.0 $\pm$ 1.6, range 1-6.5) and MR eval-

uations. Twenty eight patients were treated with immunomodulatory drug whereas the rest of the group were therapy free. The study was approved by the local Ethic Committee and written informed consent was obtained from all subjects. All the fifty-one patients of the dataset were manually segmented by two experienced neurologists, who came to a consensus when their individual results differed.
Moreover, in order to test the repeatability of our method, 3 additional subjects underwent a scan-rescan acquisition: after a first scan, the patients were required to exit the scanner and reenter at a later time for a second scan.
Finally, in order to test inter-operator variability, in a subset of 28 patients, cortical MS lesions were manually segmented by three raters, who were blinded to each other.

6.3.2 MR Volume Acquisition

MRI volumes were acquired using a 1.5T MRI scanner, *Philips Achieva 1.5T A-series, Philips Medical System, Best, The Netherlands*, with 33mT/m power gradient, using a 16 channel head coil. MRI examination protocol included FLAIR sequence (repetition time (TR)=10000 ms, echo time (TE)=120 ms, inversion time (TI)=2500 ms, 50 contiguous axial slices, images with a field of view (FOV) of 250×250, a matrix of 288×288, slice thickness = 3 mm, in-plane resolution of 0.75 mm^2), DIR sequence (TR = 15631 ms, TE = 25 ms, TI = 3400 ms, 50 contiguous axial slices, images with a field of viwe of 250×250, a matrix of 256×256, in-plane resolution of 1 mm^2, with a thickness = 3 mm) and T_1-w sequence (TR=25 ms, TE=4.6 ms, 120 contiguous axial slices with a thickness = 1.2 mm, in-plane resolution of 0.9 mm^2, a matrix size=256×256). The complete MRI acquisition protocol for the study is summarized in Table 6.1.

6.4 Results

On the 51 provided volumes, a total number of 475 cortical lesions were manually detected by the raters, who were blind to the result of our algorithm.

Table (6.1). *MRI protocol acquisition for MS patients: acquired sequences and sequences parameters.*

MR sequence	**DTI**	**DIR**	**T1W-3D**	**T2W**	**DUAL-TSE**	**FLAIR**	**SE-T1W**	
Base Seq.	SE	IR	FFE	SE	SE	IR	SE	SE
Fast Mode	EPI	TSE	-	TSE	TSE	TSE	-	-
FOV $[mm]$	240	250	250	240	250	250	250	250
RFOV $[\%]$	100	80	80	100	85	80	80	80
Scan Perc. $[\%]$	100	70	80	80	80	80	80	80
SENSE	2	no	no	1,5	no	no	no	no
Acquired Matrix	96×96	256×256	256×256	256×256	256×256	240×240	224×224	192×192
Reconstr. Matrix	256×256	256×256	256×256	256×256	256×256	288×288	256×256	256×256
Num slice	50	50	120	20	20	50	20	20
Slice Thick. $[mm]$	3	3	1.2	5	5	3	5.5	4.5
Gap $[mm]$	0	0	0	1	1	0	1	0.45
Echoes	1	1	1	1	2	1	1	1
TE $[ms]$	74	25	4.6	100	20 - 120	120	10	12.1
Flip Angle	$90°$	-	$30°$	$90°$	$90°$	$100°$	$90°$	$69°$
TR $[s]$	8	15	0.025	4	2.2	10 s	0.6	0.4
TI $[s]$	-	3.4	-	-	-	-	-	-
Delay TI $[ms]$	-	285	-	-	-	-	-	-
IR/TI $[s]$	-	-	-	-	-	2.5	-	-

The detection has been performed on each two-dimensional slice, i.e. lesions that were present in two contiguous slices were counted twice. Similarly, lesions that covered three slices were counted three times, and so on. Of the 475 true, 450 were correctly recognized by the proposed algorithm, providing a number of false negatives of 25 lesions, which represent the 5.26% of all the lesions recognized by the raters. The percentage of sensitivity is therefore 94.74%, with a Pearson correlation coefficient of 0.998 (Fig. 6.2).

At a global level, an open issue is represented by the not trivial number of false positives: on the entire dataset, the algorithm found 3576 hyperintense regions that were not cortical lesions. All these false positives can be due either to noise or to other lesions that are not cortical, but that extend through white matter, or that are entirely enclosed in white matter. As far as the latter source of false positives is concerned, remind that our GM segmentation algorithm does not make use of any anatomical information (see Chap. 4). Therefore it is possible that some white matter lesions, being hyperintense both in FLAIR and in DIR sequence, are erroneously included in the gray matter volume. In Fig. 6.3 some examples of occurred false posi-

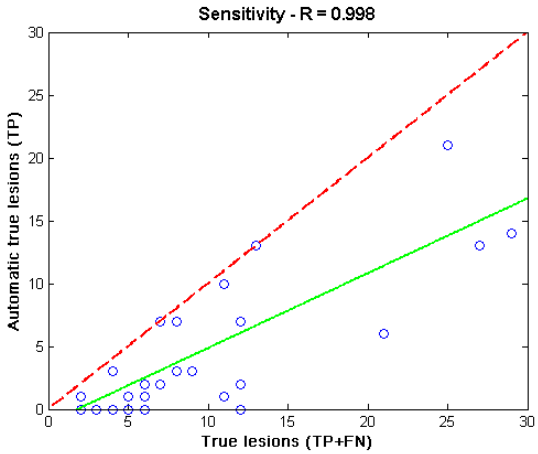

Figure (6.2). *Correlation between the true lesions present in each volume (true positive and false negative, x-axis), and those correctly identified by the algorithm(true positive, y-axis)). The dashed line is the bisector of the first and third quadrants; the solid line is the evaluated linear regression.*

tives are shown. The four images represent four contiguous DIR slices of the same subject. The segmented regions represent the result of the algorithm, i.e. what has been automatically classified as hyperintense gray matter. We have used a light-blue line to picture all the true positives, i.e. all the regions that had been classified as lesions by the neurologists. Red regions are all those automatically detected regions that do not belong to the manually outlined set. Some considerations should be done: the big cortical lesion in panel C is clearly connected to those regions in panel A, B and D that have been highlighted with yellow arrows. Similarly, the cortical lesion in panel D is connected to the region in panel C highlighted by the yellow arrow. So, regions pointed by the yellow arrows are not pure false positives, but can be considered as *mass effect* ([94]): it is known, in fact, that the effect of a lesion can influence the appearance of surrounding tissues.

Other false positives can be due to white matter lesions, which are hyperintense both in FLAIR and in DIR sequence: an example can be seen again in Fig. 6.3, where white matter lesions erroneously segmented have been highlighted either with a yellow arrowhead (if they are entirely included in the white matter) or with an orange arrowhead (if they are adjacent to the gray

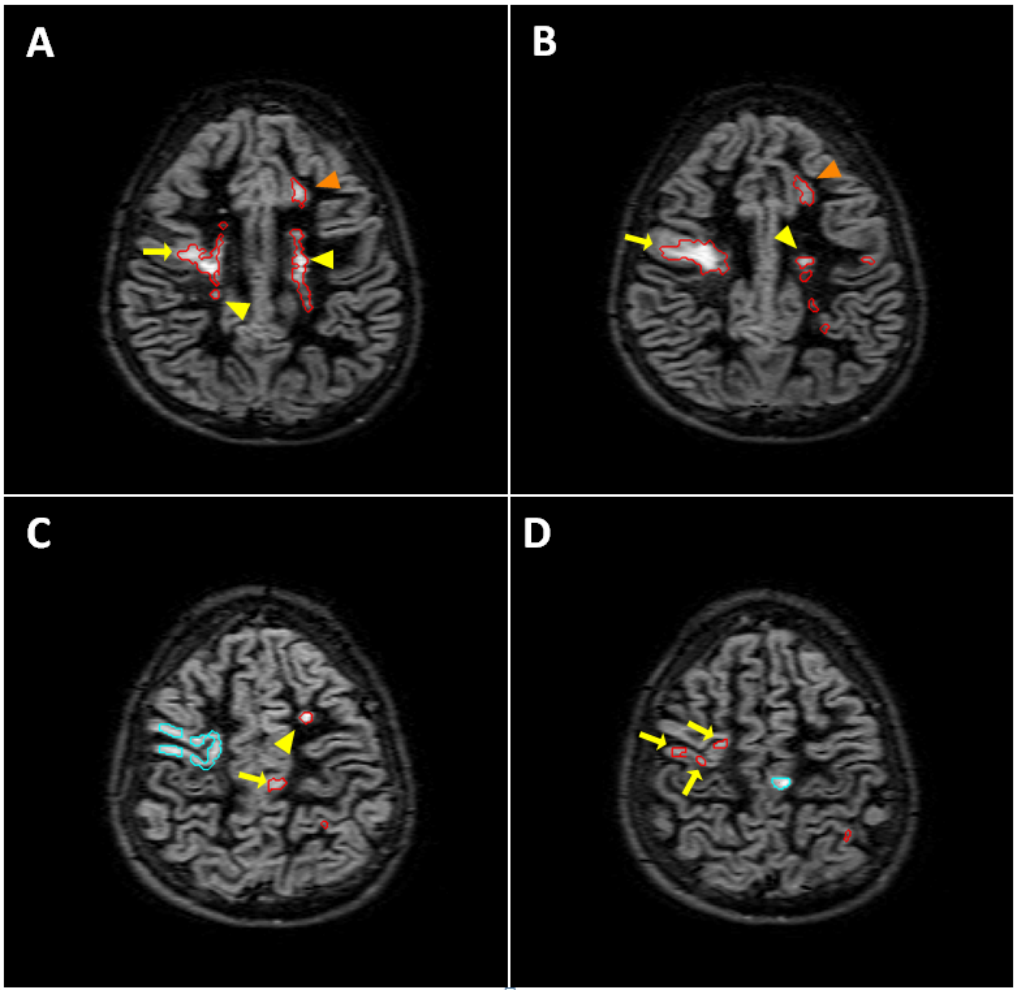

Figure (6.3). *Examples of correctly (TP, blue lines) and incorrectly (FP, red lines) detected lesions. Yellow arrows point FP that are actually connected to a cortical lesion that infiltrates into adjacent tissues. Arrowheads point white matter lesions, either entirely included in the white matter (yellow arrowhead) or adjacent to the gray matter (orange arrowhead).*

matter).

In the light of these considerations, a small value of Dice's index is expected: the resulting value is in fact 18.66%. Similarly the FFP, which is 19.43, is expected to be high. It should be also considered what has been recently pointed out by Seewann et al. ([83]): the number of cortical lesions that a human rater is able to see on an MRI exam is just the so-called *tip-of-the-iceberg* phenomenon. In fact, post mortem histopathological studies have shown that the actual lesion load is much greater. So it is possible that those regions that are automatically segmented by the algorithm may represent areas in which the normal tissue is altered, though they appear as normal tissue to a human rater.

On the additional 3 subjects for which scan-rescan data were acquired, we obtained a good match between the estimated number and position of lesions in the two acquired volumes. For all subjects, the number of estimated lesions (TP+FP) shows a correlation of 96.9% . A total number of 6 scans (2 for each of the 3 subjects) were analyzed by the raters at different times. It is worth noting that only in one of the three subjects there was a complete agreement between the manual segmentation performed on the first and on the second scan. In fact, because of the large slice thickness of DIR sequence, small lesions may fall between two slices during one volume acquisition; during the second acquisition, small movements of the patient may change the visibility of these lesions.

As far as inter-operator variability is concerned, we were provided with 28 MRI volumes on which cortical lesion segmentation had been performed by three raters. In Fig. 6.4, 6.5, and6.6 the correlation evaluated between each possible combination of raters is shown. For each of the three possible combination, we considered one of the two raters as the ground truth, and evaluated the sensitivity rate according to Eq. 6.1, resulting in 41.94%, 61.08%, and 66.61%. This means not only that the acquired data were difficult to be analyzed, but also that when performing manual segmentation, a consensus between two or more experts is always recommendable.

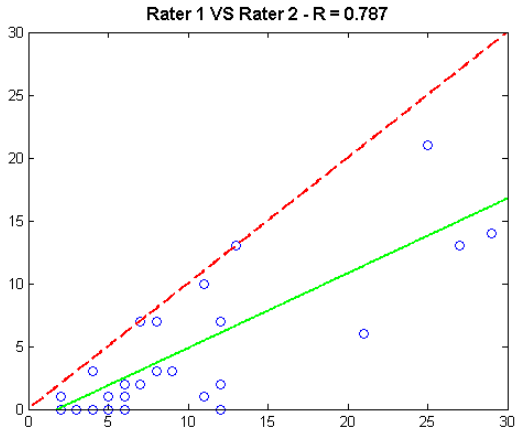

Figure (6.4). *Correlation between the lesions scored by rater 1 and rater 2. The dashed line is the bisector of the first and third quadrants; the solid line is the evaluated linear regression.*

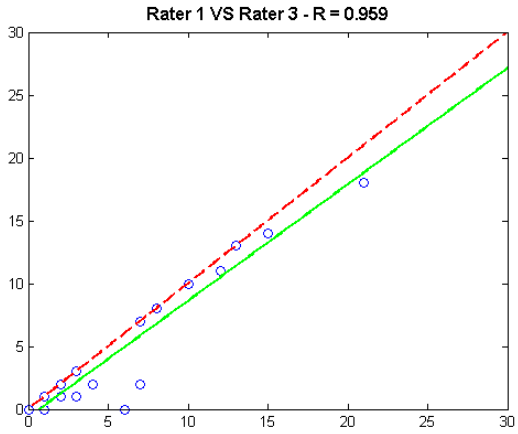

Figure (6.5). *Correlation between the lesions scored by rater 1 and rater 3. The dashed line is the bisector of the first and third quadrants; the solid line is the evaluated linear regression.*

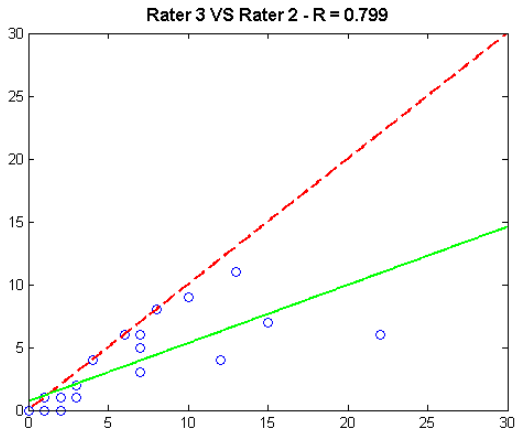

Figure (6.6). *Correlation between the lesions scored by rater 2 and rater 3. The dashed line is the bisector of the first and third quadrants; the solid line is the evaluated linear regression.*

Chapter 7

Tissue Iron Quantification

As it has been explained in Section 2.8.1, increased iron accumulation in gray matter has been described in MS and is believed to be indicative of neurodegeneration. Recently, R_2^* relaxometry has been proved as sensitive means to quantitatively assess brain iron concentrations ([52]). In particular, the transverse relaxation rates R_2 and R_2^* followed the same trend as the iron concentrations determined chemically, with R_2^* being more sensitivity than R_2 to variations in iron concentration. R_2^* indicates the reversible transverse relaxation rate and is, together with the resonance frequency, particularly sensitive to spatial magnetic susceptibility variations. Both iron and myelin have been suggested to alter the magnetic susceptibility ([27],[37]), but experimental confirmation is lacking. As it has been demonstrated by Fukunaga et al. ([31]), MRI contrast and iron staining show strong similarities. Areas of increased R_2^* relaxation in the white matter show increased iron staining. In the gray matter, a laminar distribution of iron is observed with a pattern that resembles the MRI contrast (Figure 7.1). These results would open the way to quantify iron content by combining R_2^*, R_2, and frequency data, because these measures are differentially affected by iron and myelin content. For example, as recalled in [31], iron and myelin both increase R_2 and R_2^*, whereas they have opposing effects on the resonance frequency (paramagnetic vs. diamagnetic shift, respectively).

Currently, different MRI techniques are available for the assessment of

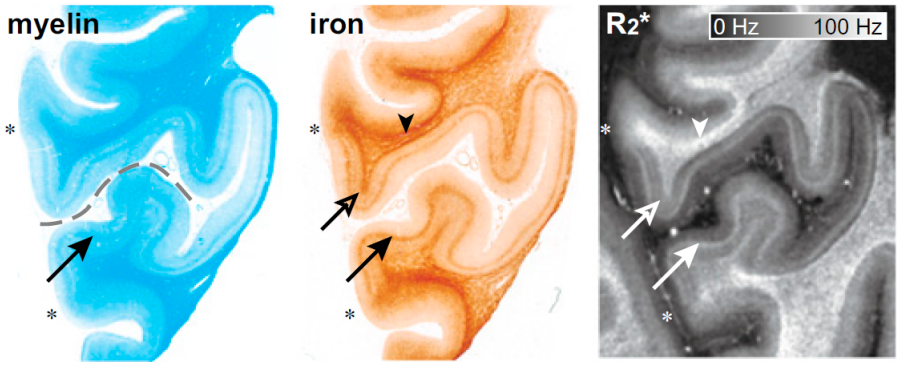

Figure (7.1). *Histochemical myelin (left) and iron (middle) staining and MRI R_2^* data (right) in the visual cortex. The MRI data are coherent with the iron stain, with increased R_2^* in the line of Gennari (solid arrow), in the deeper layers (open arrow), and in subcortical WM in the secondary visual cortex (arrowhead). Images adapted from [31]*

brain iron. A recent work by Pitt et al. ([73]) has investigated the sensitivity of T_2^*-weighted gradient-echo (T_2^*GRE) and inversion recovery turbo-field-echo (TFE) sequences for cortical MS lesions at 7 T, comparing the MRI results with the corresponding histopathological analysis. A first, important finding was that, because of expansion and eventual fusion of different type lesions, cortical lesions could not always be assigned to one single lesion category according to the classification by Bö et al. ([7]) (Figure 7.2). Besides, both the utilized MRI techniques showed several thinly myelinated cortical lesions (Figure 7.3), which might represent remyelinated lesions. More importantly, most cortical plaques as imaged by the T_2^*GRE sequence showed homogeneous, hyperintense signals on magnitude images. Some lesions displayed heterogeneous signal patterns, i.e. mixed hypointense and hyperintense signals or, more commonly, peripheral hypointense halos around a hyperintense lesion center (Figure 7.4). The correlation between these images and the tissue sections that were labeled (either with anti-CD68 antibody or stained with Perls (iron) stain) demonstrated a close association of hypointense MRI signal with the presence of iron-rich microglia within or at the edge of active and chronic active lesions. The staging of cortical lesions according to their inflammatory activity is determined by the density and distribution of macro-

phages or microglia. In particular, *active cortical lesions* have a distinct border of macrophages or microglia at the lesion edge and cores with increased macrophage or microglia density compared with normal cortex. *Chronic active cortical lesions* have a border of macrophages or microglia (usually thinner than active lesions) but decreased or normal densities in their centers compared with normal cortex. *Chronic inactive cortical lesions* show no increase in macrophage or microglia density at the lesion border or the center.

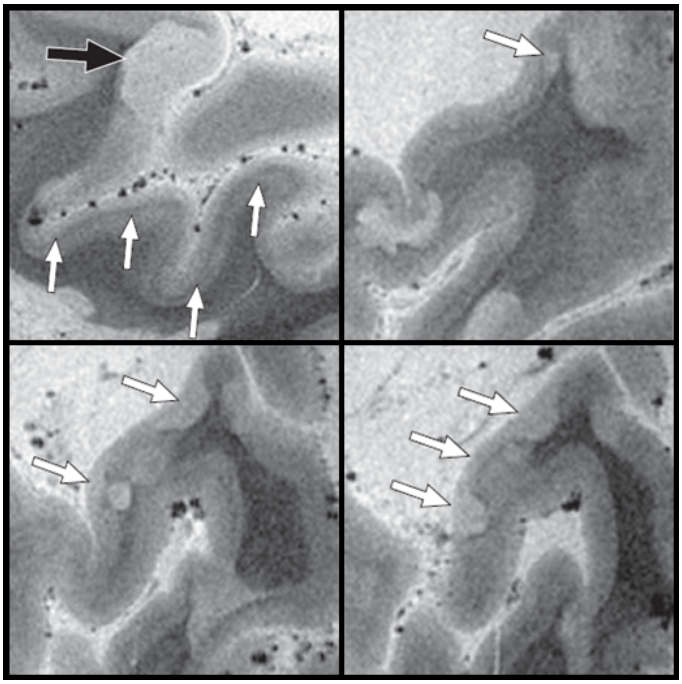

Figure (7.2). *Examples of T_2^*-w GRE MR images. Top left panel: a type IV cortical lesion (black arrow) and the line of Gennari (white arrows). Top right panel and bottom panels: evolution of a cortical lesion, from a round type II lesion (top right) into a type IV lesion, fusing with a second lesion (bottom). Images adapted from [73].*

Starting from the results provided by Pitt et al. ([73]), i.e. that hypointense rings in patients with MS represent activated microglia or macrophages, we wanted to investigate whether it is possible to stage MS lesions by inflammatory activity in vivo. Different MRI techniques are used for the assessment of brain iron (i.e. relaxation time mapping, phase imaging, susceptibility-weighted imaging, susceptibility mapping, magnetic field correlation imaging, direct saturation imaging), but they are usually employed

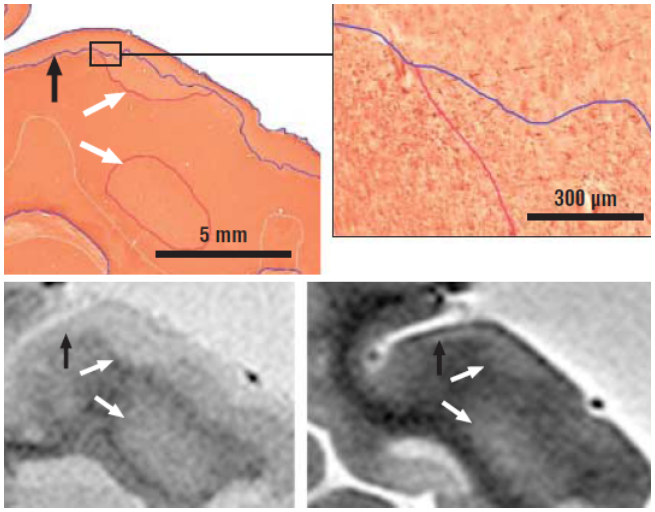

Figure (7.3). *Examples cortical lesions. Top panels: myelin-labeled section with demyelinated (black arrow) and thinly myelinated (white arrows) CLs, and magnification. Bottom panels: both T_2^*-w GRE sequence (left panel) and white matter-attenuated turbo-field-echo sequence show demyelination (black arrows) and thin myelination (white arrows). Images adapted from [73].*

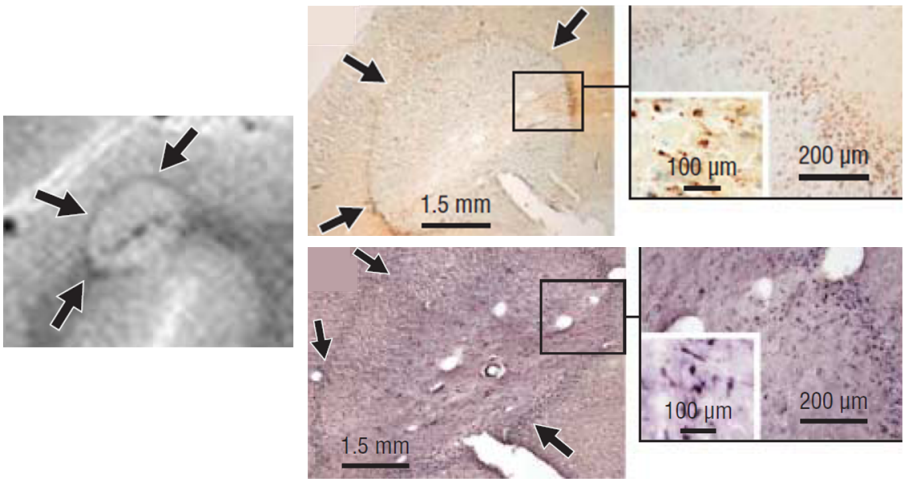

Figure (7.4). *Example of a leukocortical lesion. Leftmost panel: T_2^*-w GRE image showing a hypointense rim (black arrows). Upper middle and right panels: the same hypointense rim corresponds to activated microglia at the lesion border (black arrows). Bottom middle and right panels: again the same rim visible with Perls staining. Images adapted from [73].*

for imaging purposes, rather than for quantification (for an extensive review, see [81]). Our purpose, instead, is to quantitatively estimate the value of T_2^* (or, equivalently, of $R_2^* = \frac{1}{T_2^*}$). In a recent work, Aquino et al. ([4]) calculated R_2^* maps in a cohort of healthy people in order both to determine the values of iron accumulation in the basal ganglia at different ages, and to compare the results with previously reported iron concentrations found in autopsy material. The conclusion drawn by the authors was that R_2^* estimations do help to quantify brain iron accumulation.

7.1 Materials and Methods

7.1.1 Set up of the MRI Sequence

MRI volumes were acquired using a 1.5T MRI scanner, Philips Achieva 1.5T A-series, Philips Medical System, Best, The Netherlands, with 33mT/m power gradient, using a 16 channel head coil. A multiecho GRASE sequence was acquired (repetition time: 4000 ms; matrix: 256×256; field of view: 230×183; section thickness: 3 mm; flip angle: $90°$) with five echo times at 20, 40, 60, 80 and 100ms (Figure 7.5). This MRI sequence was chosen and adapted in order to acquire a number of echoes sufficient to estimate the value of R2*, which is often linearly related to iron concentration ([105]).
Being that the project concerning cortical lesions classification on the basis of iron overload is still at an early stage, only one MRI acquisition has been performed so far. Actually, several acquisitions have been made in order to design the proper MRI acquisition protocol, i.e. the one on which the estimation of R2* could be done. The five echo times provided by the described multiecho GRASE sequence have proved to be the proper compromise between the need of multiple echo times and the necessity to keep the acquisition time as short as possible.

7.1.2 Choice of the model

R2* maps were calculated on a voxelwise basis using non-linear least-squares fitting function. Different models, as described in [42], have been tested. The signal intensity decay $S(t)$ was finally expressed with a monoexponen-

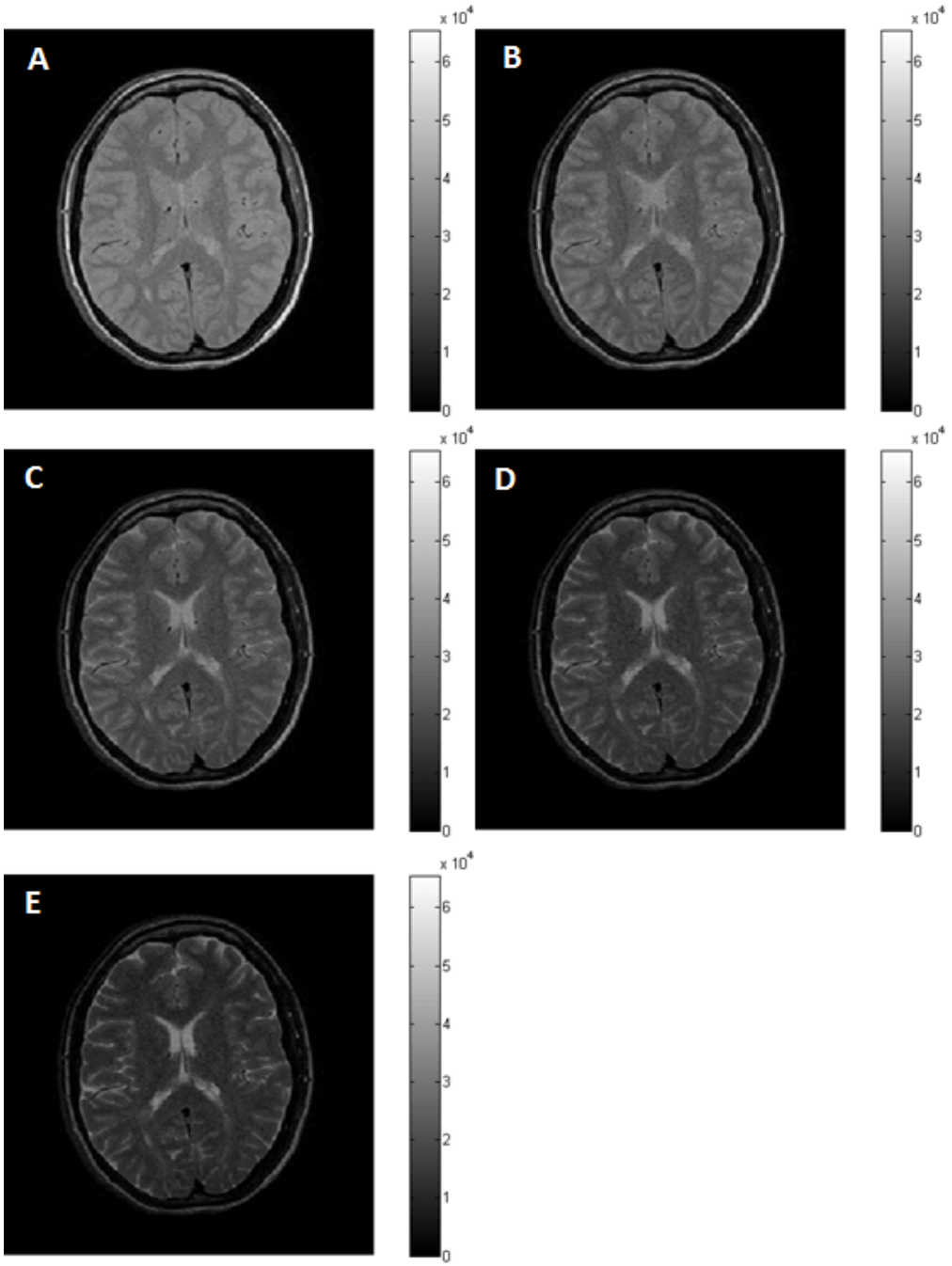

Figure (7.5). *Example of the same slice acquired at different echo times: 20 ms (A), 40 ms (B), 60 ms (C), 80 ms (D), 100 ms (E).*

tial model by using the

$$S(t) = S(0)\exp(-TE \cdot R_2^*) \tag{7.1}$$

where $S(t)$ is the signal intensity at the time t, $S(0)$ is the initial signal intensity, and TE is the echo time. By using this model, it is possible to fit the temporal samples so to obtain, voxel by voxel, the estimate of R_2^* (expressed in s^{-1}) and of its inverse, the relaxation time T_2^*.
The model has been chosen in the light of residual analysis (whiteness and independence test), estimates' accuracy, and estimates' physiological significance. It has been assumed a constant standard deviation for the measurements, i.e. it equally weights all the samples.

7.1.3 Results and Discussion

Few works have been done so far in order to quantitatively estimate either R_2^* or T_2^* in MS lesions ([53], [16]). Similarly, in literature the number of publications concerning quantitative estimation of brain iron in vivo is limited. Being that this part of the thesis is still at an experimental stage, the multiecho GRASE volume has been acquired just on one patient, who was not affected by MS. In fact the aim of the acquisition was twofold: on one hand we needed to test whether the sequence was appropriate for the subsequent R_2^* estimation. On the other hand, we wanted also to check whether the estimates provided by the model in Eq. 7.1 were proper and comparable with those values reported in literature.
Under these assumption, we decided to manually draw different ROIs corresponding to some peculiar brain tissues. In particular, the putamen and the globus pallidus were chosen and manually segmented, both in the left and in the right hemisphere (Fig. 7.6). The mean values of the R_2^* estimated inside these regions (Fig. 7.7) were considered and compared with the values derivable from literature. Besides, we verified that the R_2^* estimated in one tissue did not change through different slices: in fact we expected that the value of R_2^*, which should be characteristic of the tissue, did not vary significantly between different slides, when considering the same brain structure. The results are shown in Tab. 7.1: in the first six rows we recall values reported in

literature. The last three rows, instead, shows the estimates obtained on our MRI sequence with our estimating model. It should be noticed that the results are comparable with literature. Besides, even if we estimated the value of R_2^* in the putamen considering two different slices, the two results obtained are equal.

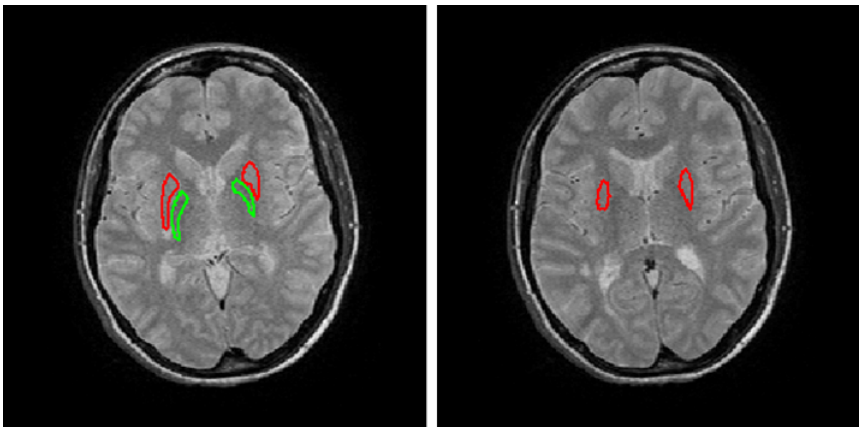

Figure (7.6). *Two dimensional ROIs of the putamen (red line) and of the globus pallidus (green line).*

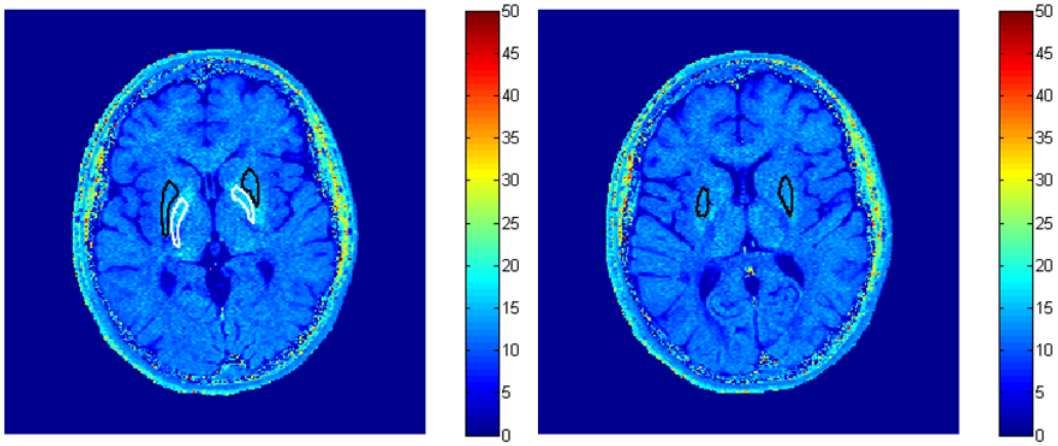

Figure (7.7). *R_2^* maps obtained for different slices. The putamen (black line) and the globus pallidus (white line) have been manually outlined.*

In this chapter we have thus described the design of a technique which is intended to be used to characterize, if possible, cortical lesions. In fact

the described procedure will be applied to MS patients' data, in order to verify whether cortical lesions exhibit different R_2^* patterns according to their inflammatory activity. In particular, in order to verify results obtained in vivo, other techniques (i.e. contrast enhanced T1-weighted sequence using Gadolinium) should be coupled, that are commonly used to enhance active MS lesions. It then could be possible to confirm whether the two sequences' results agree: this would imply that cortical lesion activity can be characterized avoiding the use of Gadolinium or any other dye.

Table (7.1). *Comparison of different literature results in R_2^* quantification and of the results obtained by our quantification algorithm.*

Reference	B_0	Sequence type	Tissue	R_2^* $[s^{-1}]$
Aquino et al. ([4])	1.5 T	GRE	Putamen	22.69 ± 0.89
Aquino et al. ([4])	1.5 T	GRE	Globus Pallidus	27.03 ± 0.98
Cohen-Adad et al. ([16])	7 T	FLASH-T2* spoiled GRE	Cortex (controls)	32.6 ± 1.8
Cohen-Adad et al. ([16])	7 T	FLASH-T2* spoiled GRE	Cortex (MS patients)	31.6 ± 1.9
Langkammer et al. ([53])	3 T	spoiled GRE	WM MS lesions	14.3 ± 3.0
Langkammer et al. ([53])	3 T	spoiled GRE	WM controls	20.1 ± 1.3
Our method	1.5 T	GRASE	Globus Pallidus	15.09 ± 2.99
Our method	1.5 T	GRASE	Putamen (slice 14)	13.52 ± 1.55
Our method	1.5 T	GRASE	Putamen (slice 16)	13.55 ± 1.52

Chapter 8

Conclusions

8.1 Achieving the Objectives

The aim of this thesis was to develop a technique for the automatic segmentation and characterization of cortical lesions in multiple sclerosis, exploiting specific magnetic resonance sequences. Cortical involvement has been recently considered a relevant aspect of MS pathology. Cortical MS lesions are a frequent phenomenon in MS since the disease onset; they typically show less inflammatory components than WM lesions, being mainly characterized by demyelination, axonal transection, and apoptotic loss of neurons, and seem to play a relevant role in driving the clinical and cognitive progression of MS. In addition, cortical lesions seem to have the same spatial distribution of the cortical atrophy in MS thus suggesting a possible role of cortical lesions in determining its development ([13]).
Demyelination of the GM is relatively sparse in the beginning phases of the disease but then it rapidly increases when the disease progresses. Extensive demyelination in the cortex is associated with a more progressive phase of the disease. Besides, cortical, juxtacortical, hypothalamic, and hippocampal lesions have been shown to correlate with the degree of clinical disability ([35]). The set aim has been achieved by breaking down the global problem into different steps: gray matter segmentation, cortical lesions segmentation, and cortical lesions characterization.

8.2 Gray Matter Segmentation

In order to detect cortical lesions, a fundamental prerequisite is represented by an accurate gray matter segmentation. When dealing with images acquired from non healthy people, the problem of brain tissues segmentation is a complex one, where even commonly available brain imaging software often fail. This is due to the fact that the disease locally alters the tissues' characteristics, thus making them appear in a non homogeneous way on a magnetic resonance examination. Segmentation mistakes are also common when specific pulse MR sequences are acquired instead of standard T_1-weighted sequences. The consequence is that an operator is required to check the automatic segmentation in order to manually correct it, an operation that is always time consuming and that introduces operator variability into the measurements.

In our work we are dealing with the two mentioned problems i.e., we are using FLAIR and DIR MRI sequences instead of the usual T_1-weighted sequence; besides, we are working on images acquired from MS patients, which are often anomalous in their appearance due to the tissue structural changes caused by the disease. For these reasons, we avoid the use of any anatomical a priori information, which may be misleading in the presence of a disease.

The brain extraction and the gray matter segmentation have been obtained using the level set method, a numerical technique used in image analysis to segment objects and shapes. In particular, we adapted the Local Binary Fitting method, using it for the first time in a multimodal approach: in fact, there is no MRI sequence that provides both a tissue contrast sufficient for a level set evolution and that at the same time offers enough resolution to allow a well defined delineation of the tissues' boundaries. So a first segmentation was performed on FLAIR sequence, which has been designed in order to provide a well defined contrast between CSF and GM. The disadvantage is a poor contrast between GM and WM, combined with a weak highlighting of MS lesions in GM.

Therefore the first segmentation is designed to provide a good brain extraction, i.e. gray and white matter are delineated, discarding the CSF. The second segmentation is then performed on DIR sequence, designed to highlight

gray matter alone, suppressing both white matter and cerebrospinal fluid. This segmentation takes advantages of the results obtained on the corresponding FLAIR images. The cascade of the two level set based segmentations, each on a different MRI sequence, provides with great accuracy the gray matter volume, on which cortical lesions are located.

8.3 Cortical Lesions Segmentation

The availability of DIR sequence has enabled a reliable in vivo identification of cortical lesions in MS patients. Although DIR imaging does not allow the detection of all the lesions which are known to be present in the cortex of MS patients ([83]), this sequence undoubtedly provides a more complete and detailed picture of the focal disease burden in the brain. Thus, those symptoms which are expression of cortical dysfunctions in MS (such as epilepsy and cognitive impairment) could be better investigated by using DIR. Moreover, the use of DIR in MS monitoring might also represent a useful paraclinical tool to assess treatment efficacy, by providing additional pieces of information on possible disease manifestations which would remain undisclosed by conventional MRI.
However, to the best of our knowledge the diagnosis and monitoring of the disease is mainly based on visual detection of MRI lesions ([62]), a process that is always time consuming, error prone and operator dependent. Moreover the identification of cortical lesions requires an accurate training of the operator in order to avoid any lesion misclassification.
Although in DIR sequence cortical lesions usually appear as hyperintense regions, the use of a simple threshold to detect them reveals to be insufficient. This is mainly due to problems of bias field inhomogeneities, which corrupt the acquired images. Besides, the use of a double inversion, which characterizes DIR sequence, lessens the signal-to-noise ratio of this acquisition technique. Last but not least, this MRI sequence has some common artifact-prone areas in which the gray matter tends to be brighter than in the rest of the volume. All these evidences have been taken into account in the proposed segmentation algorithm.
Starting from the previously obtained gray matter segmentation, we auto-

matically detect those regions in DIR that appear as localized hyperintense areas. According to the consensus criteria defined by Geurts et al. ([34]), these are highly suspectable of being actual cortical lesions. This detection is performed slice by slice, on a tessellation of the image, in order to overcome the problem of bias field inhomogeneities. The problem of artifact-prone areas has been tackled by using weighting functions that allow to be more or less restrictive when looking for cortical lesions, according to the specific region of the brain under investigation. The main result of our algorithm is the very high sensitivity 94.74% that guarantees the detection of almost all the cortical lesions, thus offering an interesting way to identify them in a more quick and repeatable way. It is worth noting that neither the gray matter segmentation step nor the cortical lesions extraction make use of anatomical a priori information. Besides, they do not use any commonly available brain tissue segmentation tool, in order to avoid the problems raised and summarized in [66]. In particular, the segmentation of MR images of MS patients usually causes the misclassification of the voxels belonging to MS lesions, either as WM or as GM or as partial volume effect. Even if human intervention is still necessary to finally discard erroneously detected cortical lesions while keeping the correct ones, this step reveals to be straightforward and rapid. The operator, in fact, does not have to peruse the entire acquired volume, but he/she can instead concentrate solely on the regions automatically highlighted by the algorithm. In such a way, it is not necessary for the rater to be highly experienced in recognizing cortical lesions in DIR sequences, since the final classification of the automatically detected regions can be much more easily done on the basis of his/her anatomical knowledge.

A still open issue is represented by false positives: their not trivial number is primarily due to noise and spurious bright voxels. As far as false negatives are concerned, it is worth noting that some lesions covering more than one slice were not automatically detected in all the slices in which they were present. Anyway, in the slices in which they were not recognized, they were counted as a false negative, even if in the adjacent slice they had been correctly identified. This means that the actual false negative rate is lower than the reported value of 5.26%. Besides, further improvements could be introduced for lesion detection in one slice, for instance by using as prior informa-

tion the results obtained in the contiguous slices.

8.4 Cortical Lesions Characterization

The staging of cortical lesions according to their inflammatory activity is determined by the density and distribution of macrophages or microglia. According to these parameters, cortical lesions have been classified in three groups: active cortical lesions, chronic active cortical lesions, and chronic inactive cortical lesions. Starting from the results provided by Pitt et al. ([73]), i.e. that hypointense rings in patients with MS represent iron-rich activated microglia or macrophages, the aim of this final part of the thesis was to verify whether it was possible to stage MS lesions by inflammatory activity in vivo. For this purpose, we were looking for a MRI sequence that could be useful to quantitatively estimate the value of R_2^*, a parameter that is known to be a helpful index to quantify brain iron accumulation ([4]).
Unfortunately, the designed MRI sequence could be acquired only from one person not diagnosed with MS. Nonetheless, on these data different estimating models were tested, and finally a monoexponential model was chosen as the best descriptor of the signal decay. Since no lesion was present in the brain volume, we tested our model's performance comparing our results with those derived from literature. In particular, we found that R_2^* quantification has been performed on different brain regions, among them the putamen and the globus pallidus. We thus estimated the value of R_2^* in these regions, finding out that our estimates have the same order of magnitude of the literature's values. So we can conclude that both our MRI sequence and our estimation model can indeed be used in order to quantify regional tissue R_2^*, and consequently iron-rich activated microglia, which determines the inflammatory activity stage of one lesion.
More work should be done as soon as required data will be available. In particular, in order to verify results obtained in vivo, other techniques (i.e. contrast enhanced T_1-weighted sequence using Gadolinium, commonly used to enhance active MS lesions) should be coupled. It then could be possible to verify whether the two sequences' results agree: this would imply that cortical lesion activity can be characterized avoiding the use of Gadolinium or any

other dye.

8.5 The Way Ahead

Although multiple sclerosis lesions detection necessarily requires the final supervision of an expert rater, the advent of an automatic tool would be desirable and useful. To date, none of the approaches proposed in literature provide a fully automatic procedure that includes all the required steps for cortical lesions detection. For its clinical relevance, there is the need of a technique able to make cortical lesions detection easy to perform, without the need to train the rater according to the MR sequences he/she is examining. Besides, to the best of our knowledge, this is the first attempt to automatically segment multiple sclerosis cortical lesions by exploiting the characteristics provided by FLAIR and DIR MRI sequences. It is worth noting that this work has been performed on data acquired from a 1.5T MRI scanner. More promising results are expected with the use of high field MRI scanners, which provide higher image resolution.
As far as cortical lesion characterization, the proposed technique could represent a valuable and above all non-invasive alternative to the use of contrast dye. Automatic and reliable quantification of the stage of activity of multiple sclerosis cortical lesions may lead to an early identification of risk, allowing to properly adapt therapy.

Appendix A

SPM Options

In order to perform spatial preprocessing, SPM8 [2] provides different options. In particular, as far as coregistration is concerned, we can choose one out of three coregistration modalities, i.e. Estimate, Reslice, and Estimate plus Reslice.
In this thesis, FLAIR and DIR images are coregistered using the *Coregister, Estimate and Reslice* tool in SPM8. The Estimation Options and the Reslice Options have been set as follows:

1. Estimation Options

    - objective function to be minimized to find the registration parameters: Normalized Mutual Information
    - separation, i.e. the average distance between sample points, in mm: [4 2]
    - accuracy tolerance for each parameter: default
    - Gaussian smoothing to be applied to the joint histogram: default

2. Reslice Options

- interpolation: trilinear.

Bibliography

[1] Amato M.P., Ponziani G., Siracusa G., et al. Cognitive dysfunction in early-onset multiple sclerosis: a reappraisal after 10 years *Arch Neurol*, 58:1602-06 (2001).

[2] Ashburner J., Friston. K.J., Unified segmentation. *NeuroImage*, 26 : 839-851 (2005).

[3] Ashburner J., Friston. K.J., Multimodal image coregistration and partitioning - a unified framework. *NeuroImage*, 6(3) : 209-217 (1997).

[4] Aquino D., Bizzi A., Grisoli M., Garavaglia B., Bruzzone M.G., Nardocci N., Savoiardo M., Chiapparini L. Age-related iron deposition in the basal ganglia: quantitative analysis in healty subjects. *Radiology* 252(1): 165-172 (2009).

[5] Bedell B.J., Narayana P.A., Volumetric analysis of white matter, grey matter, and CSF using fractional volume analysis. *Magnetic Resonance in Medicine*,39:961-969 (1998).

[6] Bertrams J., Kuwert E., Liedtke U. HL-A antigens and multiple sclerosis. *Tissue Antigens* 2: 405-408 (1972).

[7] Bö L., Vedeler C.A., Nyland H.I., Trapp B.D., Mörk S.J. Subpial demyelination in the cerebral cortex of multiple sclerosis patients. *J Neuropathol Exp Neurol* 62: 723-732 (2003).

[8] Bö L., Vedeler C.A., Nyland H., Trapp B.D., Mörk S.J. Intracortical multiple sclerosis lesions are not associated with increased lymphocyte infiltration. *Mult Scler* 9: 323-331 (2003).

[9] Bothwell T.H. Overview and mechanisms of iron regulation. *Nutr. Rev.* 53: 237-245 (1995).

[10] Brownell B., Hughes J.T. The distribution of plaques in the cerebrum in multiple sclerosis. *J Neurol Neurosurg Psychiatry* 25:315-320 (1962).

[11] Brusko T.M., Wasserfall C.H., Agarwal A., Kapturczak M.H., Atkinson M.A.. An integral role for heme oxygenase-1 and carbon monoxide in maintaining peripheral tolerance by CD4+CD25+ regulatory T cells. *J Immunol*, 174:5181-86 (2005).

[12] Bydder G.M., Young I.R. MR imaging: clinical use of the inversion recovery sequence. *JCAT* 9 : 659-675 (1985).

[13] Calabrese M., Rocca M. A., Atzori M., Mattisi I., Bernardi V., Favaretto A., Barachino L., Romualdi C., Rinaldi L., Perini P., P. Gallo, Filippi M. Cortical lesions in primary progressive multiple sclerosis. *Neurology* 72: 1330-1336 (2009).

[14] Chan T., Vese L. Active contours without edges. *IEEE Trans. Imag. Proc.*, 10:266-277, (2001).

[15] Chang C-C., Lin C-J. LIBSVM : a library for support vector machines. *ACM Transactions on Intelligent Systems and Technology* 2(3) (2011) .

[16] Cohen-Adad J., Helmer K.G., Nielsen A.S., Greve D., Benner T., Kinkel R.P., Rosen B.R., Mainero C. Quantitative characterization of cortical pathology in multiple sclerosis using surface-based analysis of T2* relaxation at 7T. Proceedings of *ISMRM 19th Scientific Meeting and Exhibition*, Montreal, Canada, 7-13 May (2011).

[17] Compston A. The marvellous harmony of the nervous parts: the origins of multiple sclerosis. *Clinical Medicine, Journal of the Royal College of Physicians* 4(4): 346-354 (2004).

[18] Confavreux C., Vukusic S., Moreau T., Adeleine P. Relapses and Progression of Disability in Multiple Sclerosis. *N. Engl J. Med.* 343:1430-38(2000).

[19] Crompton D.E., Chinnery P.F., Fey C., et al. Neuroferritinopathy: a window on the role of iron in neurodegeneration. *Blood Cells Mol. Dis.* 29: 522-531 (2002).

[20] Dale A.M., Fischl B., Sereno M.I. Cortical surface-based analysis: Segmentation and surface reconstruction. *Neuroimage* 9(2): 179-94 (1999).

[21] Damadian R., Goldsmith M., Minkoff L. NMR in cancer: XVI. FONAR image of the live human body. *Physiol Chem Phys*,9:97-100 (1977).

[22] Dawson J.W. The histology of multiple sclerosis. *Trans R Soc Edinburgh* 50:517-740 (1916)

[23] Dexter D.T., Carayon A., Javoy-Aqid F., et al. Alterations in the levels of iron, ferritin and other trace metals in Parkinson's disease and other neurodegenerative diseases affecting the basal ganglia. *Brain* 114: 1953-1975 (1991).

[24] Dice L.R. Measures of the amount of ecologic association between species. *Journal of Ecology*, 26:297-302, (1945).

[25] Drayer B., Burger P., Darwin R., Riederer S., Herfkens R., Johnson G.A. MRI of brain iron *AJR* 147:103-110 (1986).

[26] Drayer B., Burger P., Hurwitz B., et al. Reduced signal intensity on MR images of thalamus and putamen in multiple sclerosis: increased iron content? *AJR* 149:357-363 (1987).

[27] Duyn J.H., van Gelderen P., Li T.Q., de Zwart J.A., Koretsky A.P., Fukunaga M. High-field MRI of brain cortical substructure based on signal phase. *Proc Natl Acad Sci USA* 104:11796-11801 (2007).

[28] Fainardi E., Castellazzi M., Seraceni S., Granieri E., Contini C. Under the microscope: focus on *Chlamidia pneumoniae* infection and multiple sclerosis.*Curr. Neurovasc. Res.* 5(1): 60-70 (2008).

[29] Feinberg A., Oshio K. GRASE (gradient- and spin-echo) MR imaging: a new fast clinical imaging technique. *Radiology* 181:597-602 (1991).

[30] Fischl B., Sereno M.I., Dale A.M., Cortical Surface-Based Analysis II: Inflation, Flattening, and a Surface-Based Coordinate System, *NeuroImage* 9:195-207 (1999).

[31] Fukunaga M., Li T.Q., van Gelderen P., de Zwart J.A., Shmueli K., Yao B., Lee J., Maric D., Aronova M.A., Zhang G., Leapman R.D., Schenck J. F., Merkle H., Duyn J.H. Layer-specific variation of iron content in cerebral cortex as a source of MRI contrast. *Proc Natl Acad Sci* 107(8): 3834-9 (2010).

[32] Gelineau-Kattner R., Tomassini V., Jenkinson M., Palace J., The effect of white matter lesions on segmentation of deep grey matter structure. In: *16th Annual Meeting og the Organization for Human Brain Mapping*, HBM 2010 (2010)

[33] Geurts J.J.G., Bö L., Pouwels P.J.W., Castelijns J.A., Polman C.H., Barkhof F. Cortical lesions in multiple sclerosis: combined postmortem MR imaging and histopathology. *American Journal of Neuroradiology* 26: 572-77 (2005).

[34] Geurts J.J.G., Roosendaal S.D., Calabrese M., et al. Consensus recommendations for MS cortical lesion scoring using double inversion recovery MRI. *Neurology* 76:418-424 (2011).

[35] Geurts J.J.G., Barkhof F. Grey matter pathology in multiple sclerosis. *Lancet Neurololgy* 7: 841-51 (2008).

[36] Ghugre N.R., Coates T.D., Nelson M.D., Wood J.C. Mechanisms of tissue-iron relaxivity: nuclear magnetic resonance studies of human liver biopsy specimens. *Magn. Reson. Med.* 54(5):1185-93 (2005).

[37] Haacke E.M., Cheng N.Y.C., House M.J., Liu Q., Neelavalli J., Ogg R.J., Khan A., Ayaz M., Kirsch W., Obenaus A. Imaging iron stores in the brain using magnetic resonance imaging. *Magn Reson Imaging* 23:1-25 (2005).

[38] Hallgren B., Sourander P. The effect of age on the non/hemin iron in the human brain. *J. Neurochem.* 3: 41-51 (1958).

[39] Han H., Fischl B. Atlas renormalization for improved brain MR image segmentation across scanner platforms. *IEEE Transactions on Medical Imaging* 26(4):479-486 (2007).

[40] Haralick R.M. Statistical and Structural Approaches to Texture. *Proceedings of the IEEE* 67, 786-804 (1979).

[41] Hayes C.E., Donald Acheson E. A unifying multiple sclerosis etiology linking virus infection, sunlight, and vitamin D, through viral interleukin-10 *Med. Hypotheses* 71: 85-90 (2008).

[42] He T., Gatehouse P.D., Smith G.C., Mohiaddin R.H., Pennell D.J., Firmin D.N. Myocardial T*2 measurements in iron-overloaded thalassemia: an in vivo study to investigate optimal methods of quantification. *Magnetic Resonance in Medicine* 60:1082-1089 (2008)

[43] Held K., Kops E., Krause B., Wells W., Kikinis R., Muller-Gartner H.W., Markov random field segmentation of brain MR images. *IEEE Transactions on Medical Imaging*, 16:878-886 (1997).

[44] Hinshaw D.S., Bottomley P.A., Holland G.N. Radiographic thin-section image of the human wrist by nuclear magnetic resonance. *Nature*, 270:722-723 (1977).

[45] Jaccard P., The distribution of the flora in the alpine zone. New Phytologist, 11(2): 37-50 (1912).

[46] Jersild C., Svejgaard A., Fog T. HL-A antigens and multiple sclerosis. *Lancet*, 1:1240-1241 (1972).

[47] Kass M., Witkin A., Terzopoulos D. Snakes: Active Contour Models. *Int. J. of Comp. Vision*, 1:321-331 (1988).

[48] Koeppen A.H. A brief history of brain iron research. *J Neurol Sci* 207:95-97 (2003).

[49] Lladó X., Ganiler O., Oliver A., Martií R., Freixenet J., Valls L., Vilanova J.C., Ramió-Torrentà L., Rovira A. Automated detection of multiple sclerosis lesions in serial brain MRI. *Neuroradiology* Published online (2011).

[50] Kurtzke J.F. Rating neurologic impairment in multiple sclerosis. An expanded disability status scale (EDSS). *Neurology* 33(11): 1444-52 (1983).

[51] Kutzelnigg A., Lucchinetti C.F., Stadelmann C., Brück W., Rauschka H., Bergmann M., Schmidbauer M., Parisi J.E., Lassmann H. Cortical demyelination and diffuse white matter injury in multiple sclerosis. *Brain* 128: 2705-2712 (2005).

[52] Langkammer C., Krebs N., Goessler W., Scheurer E., Ebner F., Yen K., Fazekas F., Ropele S. Quantitative MR imaging of brain iron: a postmortem validation study. *Radiology.* 257(2):455-62 (2010).

[53] Langkammer C., Khalil M., Enzinger C., Wallner-Blazek M., Jehna M., Fuchs S., Fazekas F., Ropele S. Quantitative assessment of iron in multiple sclerosis lesions. Proceedings of *ISMRM 19th Scientific Meeting and Exhibition*, Montreal, Canada, 7-13 May (2011).

[54] Lauterbur P.C. Image Formation by Induced Local Interactions: Examples of Employing Nuclear Magnetic Resonance. *Nature* 242:190-191 (1973).

[55] LeVine S.M. Iron deposits in multiple sclerosis and Alzheimer's disease brains. *Brain Res.* 760:298-303 (1997).

[56] Li C., Liu J., Fox M.D. Segmentation of external force field for automatic initialization and splitting of snakes. *Pattern Recognition*, 38(11):1947-1960 (2005).

[57] Li C., Xu C., Gui C., Fox M.D. Level set evolution without re-initialization: A new variational formulation. *IEEE Conference on CVPR*, 1, 430-436, (2005).

[58] Li C., Kao C., Gore J., Ding Z. Implicit active contours driven by local binary fitting energy. *Proceedings of IEEE Conference on CVPR* (2007).

[59] Li C., Gatenby C., Wang L., Gore J. A robust parametric method for bias field estimation and segmentation of MR images. *IEEE Conference on Computer Vision and Pattern Recognition.* 218-223 (2009)

[60] Liang Z.P., Lauterbur P.C. Principles of magnetic resonance imaging: a signal perspective. *IEEE Press* (2000).

[61] Lumsden C.E. The neuropathology of multiple sclerosis. In: Vinken P.J., Bruin G.W., ed. *Handbook of Clinical Neurology*. Amsterdam: Elsevier Science Publishers; 217-309 (1970)

[62] McDonald W.I., Compston A., Edan G., Goodkin D., Hartung H.P., Lublin F.D., McFarland H.F., Paty D.W., Polman C.H., Reingold S.C., Sandberg-Wollheim M., Sibley W., Thompson A., van den Noort S., Weinshenker B.Y., Wolinsky J.S. Recommended diagnostic criteria for multiple sclerosis: guidelines from the international panel on the diagnosis of multiple sclerosis. *Ann Neurol* 50:121-127 (2001).

[63] Moraal B., Roosendaal S.D., Pouwels P.J., Vrenken H., van Schijndel R.A., Meier D.S., Guttmann C.R.G., Geurts J.J.G., Barkhof F. Multicontrast, isotropic, single-slab 3D MR imaging in multiple sclerosis. *Eur Radiol* 18:2311-2320 (2008).

[64] Morris C.M., Kerwin J.M., Edwardson J.A.. Non-haem iron histochemistry of the normal and Alzheimer's disease hippocampus. *Neurodegeneration* 3:267-275 (1994).

[65] Naito S., Namerow N., Mickey M.R., Terasaki P.I.. Multiple Sclerosis: association with HL-A3.*Tissue Antigens* 2: 1-4 (1972).

[66] Nakamura K., Fisher E., Segmentation of brain magnetic resonance images for measurement of gray matter atrophy in multiple sclerosis patients. *NeuroImage* 44: 769-776 (2009)

[67] Narayana P., Brey W., Kulkarni M., Sievenpiper C. Compensation for surface coil sensitivity variation in magnetic resonance imaging. *Magn Reson Imaging* 6 (3), 271-274 (1988).

[68] Oksenberg J.R., Baranzini S.E., Sawcer S., Hauser S.L. The genetics of multiple sclerosis: SNPs to pathways to pathogenesis. *Nature Rev. Genet.* 9: 516-526 (2008).

[69] Osher S., Sethian J. Fronts propagating with curvature dependent speed: algorithms based on Hamilton-Jacobi formulations. *J.Comput.Phys.* 79, 12-49 (1988).

[70] Osher S., Fedkiw R. Level set methods and dynamic implicit surfaces. *Appl. Mech. Rev.* Volume 57, Issue 3 (2004).

[71] Paragios N., Deriche R. Geodesic active regions and level set methods for supervised texture segmentation. *Intel J. Comp. Vis.*, 46:223-247, (2002).

[72] Patrikios P., Stadelmann C., Kutzelnigg A., Rauschka H., Schmidbauer M., Laursen H., et al. Remyelination is extensive in a subset of multiple sclerosis patients. *Brain* 129: 3165-72 (2006).

[73] Pitt D., Boster A., Pei W., Wohleb E., Jasne A., Zachariah C.R., Rammohan K., Knopp M.V., Schmalbrock P. Imaging cortical lesions in multiple sclerosis with ultra-high field magnetic resonance imaging. *Arch Neurol.* 67(7):812-818 (2010).

[74] Poletti E., Veronese E., Calabrese M., Bertoldo A., Ruggeri A., Grisan E. Supervised classification of brain tissues through local multi-scale texture analysis by coupling DIR and FLAIR MR sequences. Accepted at *SPIE Medical Imaging*, San Diego, California, USA, February 4-9 (2012).

[75] Porto G., De Sousa M., Subramaniam N. Iron overload and immunity. *World J Gastroenterol*, 13:4707-15 (2007).

[76] Prima S., Ayache N., Barrick T., Roberts N. Maximum likelihood estimation of the bias field in MR brain images: investigating different modelings of the imaging process. *In: LNCS, S. (Ed.)*, Proc. of MICCAI-01. 811-819 (2001)

[77] Prineas J.W., Connel F. Remyelination in multiple sclerosis. *Annuals of Neurology* 5: 22-31 (1979).

[78] Redpath T.W., Smith F.W. Technical note: Use of a double inversion recovery pulse sequence to image selectively grey or white brain matter *The British Journal of Radiology* 67:1258-1263 (1994).

[79] Regis G., Bosticardo M., Conti L., De Angelis S., Boselli D., Tomaino B., Bernabei P., Giovarelli M., Novelli F. Iron regulates T-lymphocyte sensitivity to the INFgamma/STAT1 signaling pathway in vitro and in vivo. *Blood* 105: 3214-21 (2005).

[80] Rydberg J.N., Hammond C.A., Grimm R.C., Erickson B.J., Jack C.R., Huston J., Riederer S.J. Initial clinical experience in MR imaging of the brain with a fast fluid-attenuated inversion-recovery pulse sequence. *Radiology* 193: 173-180 (1994).

[81] Ropele S., de Graaf W., Khalil M., Wattjes M.P., Langkammer C., Rocca M.A., Rovira A., Palace J., Barkhof F., Filippi M., Fazekas F. MRI assessment of iron deposition in multiple sclerosis. *J Magn Reson Imaging* 34(1):13-21 (2011).

[82] Sègonne F., Dale A.M., Busa E., Glessner M., Salat D., Hahn H.K., Fischl B., A hybrid approach to the skull stripping problem in MR, *NeuroImage* 22:1060-1075 (2004)

[83] Seewann A., Vrenken H., Kooi E.J., van der Valk P, Knol D.L., Polman C.H., Pouwels P.J., Barkhof F., Geurts J.J. Imaging the tip of the iceberg: visualization of cortical lesions in multiple sclerosis. *Mult. Scler.* 17(10): 1202-1210 (2011).

[84] Sfagos C., Makis A.C., Chaidos A., Hatzimichael E.C., Dalamaga A., Kosma K., Bourantas K.L.. CSerum ferritin, transferrin and soluble transferrin receptor levels in multiple sclerosis patients. *Mult Scler* 11: 272-275(2005).

[85] Shattuck D.W., Prasad G., Mirza M., Narr K.L., Toga A.W., Online resource for validation of brain segmentation methods. *Neuroimage* 45:431-439 (2009).

[86] Singh A.V., Zamboni P. Anomalous venous blood flow and iron deposition in multiple sclerosis. *Journal of Cerebral Blood Flow and Metabolism* 29: 1867-78 (2009).

[87] Sklansky, J. Image Segmentation and Feature Extraction *IEEE Transactions on Systems, Man, and Cybernetics* 237-247 (1978).

[88] Smith S., Jenkinson M., Woolrich M., Beckmann C., Behrens T., Johansen-Berg H., Bannister P., De Luca M., Flitney D.E., Niazy I.D., Saunders J., Zhang J.V., Stefano N.D., Brady J., Matthews P., 2004. Advances in functional and structural MR image analysis and implementation as FSL. *NeuroImage* (23), 208-219 (2004).

[89] Smith S.M., Fast Robust Automated Brain Extraction. *Human Brain Mapping*, 17(3):143-155 (2002)

[90] Souplet J., Lebrun C., Ayache N., Malandain G. An automatic segmentation of T2-FLAIR multiple sclerosis lesions. In: *The MIDAS Journal - MS Lesion Segmentation* (MICCAI 2008 Workshop). New York, NY, USA (2008)

[91] Stankiewicz J., Panter S.S., Neema M., et al. Iron in chronic brain disorders: imaging and neurotherapeutic implications. *Neurotherapeutics* 4: 371-386 (2007).

[92] Svejgaard A. The immunogenetica of multiple sclerosis. *Immunogenetics* 60:275-286 (2008)

[93] Theil E. Ferritin: structure, gene regulation, and cellular function in animals, plants, and microorganisms. *Annual review of biochemistry* 56(1): 289-315 (1987).

[94] Thirion J.P., Calmon G. Deformation analysis to detect and quantify active lesions in three-dimensional medical image sequences. *IEEE Trans Med Imaging* 18 : 429-441 (1999).

[95] Tincher M.,Meyer C., Gupta R., Williams D. Polynomial Modeling and Reduction of RF Body Coil Spatial Inhomogeneity in MRI. *IEEE Trans Med Imag* 12 (2), 361-365 (1993)

[96] Tsang O., Gholipour A., Kehtarnavaz N., Gopinath K., Briggs R., Panahi I. Comparison of tissue segmentation algorithms in neuroimage analysis software tools. *30th Annual International IEEE EMBS Conference Vancouver*, British Columbia, Canada, August 20-24 (2008).

[97] Tuceryan M., Jain A K. Methods in Computer Vision: Texture Analysis in *The Handbook of Pattern Recognition and Computer Vision* (2nd Edition)), by C. H. Chen, L. F. Pau, P. S. P. Wang (eds.), pp. 207-248, World Scientific Publishing Co. (1998)

[98] Veronese E., Grisan E., Calabrese M., Favaretto A., Gallo P., Bertoldo A. Automatic Segmentation of Gray Matter Multiple Sclerosis Lesions on DIR Images submitted to*16th annual meeting of the Organization for Human Brain Mapping* (2010).

[99] Vese L., Chan T. A multiphase level set framework for image segmentation using the mumford and shah model. *Intel J. Comp. Vis.*, 50:271-293, (2002).

[100] Vymazal J., Righini A., Brooks R.A., Canesi M., Mariani C., Leonardi M., Pezzoli G. T1 and T2 in the brain of healthy subjects, patients with Parkinson disease, and patients with multiple system atrophy: relation to iron content. *Radiology* 221(2): 489-495 (1999).

[101] Vovk A., Cox R.W., Stare J., Suput D., Saad Z.S. Segmentation priors from local image properties: Without using bias field correction, location-based templates, or registration. *Neuroimage* 56(1) 142-152 (2011).

[102] Waxman S.G. Axonal conduction and injury in multiple sclerosis: the role of sodium channels. *Nat.Rev.Neurosci.* 7: 932-941 (2006).

[103] Willis S.N., Stadelmann C., Rodig S.J., Caron T., Gattenloehner S., Mallozzi S.S., Roughan J.E., Almendinger S.E., Blewett M.M., Brück W., Hafler D.A., O'Connor K.C. Epstein-Barr virus infection is not a characteristic feature of multiple sclerosis brain. *Brain* 132(12):3318-3328 (2009).

[104] Wood J.C., Ghugre N. Magnetic resonance imaging assessment of excess iron in thalassemia, sickle cell disease and other iron overload diseases. *Hemoglobin.* 32(1-2):85-96 (2008)

[105] Wood J.C., Enriquez C., Ghugre N., Tyzka J.M., Carson S., Nelson M.D., Coates T.D. MRI R2 and R2* mapping accurately estimates hepatic iron concentration in transfusion-dependent thalassemia and sickle cell disease patients. *Blood* 106(4):1460-1465 (2005).

[106] Zhang Y., Brady M., Smith S., Segmentation of Brain MR Images Through a Hidden Markov Random Field Model and the Expectation-Maximization Algorithm, *IEEE Transactions on Medical Imaging*, 20(1) (2001)

[107] Zijdenbos A.P., Forghani R., Evans A.C. Automatic pipeline analysis of 3-D MRI data for clinical trials: application to multiple sclerosis. *IEEE Trans Med Imaging*, 21(10):1280-1291 (2002).